GDAŃSK UNIVERSITY
OF TECHNOLOGY
Faculty of Electrical and Control Engineering

SuperGrid
Institute

Author: mgr inż. Piotr Dworakowski

Scientific discipline: Automation, Electronics and Electrical Engineering

**DOCTORAL DISSERTATION**

# Title: Modelling and analysis of medium frequency transformers for power converters

Tytuł: Modelowanie i analiza transformatora średniej częstotliwości dla potrzeb przekształtników energoelektronicznych

Supervisor
dr hab. inż. Andrzej Wilk, profesor uczelni
Gdańsk University of Technology

Auxiliary supervisor
dr inż. Michał Michna
Gdańsk University of Technology

Technical supervisor
dr Michel Mermet-Guyennet
SuperGrid Institute

Technical supervisor
dr Bruno Lefebvre
SuperGrid Institute

Gdańsk, 2020

# Abstract

The evolutions in power systems and electric vehicles, related to the economic opportunities and the environmental issues, bring the need of high power galvanically isolated DC-DC converter. The medium frequency transformer (MFT) is one of its key components, enabled by the increasing switching frequency of modern power semiconductors like silicon carbide transistors or diodes. The increased operating frequency offers small converter size, leading to the decrease in raw material usage. Most likely this will result in the converter cost reduction what will further increase the demand for solid state transformer solutions. The modelling and analysis are essential in the development of the MFT technology which is attracting lots of research and industrial interest.

In this dissertation the isolated DC-DC converter topologies are introduced with the particular focus on the dual active bridge (DAB). The key components of the isolated DC-DC converters, power semiconductors and medium frequency transformer are reviewed.

A mathematical model of a 3-phase MFT in the isolated DC-DC power converter, suitable in electromagnetic transient and steady state simulation is developed. The transformer modelling methods are reviewed and the Lagrange energy method is used to derive a physically motivated model for circuit analysis. The model involves a matrix of nonlinear magnetizing inductances and a matrix of linear leakage inductances, both including self and mutual values. The macroscopic models of magnetic hysteresis are reviewed and the feedback Preisach model is developed.

The design of a 3-phase 20 kHz transformer for a 100 kW 1.2 kV isolated DC-DC power converter is presented. The particular focus is put on the winding and core design, and power loss and thermal calculations which are the most critical aspects of the high-power density transformer. The design results in two 3-phase MFT prototypes, first of its kind worldwide.

A finite element model of the transformer is developed allowing to determine the magnetic flux characteristic $\boldsymbol{\Phi}(\boldsymbol{\Theta})$ and the related inductances required in the circuit model. The finite element model is based on the measured equivalent $B(H)$ and homogenized material properties. Other model parameters are calculated analytically and compared against the measurement on the prototype MFT.

The dissertation is concluded showing the technical feasibility and benefits of the 3-phase MFT. The developed MFT prototype operating at 20 kHz is more than 10 times lighter than the equivalent 50 Hz transformer. The 3-phase 100 kW DC-DC converter efficiency is measured 99.2% what is an impressive result. The efficiency of the 3-phase DC-DC is higher than its equivalent single-phase variant.

A challenge of high power MFT design related to the parasitic air gaps in the core is highlighted. The influence of the air gaps on core power loss is confirmed showing that the increase in the air gap size in a certain range causes a decrease in the core power loss. In the 3-phase MFT prototype the parasitic air gaps do not cause any measurable effect on winding power loss and temperature. It is shown that the relative magnetic permeability is nonlinearly decreasing with the increase of the number of parasitic air gaps. An exponential interpolation function is proposed allowing to estimate the equivalent magnetic permeability, average air gap length and magnetizing inductance for any high-power ferrite core MFT with a similar core assembly.

The proposed MFT equivalent circuit model is proven accurate in steady state and transient analyses. The no-load inrush test confirms the importance of the magnetic cross saturation involved in the magnetizing inductance model. The influence of the mutual leakage inductance on the operation of the DAB converter is shown. The feedback Preisach model of hysteresis is proven accurate in the modelling of hysteresis loops in the multi air gap ferrite core MFT.

# Streszczenie

Postępujące zmiany w systemach elektroenergetycznych i pojazdach elektrycznych, związane z możliwościami ekonomicznymi i kwestiami środowiskowymi, wytworzyły zapotrzebowanie na izolowane galwanicznie przekształtniki DC-DC dużej mocy. Transformator średniej częstotliwości (MFT) jest jednym z ich kluczowych elementów. Technologia MFT rozwijana jest dzięki dostępności nowoczesnych półprzewodników mocy o coraz większej częstotliwości przełączeń, takich jak np. tranzystory i diody wykonane z węglika krzemu. Zwiększona częstotliwość pracy skutkuje małymi rozmiarami przekształtnika, co z kolei prowadzi do zmniejszenia zużycia materiałów konstrukcyjnych. Opracowanie technologii umożliwiających wieloseryjną produkcję przemysłową spowoduje dalszą redukcję kosztów przekształtnika, co dodatkowo zwiększy zapotrzebowanie na rozwiązania oparte na transformatorach z energoelektronicznymi przekształtnikami. Projektowanie oparte na modelowaniu, symulacji i analizie jest podstawą rozwoju technologii MFT i przyciąga coraz większe zainteresowanie w świecie nauki i przemysłu.

W niniejszej rozprawie przedstawiono izolowane topologie przekształtników DC-DC, skupiając się na topologii DAB (ang. *dual active bridge*). Przeanalizowano kluczowe elementy przekształtników DC-DC takich jak półprzewodniki mocy i transformator średniej częstotliwości.

Opracowano model matematyczny trójfazowego MFT zastosowany w izolowanym przekształtniku DC-DC. Model ten nadaje się do symulacji elektromagnetycznych stanów ustalonych i nieustalonych. Opisano różne metody modelowania transformatorów, a metoda Lagrange'a została wybrana do opracowania szczegółowego modelu obwodowego. Model transformatora uwzględnia macierz nieliniowych indukcyjności magnesujących oraz macierz liniowych indukcyjności rozproszenia. Obie macierze zawierają zarówno wartości własne i wzajemne. Opisano makroskopowe modele histerezy magnetycznej. Model Preisach'a ze sprzężeniem zwrotnym został opracowany dla analizowanego MFT.

Przedstawiono projekt trójfazowego transformatora 20 kHz zastosowany w prototypowym przekształtniku DC-DC o mocy 100 kW i napięciu 1,2 kV. Szczególny nacisk położono na aspekty istotne przy projektowaniu transformatora o dużej gęstości mocy. Opisano proces projektowania konstrukcji uzwojenia i rdzenia transformatora, uwzględniając zagadnienia symulacji i obliczeń strat mocy oraz temperatur. Wynikiem projektu są dwa, unikatowe w skali światowej, w pełni funkcjonalne trójfazowe transformatory średniej częstotliwości.

Opracowano model polowy transformatora, który umożliwia wyznaczenie charakterystyki strumienia magnetycznego w funkcji przepływu $\boldsymbol{\Phi}(\boldsymbol{\Theta})$. W zaproponowanym modelu obwodowym użyto indukcyjności wynikających z charakterystyki $\boldsymbol{\Phi}(\boldsymbol{\Theta})$. Opracowano metodę wyznaczania zastępczej charakterystyki magnesowania, w oparciu o pomiar na prototypie MFT. Zastępcza charakterystyka magnesowania została wykorzystana w uproszczonym modelu polowym MFT. Pozostałe parametry modelu obwodowego wyznaczono na podstawie zależności analitycznych. Poprawność metod i modeli została zweryfikowana w oparciu o porównanie wyników symulacji i pomiarów.

Rozprawa wykazuje techniczną wykonalność i zalety trójfazowego MFT. Opracowany prototyp MFT pracujący przy 20 kHz jest ponad 10 razy lżejszy niż porównywalny transformator 50 Hz. Sprawność trójfazowego przekształtnika DC-DC 100kW wynosi 99,2%, co jest bardzo dobrym wynikiem. W oparciu o wyniki pomiarów stwierdzono, że sprawność trójfazowego przekształtnika DC-DC jest wyższa niż wariant jednofazowy.

W rozprawie szczególny nacisk położono na analize konsekwencji konstrukcji wielosegmentowego rdzenia ferrytowego MFT dużej mocy. Konstrukcja związana jest z licznymi niepożądanymi szczelinami powietrznymi. Potwierdzono, że wzrost długości szczeliny powietrznej w pewnym zakresie, powoduje zmniejszenie strat mocy w rdzeniu. Na podstawie badań symulacyjnych i wyników pomiarów stwierdzono, że w analizowanym MFT, szczeliny powietrzne nie powodują żadnego mierzalnego wpływu na straty mocy i temperaturę uzwojenia. Wykazano, że przenikalność magnetyczna rdzenia zmniejsza się nieliniowo wraz ze wzrostem liczby szczelin powietrznych. Zaproponowano wykładniczą funkcję pozwalającą oszacować zastępczą przenikalność magnetyczną, średnią długość szczeliny powietrznej i indukcyjność magnesującą dla dowolnego MFT o podobnej konstrukcji rdzenia z materiału ferrytowego.

Wykazano, że zaproponowany model obwodowy MFT pozwala na dokładną analizę stanów ustalonych i nieustalonych. Próba włączenia transformatora potwierdza istotny wpływ nasycenia magnetycznego pomiędzy kolumnami, które modelowane jest w macierzy indukcyjności magnesującej, na wartość prądu udarowego. Wykazano wpływ wzajemnej indukcyjności rozproszenia na pracę przekształtnika DAB. Wykazano, że model histerezy Preisach'a ze sprzężeniem zwrotnym charakteryzuje się dużą dokładnością w modelowaniu pętli histerezy rdzenia ferrytowego MFT z wieloma szczelinami powietrznymi.

# Acknowledgment

This doctoral dissertation is a result of a 5-year work, enabled by many people who I would like to address my personal thanks.

I am very grateful to my thesis supervisor Andrzej Wilk. Since the end of my master studies in 2007 he encouraged me to proceed with my academic development. Finally, in 2015 he succeeded and together we launched the doctoral studies. He helped me with his undoubtable scientific and technical knowledge, his long-term and every-day guidance and by controlling my personal temper. Eventually, from professor Wilk he has become my friend Andrzej.

I am also very grateful to my auxiliary supervisor Michał Michna. We have known each other well since he was my master thesis supervisor back in 2007. He is an expert in electrical machines and the Matlab mastermind. Without his help I would have really struggled with many programming tasks.

I am particularly grateful to my technical supervisor Michel Mermet-Guyennet. He was the only manager who enabled me to work on the doctoral thesis while continuing my ordinary engineering job. He is an expert in power electronics and a true leader. Quite often he comes out with visions which many people judge wrong, but which eventually become right. Michel made me develop many personal and managerial skills. He is a kind of a boss that you hang out with while reaching very good professional results.

I thank my technical supervisor Bruno Lefebvre who helped me from the beginning to the end of the study. He is an excellent engineer and a careful manager. Our numerous collaborations have always been a pleasure.

I also thank some of my colleagues who helped me during the study or well before: Janusz Nieznański, Jarosław Guziński, Maciej Łuszczek, Ewa Wawoczna, Krzysztof Karwowski, Mieczysław Ronkowski, Roland Ryndzionek, Filip Kutt, Artur Cichowski, Wojciech Śleszyński, Piotr Chrzan, Jean-François Ballet, Thomas Lagier, Cyril Buttay, François Wallart, Laurent Chédot, Przemysław Makowski, Jose Maneiro, Martin Guillet, Alexis Fouineau, Albert Pereira, Layal Ghossein, Hadiseh Geramirad, Caroline Stackler, Juan Paez, Pierre Le Métayer, Pierre-Baptiste Steckler, Florian Errigo, Daniel Gomez, Diego Velazco, Christophe Hamond, Joël Jeremiash, Philippe Camail, Elissa Anak, Florent Morel, Hervé Morel, Philippe Lasserre, Fabrice Potiron, Eve-Anne Poubelle and all colleagues I have forgotten. Thank you.

Finally, I would like to thank my family. I thank my wife and children who accepted me working the long hours on weekends and holidays for the past 5 years. They have paid a lot and I am very grateful. I thank my mother and father who have raised me with care and made me the man I am today. They have always supported me in my development and encouraged me in the doctoral studies. I thank my brother, my grandparents, my in-laws and the entire family for all the support.

# Contents

# Acronyms

| | |
|---|---|
| AC | Alternating Current |
| CFD | Computational Fluid Dynamics |
| CIGRE | Conseil International des Grands Réseaux Electriques (International council on large electric systems) |
| DAB | Dual Active Bridge |
| DAB3 | Dual Active Bridge 3-phase |
| DC | Direct Current |
| EMI | Electromagnetic Interference |
| EV | Electric Vehicle |
| FEM | Finite Element Method |
| GUT | Gdańsk University of Technology |
| HVDC | High Voltage Direct Current |
| IGBT | Insulated Gate Bipolar Transistor |
| MFT | Medium Frequency Transformer |
| MMC | Modular Multilevel Converter |
| MOSFET | Metal Oxide Semiconductor Field Effect Transistor |
| MVDC | Medium Voltage Direct Current |
| PV | Photovoltaic |
| SST | Solid State Transformer |
| VSC | Voltage Source Converter |
| WBG | Wide Band Gap |
| ZVS | Zero Voltage Switching |

# 1. Introduction

## 1.1. Context

A new battle in the War of Currents [47], with Edison's direct current (DC) and Westinghouse's alternating current (AC) at the origin, has begun. The arrival of new power semiconductors, such as thyristors and insulated gate bipolar transistors (IGBT), and the development of electronics and computer science, have been the main triggers. The transmission of bulk power over very long distances is now reserved to high voltage direct current (HVDC), which has been recently revolutionised by the modular multilevel converter (MMC) [104]. Thanks to the technological improvements in wide band gap semiconductors, such as the silicon carbide SiC [123], an increasing number of applications may switch to DC in the coming years. The DC-DC converters are often proposed in modern power systems and transportation applications such as photovoltaic, wind power, electric vehicles and railway traction. The DC-DC converter is also a key subsystem of the AC-DC or AC-AC converters called solid state transformers (SST) [152] as presented in Fig. 1.1. In general, the DC-DC converters will play a major role in the future smartgrids and supergrids [17].

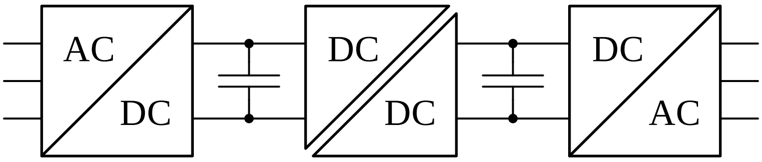

Fig. 1.1. Solid state transformer diagram based on a 3-stage conversion with an isolated DC-DC converter

The dual active bridge (DAB) converter [27] is one of the most promising DC-DC circuit topologies for high power applications [94]. The series and/or parallel connection of elementary DABs allows to increase the voltage and power to build converters well suited for medium voltage DC (MVDC) and potentially extensible to high voltage DC (HVDC) applications [99]. However, even if a high voltage insulated DAB has been reported in [151] it seems that for the moment these multi-cell converters are more viable for MVDC applications.

The medium frequency transformer (MFT) is one of the key components of the DAB [139]. This is still quite a novel technology with lots of research interest. The main technological challenges consist in winding, core and insulation design and materials, especially at medium frequency. It can be highlighted the selected state of the art reported in [55], [136], [172] regarding winding, core and insulation respectively.

The modelling and analysis are essential in the design of medium frequency transformers. The accurate power loss and temperature estimation are probably the most important challenges of the design. This is due to the high-power density which is in fact the objective of any MFT design. The medium frequency excitation reveals the importance of precise modelling of frequency effects on winding resistance, parasitic capacitance and power loss.

This doctoral dissertation is a result of a collaboration between Gdańsk University of Technology (GUT), LINTE$^2$ and SuperGrid Institute. GUT is one of the oldest technical universities in Poland. The LINTE$^2$ Laboratory at GUT is a complex experimental installation dedicated to R&D activities in the area of electric power systems. SuperGrid Institute is a research and innovation center in Lyon, France, developing key technologies for future electricity grids and renewables integration. In particular, the development of MFT technology, as a key component of isolated DC-DC converters, is a part of the institute's research and business strategy. Since 2014 the author has been leading an R&D team at SuperGrid Institute focused on power converters for electricity grids and electric vehicles.

The author is an active member of two CIGRE working groups related to the scope of this dissertation:

- B4.76 DC-DC converters in HVDC Grids and for connections to HVDC systems, where he is in charge of a chapter on the modelling of DC-DC power converters,
- C6/B4.37 Medium voltage DC distribution systems, where he contributes to the DC-DC converter technology review.

## 1.2. Theses

The theses of this doctoral dissertation are the following:

Thesis 1 - the feedback Preisach model of hysteresis with the distribution function approximated by a two-dimensional Gauss functional series, precisely represents the magnetic hysteresis loops in the multi air gap medium frequency transformers composed of type "I" MnZn ferrite cores.

Thesis 2 - the equivalent magnetic permeability and the average air gap length in the multi air gap medium frequency transformers composed of type "I" MnZn ferrite cores, are nonlinear functions of the number of air gaps which can be approximated with an exponential function.

Thesis 3 - the nonlinear mutual inductances in the 3-phase multi air gap medium frequency transformers composed of type "I" MnZn ferrite cores, influence the accuracy of the transformer equivalent circuit model:

- the magnetizing flux cross saturation has a significant impact on the inrush current in the transformer no load test supplied from the voltage source converter,
- the mutual leakage inductances have a significant impact on the power transfer in the dual active bridge converter.

## 1.3. Objectives

The objectives of this doctoral dissertation are the following:

- development of a mathematical model of a 3-phase medium frequency transformer for circuit analysis of isolated DC-DC converters,
- development of a magnetic hysteresis model suitable in equivalent circuit analysis and in power loss analysis of medium frequency transformers,
- development of finite element models of the 3-phase medium frequency transformer for electromagnetic and thermal analyses, allowing determination of the equivalent circuit model parameters,
- design, prototyping and testing of the 3-phase medium frequency transformer demonstrating the feasibility and benefits in high power isolated DC-DC converters,
- experimental verification of the 3-phase medium frequency transformer model,
- analysis of the 3-phase medium frequency transformer in isolated DC-DC converters.

## 1.4. Scope

Chapter 2 provides the state of the art on power converters and related technologies. The motivation for this doctoral dissertation is given in perspective of evolutions in power systems and electric vehicles. The isolated DC-DC converter topologies are introduced with the particular focus on the dual active bridge. The key components of isolated DC-DC converters, power semiconductors and medium frequency transformer, are reviewed providing the list of challenges for the development of MFT.

Chapter 3 presents a mathematical model of the MFT in the isolated DC-DC power converter. The transformer modelling methods are reviewed and the Lagrange energy method is used to derive a physically motivated model for circuit analysis. The macroscopic models of magnetic hysteresis are reviewed and the feedback Preisach model is developed.

Chapter 4 details the design of a 3-phase 20 kHz transformer for a 100 kW 1.2 kV isolated DC-DC power converter. The particular focus is put on the winding and core design and power loss which are the most critical aspects of the high-power density transformer. Two 3-phase MFT prototypes are presented.

Chapter 5 deals with the parameters for the model developed in chapter 3, based on the transformer design from chapter 4. A finite element model of the transformer is developed allowing to determine the magnetic flux characteristic $\mathbf{\Phi}(\mathbf{\Theta})$. Some of the analytically calculated parameters are compared against measurements on the MFT prototype. In particular, the feedback Preisach model of hysteresis is compared with the measurement proving the thesis 1.

Chapter 6 provides some analyses and verifications. The experimental test results on the prototype MFT are presented including the thermal test and efficiency measurement. The influence of the parasitic air gaps on the equivalent magnetic permeability, average air gap length and power losses is discussed proving the thesis 2. The effect of magnetic cross saturation and mutual leakage inductance is studied proving the thesis 3.

Chapter 7 concludes this doctoral dissertation and provides some perspectives for future research.

The document contains 5 appendices.

The novel aspects of this dissertation include:

- Lagrangian model of 3-phase DAB for electromagnetic transient and steady state simulation,
- 3-phase MFT model accounting magnetic cross saturation for precise steady state and transient analyses; the model involves a matrix of nonlinear magnetizing inductances and a matrix of linear leakage inductances, both including self and mutual values,
- Feedback Preisach model of hysteresis for multi air gap MFT composed of type "I" MnZn ferrite cores,
- 3-phase MFT prototype for a 100kW 20 kHz DC-DC power converter,
- Determination of the equivalent $B(H)$, the equivalent magnetic permeability and the average air gap length in a 3-phase multi air gap ferrite core MFT,
- Practical approach to the determination of 3-phase MFT model parameters based on magnetostatic FEM simulations,

- Demonstration that the equivalent magnetic permeability and the average air gap length of the multi air gap ferrite core MFT are nonlinear functions of the number of air gaps,
- Proposal of an exponential scaling function enabling a rapid estimation of the magnetizing inductance based on the ferrite material datasheet only.

# 2. Power converters and related technologies

## 2.1. Evolutions in power systems and transportation

The power system is organised in a hierarchical structure involving power generation, transmission and distribution. The electric power is primarily generated in large power plants: nuclear, coal and gas. The power transmission covers the large distances using the high voltage overhead lines in a meshed grid. The power distribution serves the industrial and household loads in medium and low voltage radial grids.

Due to the economic opportunities and the environmental issues of the 20th and 21st centuries, the power system is facing several changes. Nowadays the power generation is developing with the distributed renewable energy sources. The wind power plants are being installed on the mainland and offshore. The solar power plants are spreading from the large power plants to the small units on the household rooftops. The electricity market directives and liberalisation excite the development of new technologies. The power consumption is changing with new types of loads as electric vehicles, consumer electronics or air conditioning. The power transmission and distribution systems have to face these changes.

The high voltage direct current (HVDC) technology is expanding in the transmission grids. It offers the economically viable solution for the long-distance power transmission, especially when the underground or underwater cables are used. The power losses in DC cables are much lower than in AC cables because there is no reactive power that makes the reactive current circulate, creating the joule losses in the conductors [119]. However, the HVDC transmission requires the converter stations that have a significant cost and add some power losses. There can be found a break-even-distance where the HVDC becomes more economically interesting than the HVAC as presented in Fig. 2.1.

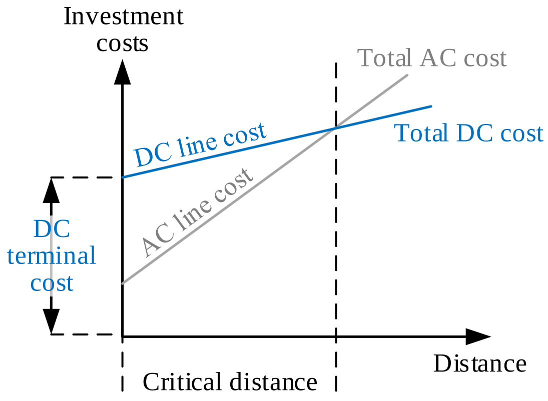

Fig. 2.1. Investment costs of HVDC and HVAC transmission [1]

In case of overhead lines, the break-even-distance is approximately 600-800 km and in case of submarine cables it drops down to 50 km [1]. In some situations, the HVDC technology may be the only solution due to the limited availability of the right of way (ROW) for new overhead transmission lines [5]. The HVDC technology is also used in order to interconnect the asynchronous power systems or to reinforce the existing interconnections, offering new trade opportunities. In Fig. 2.2 it is presented the expansion of HVDC links in Europe.

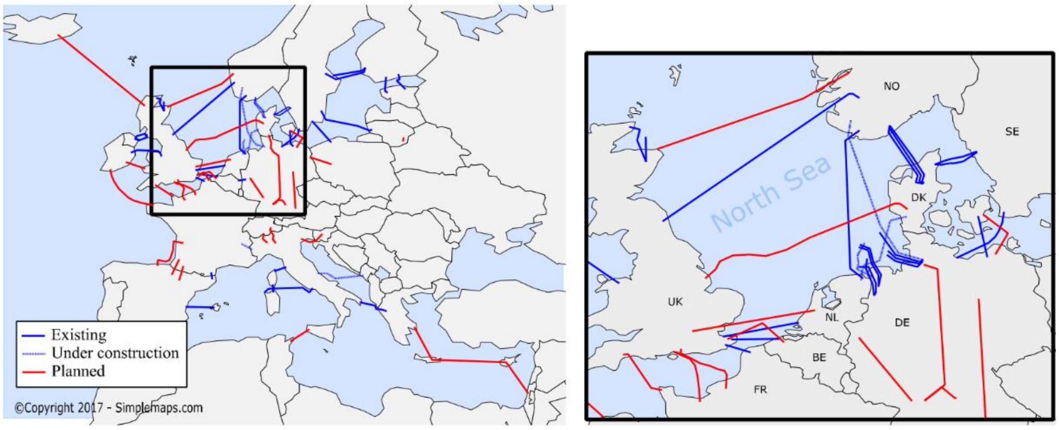

Fig. 2.2. HVDC links in Europe [63]

The similar reasons that have made the HVDC technology spread in power transmission are making the MVDC technology emerge in power distribution [23]. Recently, Siemens has proposed a product for MVDC links offering among others the low transmission losses and power flow controllability [156]. ABB makes a similar analysis in [2]. The Angle DC project in United Kingdom is an example of converting two existing MVAC circuits to operate as MVDC circuits [198]. The 23% increase in transmitted power capacity is expected. Moreover, the converter stations will provide the reactive power control capability on both AC networks, which will improve the voltage profile in the local region and hence reduce the operating losses in the networks. On the other hand, the DC electrification of railways is a kind of existing MVDC grid. The existing MVDC infrastructure disposes high installed power but with a low average power usage. It could be considered to use this infrastructure for integrating renewable energy sources or suppling additional loads [204].

The distribution grids are facing today some issues related to voltage control, power flow management and fault current level management. The conventional solutions as new line installation, reactive power compensators and transformer on-load tap changers solve those issues only partially. An innovative solution based on a smart substation transformer is investigated in a demonstration project LV engine in the United Kingdom [88]. The solution is composed of 11 kV / 400 V power electronics-based device and a smart control system (Fig. 2.3). It is supposed to increase the network controllability and flexibility.

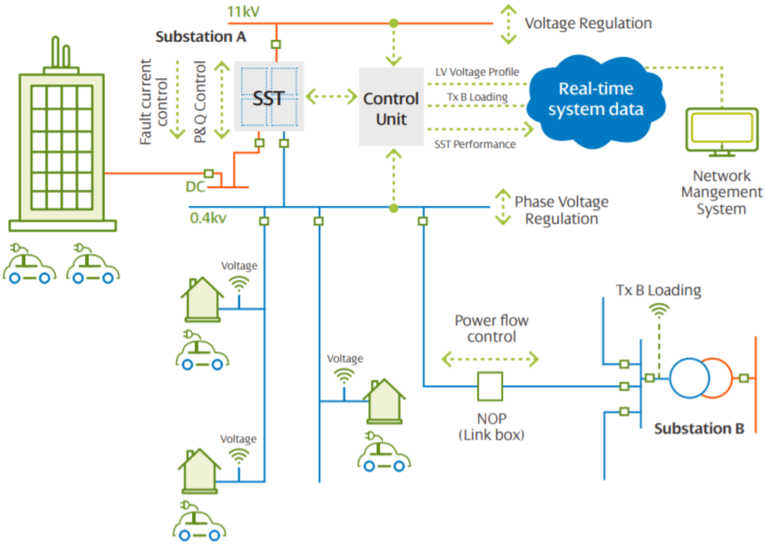

Fig. 2.3. LV engine project diagram (copied from [159] under SP Energy Networks permission)

The collection grids for wind and solar power plants are attracting the research and industrial interest [148]. In large offshore wind power plants, the distance between the wind turbines and HVDC converter stations exceeds tens of kilometres. Since the underwater cables are used then the DC current transmission may be considered [26]. On the other hand, the DC collection grid with a direct to shore connection has been examined in [15] and it is gaining the interest for some specific locations, too close to shore for HVDC and too far from shore for HVAC. The large solar power plants may also benefit from DC current transmission. The photovoltaic (PV) modules are inherently producing the electric power in DC so it seems relevant to consider the DC collection grid [19].

The 21st century will see the electric vehicle (EV) market booming, at least in Europe where the combustion engines are meant to be out of sale starting from year 2040. This will come with a massive demand of EV charging points. In a similar way to PV, the storage elements of the EV are inherently DC so they require an appropriate DC charging interface [38]. Trucks will be most likely supplied from hydrogen fuel cells, requiring a DC interface [85] in similar manner than the todays hydrogen trains [8]. Moreover, in the future evolutions of the AC electrified trains, the power electronics solutions may be considered to replace the classical transformers [202].

The evolutions in the power generation involving a high share of renewable energy sources and new power loads will inevitably require the additional energy storage. The existing hydraulic pumped-storage plants will be most likely extended with variable speed drives [52]. The expansion of EV may support the energy storage thanks to the concept of vehicle-to-grid [196]. The energy storage elements like capacitors, supercapacitors or batteries that are considered for distributed storage systems will require a DC interface.

All the above presented applications have at least one point in common. They all require or will require the DC-DC power converters. We can roughly assume the ratings of these converters in the range from 1 kV - 10 kW to 1 MV - 1 GW. The DC-DC converters can be organised in two principal groups: isolated and non-isolated [137]. In most applications, due to technical constraints or standards, the DC-DC converter needs to provide a galvanic separation. For these reasons, in this work the isolated DC-DC converters will be further analysed.

## 2.2. Power electronics converters

An isolated DC-DC converter is composed of at least: an inverter, a transformer and a rectifier (Fig. 2.4). In many applications, the inverter and the rectifier are of a voltage source converter (VSC) type. The variety of DC-DC converter topologies is at least as wide as the variety of VSC topologies.

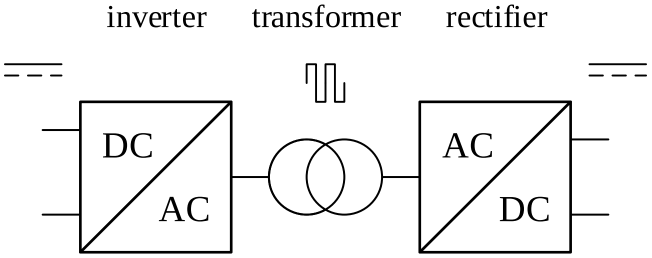

Fig. 2.4. General diagram of an isolated DC-DC converter

### 2.2.1. Voltage source converters

There are 3 VSC topologies that are widely used in high power industrial applications:

- two level inverter (2LI),
- neutral point clamped inverter (NPC),
- modular multilevel converter (MMC).

The 2LI is likely the most common VSC used in the industrial applications. The 2LI topology is composed of at least one inverter leg (Fig. 2.5) and the most common is the 3-leg, 3-phase topology. In high power applications the IGBT power semiconductors with the blocking voltage from 650 V to 6500 V are widely used. If a higher blocking voltage is required, then a series connection of individual IGBTs is possible but very challenging. The 2LI offers the independent bidirectional active and reactive power flow control. Compared to the square wave modulation, the pulse width modulation (PWM) is often used to reduce the harmonic content of the AC current.

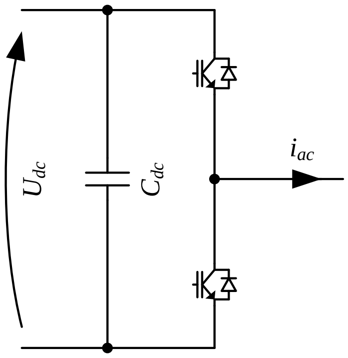

Fig. 2.5. One leg of a two-level voltage source converter (2LI): $U_{dc}$ DC bus voltage, $C_{dc}$ DC bus capacitor, $i_{ac}$ AC current

The NPC offers an interesting alternative to 2LI if the DC bus voltage is higher than the available power semiconductor blocking voltage or if the harmonic requirements have to be met with a low switching frequency [130]. The 3-level NPC converter leg is presented in Fig. 2.6. Compared to the 2LI, for the same $U_{dc}$ and IGBT, it requires two additional diodes and the DC capacitor $C_{dc}$ has to be split into two. The 5-level NPC is also used but the complexity of the topology is rapidly increasing with the increase of number of levels.

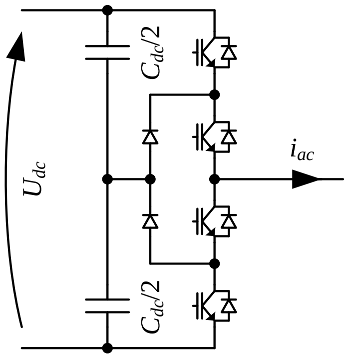

Fig. 2.6. One leg of a neutral point clamped voltage source converter (NPC)

The MMC was invented in 2003 by Marquardt [104] and it has revolutionised the HVDC market. The 1-leg MMC is presented in Fig. 2.7. Each converter leg is composed of two arms. Each arm is composed of a series connection of submodules (SM) and an inductor $L_{arm}$. The submodule is basically a one leg 2LI with DC bus capacitor $C_{sm}$. This topology has no interest in the applications where the 2LI or NPC can be used but it allows the unlimited converter scaling in voltage. For example, the North Sea wind power plant DolWin3 is based on a 640 kV - 900 MW MMC [59].

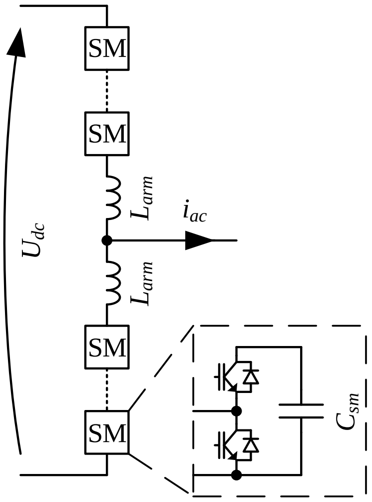

Fig. 2.7. One leg of a modular multilevel voltage source converter (MMC)

### 2.2.2. Isolated DC-DC converters

According to the system requirements, the isolated DC-DC converters can be of unidirectional or bidirectional power type. In case of the unidirectional converter, the rectifier in Fig. 2.4 is a diode bridge. The converter topology may involve a resonant circuit. The converter control and modulation techniques can further impact the performance of the converter. In high power applications the following topologies are of the interest:

- series resonant converter (SRC),
- LLC DC-DC resonant converter (LLC),
- phase-shifted full bridge (FSFB),
- dual active bridge (DAB),
- single active bridge (SAB)

where any VSC topology can be considered for the inverter and rectifier bridge. However, for the further analysis the 2LI is considered.

The SRC is composed of a VSC, LC resonant circuit ($L_{ac}$, $C_{ac}$), transformer and diode bridge with capacitor filter as presented in Fig. 2.8. It was proposed in [150] using thyristors where the LC circuit ensures the device commutation and energy transfer. However, the topology can be implemented with any power semiconductor device. The diode rectifier can be replaced with a VSC operating in the synchronous rectification.

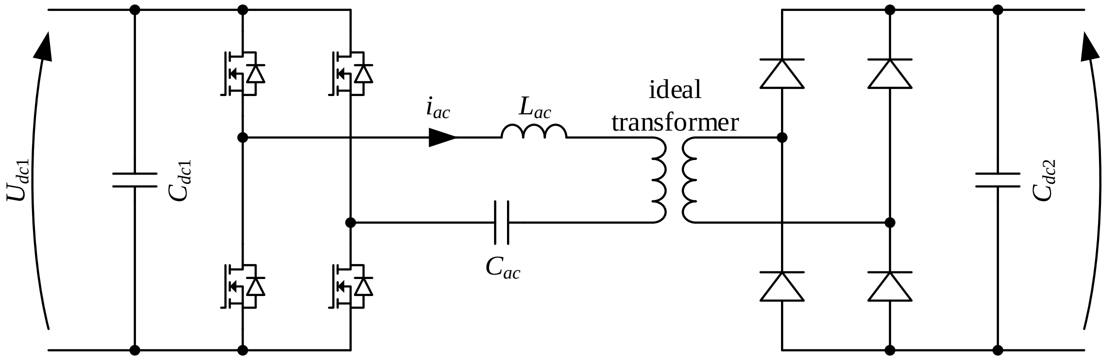

Fig. 2.8. Series resonant converter (SRC) based on a 2LI: $U_{dc1}$ input DC bus voltage, $U_{dc2}$ output DC bus voltage, $C_{dc1}$ input DC bus capacitor, $C_{dc2}$ output DC bus capacitor, $i_{ac}$ AC current

The LLC converter is composed of a VSC, LLC resonant circuit ($L_{ac}$, $L_m$, $C_{ac}$), transformer and diode bridge with capacitor filter as presented in Fig. 2.9. The LLC circuit may be physically realised with the leakage $L_{ac}$ and magnetizing $L_m$ inductance of the transformer. The analysis of the circuit is presented in [100]. The circuit offers the buck and boost operation with the zero-voltage switching (ZVS) in the entire power range. The diode rectifier can be replaced with a VSC operating in the synchronous rectification.

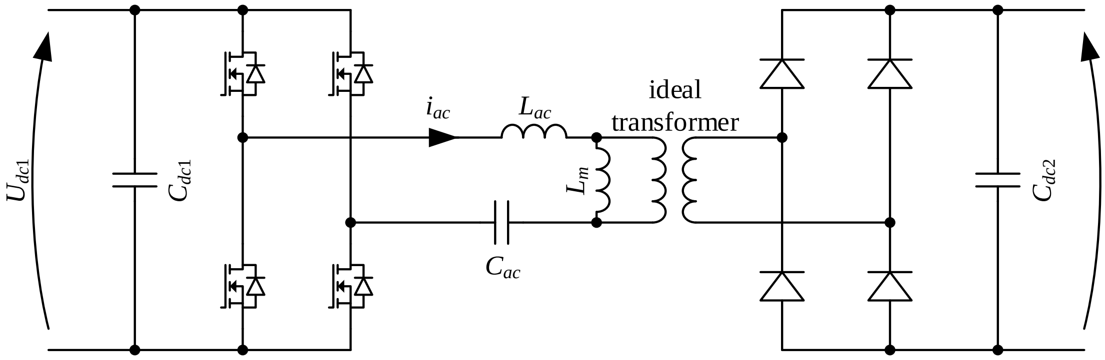

Fig. 2.9. LLC DC-DC resonant converter (LLC)

The FSFB is composed of a VSC, transformer and diode bridge with LC filter ($L_{dc}$, $C_{dc2}$) as presented in Fig. 2.10. It was proposed in [129]. The topology offers the possibility of avoiding the LC resonant circuit which may cause technological challenges in high power applications.

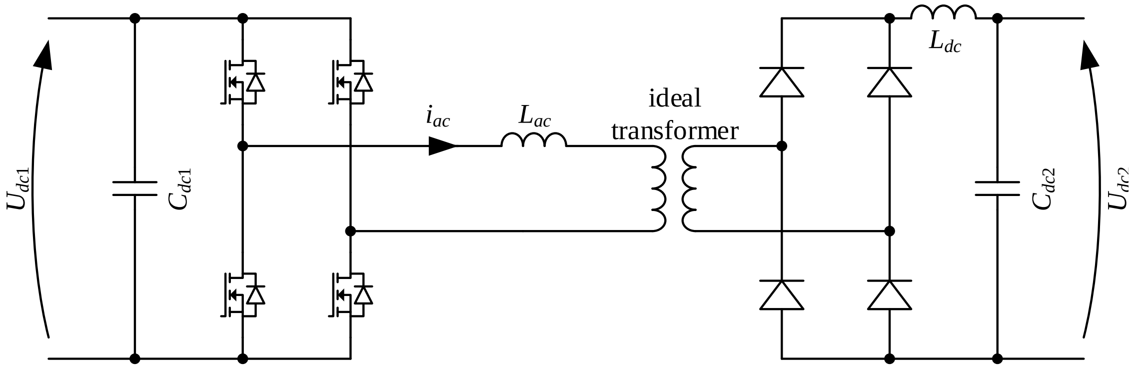

Fig. 2.10. Phase-shifted full bridge (FSFB)

The DAB was invented by De Doncker near 1989 and the patent [27] was granted in 1991. The DAB is composed of two VSCs connected with a transformer and it should be mentioned that the operation of the DAB requires the use of two VSCs. The DAB circuit diagram is presented in Fig. 2.11.

If the rectifier is replaced with a diode bridge then the topology is referenced as a single active bridge (SAB) [80].

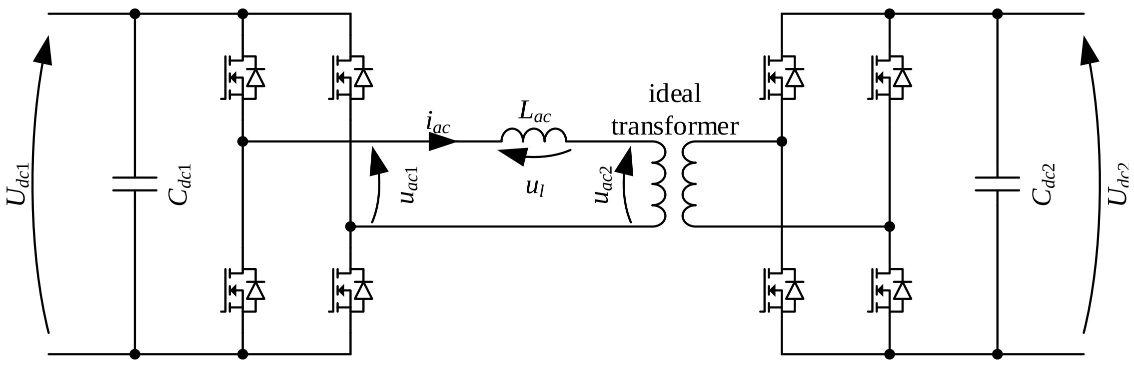

Fig. 2.11. Dual active bridge (DAB): $u_{ac1}$ primary AC voltage, $u_{ac2}$ secondary AC voltage referenced to primary, $u_l$ voltage across $L_{ac}$

The DAB can be seen as a generalized isolated DC-DC converter topology allowing to be easily transformed into:

- SAB - with the rectifier bridge not being controlled,
- FSFB - with the additional DC inductor $L_{dc}$ and the rectifier bridge not being controlled,
- SRC - with an additional resonant capacitor $C_{ac}$ and the rectifier bridge not being controlled,
- LLC - with an additional resonant capacitor $C_{ac}$, carefully designed magnetizing inductance $L_m$ and the rectifier bridge not being controlled

while adapting the converter design and control. For this reason, the DAB will be further analysed.

## 2.3. Dual active bridge converter

The operation of the DAB is based on the phase shift $\delta$ between the two VSCs. The variety of modulation techniques was analysed in [94] and the rectangular modulation has been selected for the further study. The rectangular modulation assumes the 50% duty cycle and the only controlled variable is the phase shift $\delta$. The idealised waveforms are presented in Fig. 2.12 and they correspond to the variables defined in Fig. 2.11. For the simplicity of analysis, it is considered the transformer ratio equal to 1.

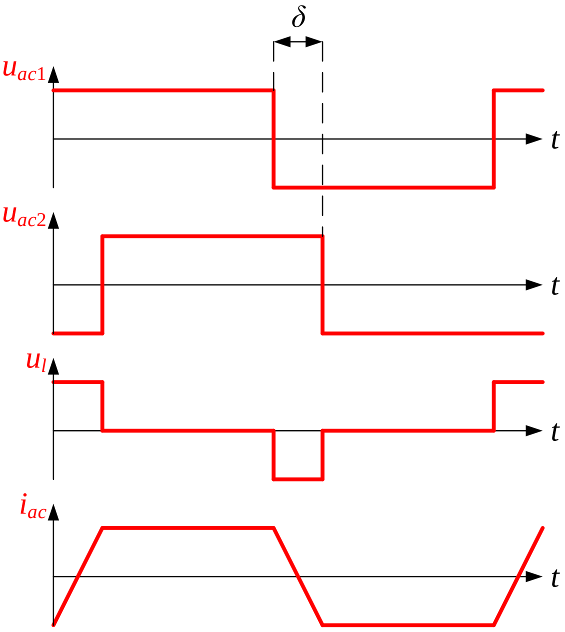

Fig. 2.12. Idealised waveforms of the DAB with $U_{dc1}=U_{dc2}$ operating with the rectangular modulation

According to [25] the power flow analysis can be performed using the fundamental frequency model presented in Fig. 2.13. The fundamental frequency is equal to the switching frequency *f*.

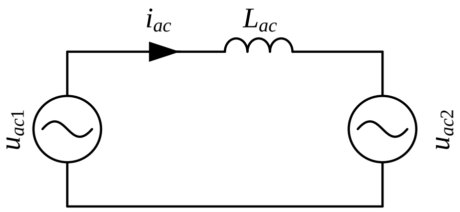

Fig. 2.13. Fundamental model of the DAB

The power flow is defined by the equations:

$$P_{ac} = \frac{U_{ac1} U_{ac2}}{2\pi f L_{ac}} \sin\delta \tag{2.1}$$

$$Q_{ac} = \frac{U_{ac1}}{2\pi f L_{ac}} (U_{ac1} - U_{ac2} \cos\delta) \tag{2.2}$$

where $U_{ac1}$ is the RMS value of the $u_{ac1}$ fundamental defined by:

$$U_{ac1} = \frac{2\sqrt{2}}{\pi} U_{dc1} \tag{2.3}$$

where $U_{dc1}$ is the input DC bus voltage. The $U_{ac2}$ is defined accordingly.

The conclusion of [25], [57], [94], [195] was that for the high power applications, where the very high power density is required, a 3-phase DAB (DAB3) is an interesting candidate. In [57], [94] the multiphase DAB was analysed but no significant gain was demonstrated compared to the DAB3. The main advantages of the DAB3 compared to the single-phase DAB are the following:

- the DC capacitor size can be reduced thanks to the $2\pi/3$ phase shift in the voltage ripple,
- for a given rating of the power semiconductor switch the converter power is higher thanks to natural current paralleling,
- the turn off current of the power semiconductor switch is lower,
- the magnetic circuit of the transformer is more compact,
- the voltage and current harmonics are lower resulting in lower transformer power loss,
- the transformer vector group can be chosen to optimize the converter design.

The DAB3 is composed of two 3-phase VSCs connected with a 3-phase transformer. The DAB3 circuit diagram is presented in Fig. 2.14. The DAB3 in the asymmetric monopole configuration and the transformer Yy vector group is detailed in Fig. 2.15.

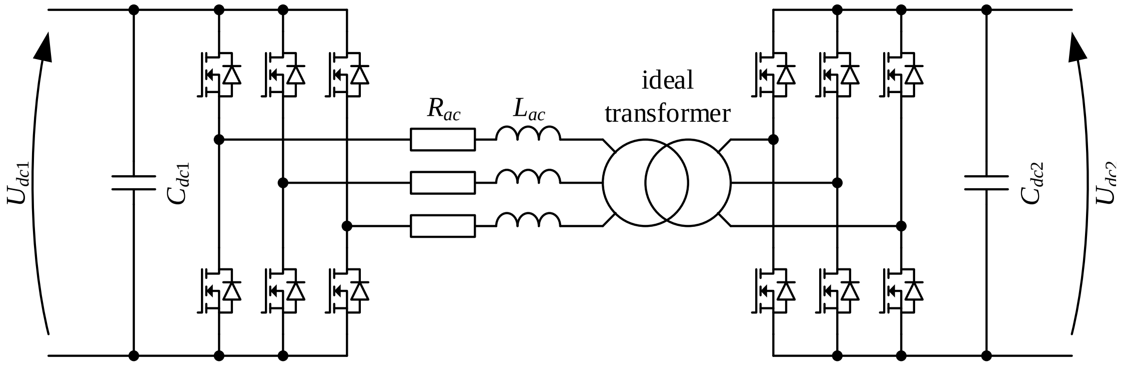

Fig. 2.14. 3-phase dual active bridge (DAB3): $R_{ac}$ AC resistance

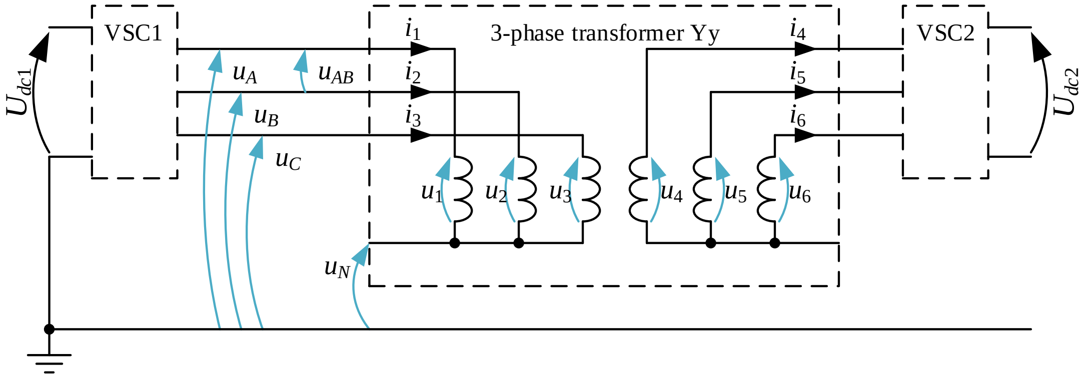

Fig. 2.15. 3-phase DAB in the asymmetric monopole configuration with Yy transformer: $u_A$, $u_B$, $u_C$ phase-ground voltage, $u_{AB}$ phase-phase voltage, $u_N$ star point-ground voltage, $u_1$, $u_2$, $u_3$ primary phase voltage, $u_4$, $u_5$, $u_6$ secondary phase voltage, $i_1$, $i_2$, $i_3$ primary phase current, $i_4$, $i_5$, $i_6$ secondary phase current

For a 3-phase VSC we can assume that the sum of 3 phase-ground voltages $u_A$, $u_B$, $u_C$ equals a non-zero voltage with respect to ground $u_X$:

$$u_A + u_B + u_C = u_X \tag{2.4}$$

It can be easily proven that the sum of phase-phase voltages is equal to zero:

$$u_{AB} + u_{BC} + u_{CA} = 0 \tag{2.5}$$

and therefore, considering the isolated star point, the sum of all transformer phase-neutral voltages is equal to zero:

$$u_1 + u_2 + u_3 = 0 \tag{2.6}$$

Thanks to the above statements we can prove that:

$$u_N = \frac{1}{3} u_X \tag{2.7}$$

and

$$u_1 = \frac{u_{AB} - u_{CA}}{3} \tag{2.8}$$

Analogically we can calculate $u_2$ and $u_3$. According to the equations above and assuming the rectangular modulation, the voltage waveforms can be plotted as presented in Fig. 2.16.

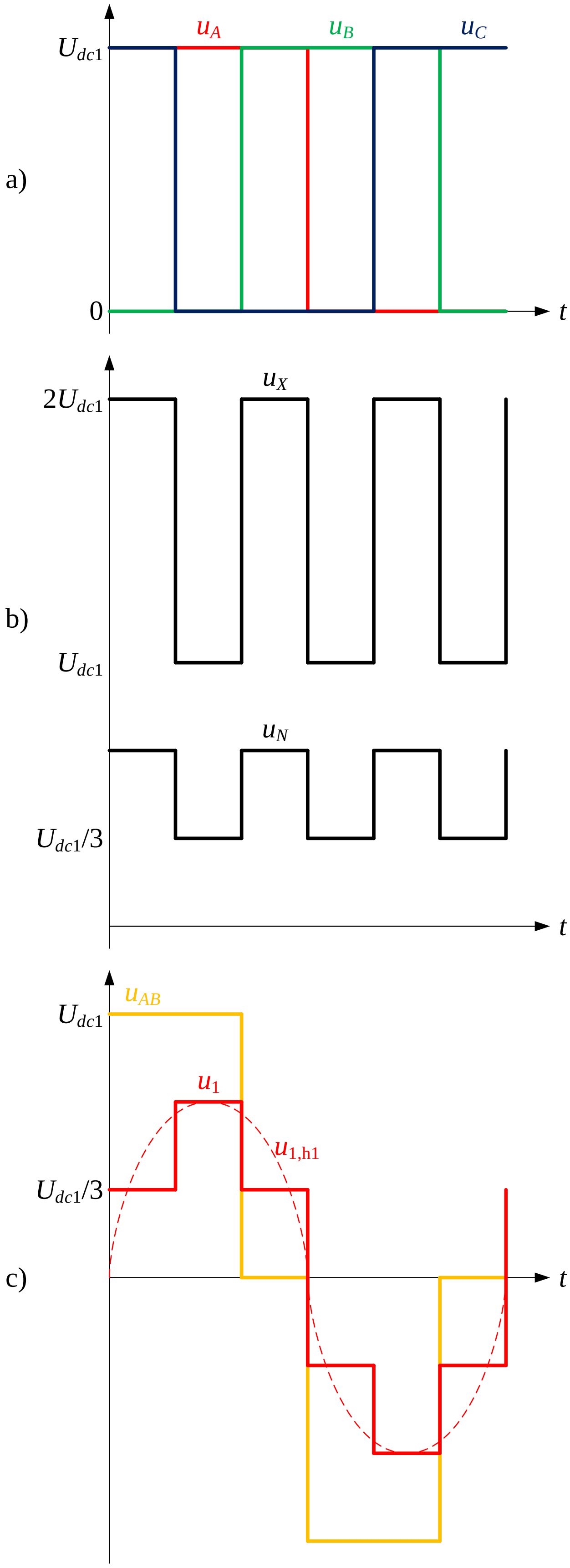

Fig. 2.16. Idealised waveforms of the DAB3, VSC1: a) VSC phase-ground voltage, b) sum of VSC phase-ground voltages and transformer star point-ground voltage, c) transformer phase-phase voltage and phase-neutral voltage and its fundamental

Using the Fourier transform, the RMS value of the voltage fundamental can be calculated. Assuming the same RMS voltage in each phase, the primary phase-neutral voltage is:

$$U_{ac1} = \frac{\sqrt{2}}{\pi} U_{dc1} \tag{2.9}$$

and the secondary phase-neutral voltage $U_{ac2}$ is defined accordingly. Finally, the power flow is defined by the equations:

$$P_{ac} = 3 \frac{U_{ac1} U_{ac2}}{2\pi f L_{ac}} sin\,\delta \tag{2.10}$$

$$Q_{ac} = 3 \frac{U_{ac1}}{2\pi f L_{ac}} (U_{ac1} - U_{ac2}\,cos\,\delta) \tag{2.11}$$

A similar analysis can be performed for the phase-phase voltage and it can be proven that the primary phase-phase voltage $U_{ac1\Delta}$ is:

$$U_{ac1_{\Delta}} = \sqrt{3} U_{ac1} \tag{2.12}$$

The phase current can be calculated neglecting the $R_{ac}$ according to:

$$L_{ac} \frac{di_1}{dt} = u_1 - u_4 \tag{2.13}$$

## 2.4. Power semiconductors

The performance of any power electronics converter is primarily defined by the performance of the power semiconductor device. The development of new power semiconductors represents the investments of billions of euros so the converter designs follow the evolution of power semiconductor market.

In high power applications the most common power semiconductors are the silicon thyristor and IGBT (Fig. 2.17). The thyristors offer higher blocking voltage and higher nominal current ratings, up to 8 kV and 4 kA [77]. The press-packs are used offering a good electrical and thermal interface. The light-triggered press-packs are available which is practical in series connection of thyristors. However, a special mechanical interface ensuring the mechanical integrity is required with the right pressure at all operating conditions. The IGBTs are available in power module housing [78] where the individual semiconductor dies are connected in parallel, often using bonding wires. In some HVDC and railway applications the 3.3 kV / 1.5 kA IGBT power modules are used.

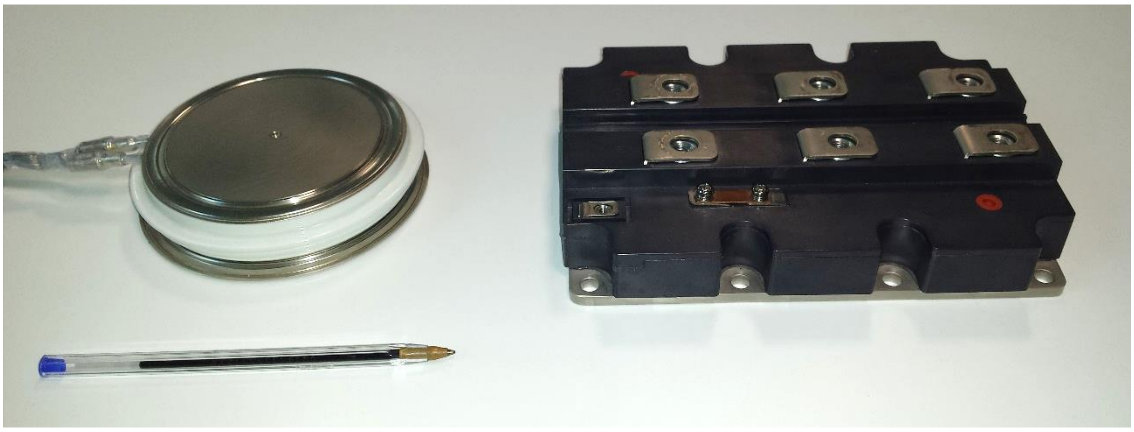

Fig. 2.17. Thyristor press-pack (left) and IGBT module (right)

Since few decades, the new wide band gap (WBG) semiconductors such as silicon carbide (SiC) and gallium nitride (GaN) have been developing. The band gap is the energy gap between the valence band and the conduction band which is approximately 3 eV for the SiC. In Fig. 2.18 the material properties of SiC and GaN are compared against the Si. The WGB semiconductors offer the higher blocking voltage, higher operating temperature and faster switching.

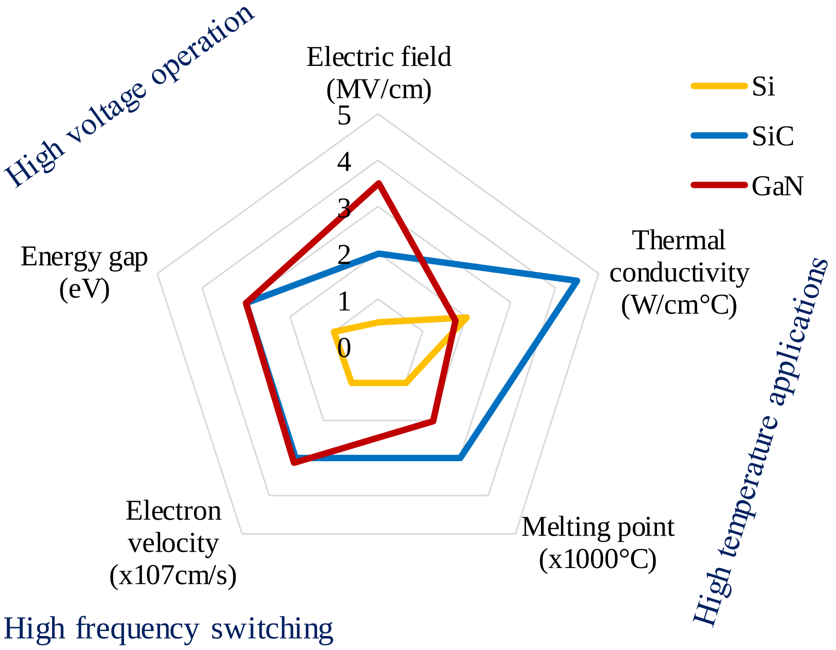

Fig. 2.18. Summary of Si, SiC, and GaN relevant material properties [123]

Today, the SiC power semiconductors are commercially available up to 1.7 kV / 325 A [190] with the MOSFET and Schottky diodes. The devices with higher blocking voltage, up to 15 kV are feasible [191] but the market demand is too low for the SiC offer to develop. For the time being we cannot really benefit from the higher blocking voltage. Moreover, the on-state resistance of the MOSFET increases 2 times from 25°C to 150°C [190]. Thus, the possible high temperature operation has no practical usage in high efficiency applications. The most significant gain of SiC devices compared to Si is the important decrease in the switching power losses. It can either allow to operate the power electronics converters at higher frequency or to decrease the power losses while keeping the same frequency.

## 2.5. Medium frequency transformer

In AC power systems, the transformers allow to adjust the level of voltage between the power generation, transmission and distribution. Moreover, the transformer offers the galvanic separation between two AC circuits. The 50/60 Hz transformers are usually realised with laminated silicon-iron steel sheets, copper or aluminium windings and oil or resin insulation [142]. This technology is industrially mature with more than 100 years of return of experience but still attracting lots of research interest [199], [200].

The low voltage "electronic transformers" has driven the development of isolated DC-DC converters. Multiple advantages have led to the development of a novel technology - the high frequency transformer (HFT). The Faraday's law of induction shows the benefit of increasing the transformer frequency - the magnetic circuit cross section is inversely proportional to the frequency. In addition, knowing that the transformer cost is roughly proportional to its weight, we see a clear benefit in developing the HFT, the isolated DC-DC converter and the solid-state transformer. They are simply smaller, lighter and cheaper. The evolution of the domestic DC power supplies clearly shows this trend (Fig. 2.19).

Fig. 2.19. Illustrative comparison between a 50 Hz transformer-rectifier (top left) and a solid-state transformer (bottom right)

The low power HFT is nowadays quite mature but the high power MFT and HFT are still within the domain of research with only some industrial applications. However, it is expected that more industrial applications will require the MFT/HFT due to the evolutions of power systems and transportation as explained in §2.1. For the purpose of this work, in high power isolated DC-DC converters, let's assume that the medium frequency is higher than 1 kHz and lower than 100 kHz.

The magnetic circuit of MFT can be realised with different geometrical structures: core type [180], shell type [124], matrix [135] or coaxial [90]. In [13] the different core structures have been compared and it was concluded that for the high power MFT the core type structure offers the lowest losses.

The choice of MFT magnetic core material shall be done according to the material properties and cost. The performance factor, which is defined as a product of the frequency and flux density at a specified core power loss density, is used to compare different types of core materials [74], [179]. The amorphous and especially nanocrystalline materials are preferred in the low and medium frequencies due to the high flux density. The main advantage of ferrite cores is their low power loss, which makes them an attractive material for the construction of medium and high frequency transformers [12], [164]. The ferrite also offers low cost in terms of material and transformer assembly. In [162] the ferrite core MFT is considered for the DC-DC converters operating above a few kHz. Finally, the ferrite seems as a good candidate for the short-term industrialization of high power MFT.

The design of MFT winding has to take into account the skin and proximity effects. The skin effect is due to opposing eddy currents induced by the changing magnetic field resulting from the alternating current flow in the conductor. The electric current flows mainly between the outer surface and a level called the skin depth:

$$\delta_{se} = \sqrt{\frac{1}{\pi f \mu \sigma}} \tag{2.14}$$

where $f$ is the current frequency, $\mu$ is the conductor permeability and $\sigma$ is the conductor conductivity. For example, for a copper wire at 20 kHz the skin depth is 0.5 mm. Considering a high power MFT it is clear that the wire diameter will be larger than the skin depth. The proximity effect is due to opposing eddy currents induced by the changing magnetic field resulting from the alternating current flow in nearby conductors. The result is that the current is concentrated in the areas of the conductor farthest away from nearby conductors carrying current in the same direction. In MFT applications three types of conductors are used:

- litz wire - it consists of many thin wire strands, individually insulated and twisted or woven together, following one of several carefully prescribed patterns,
- foil - it is a flexible sheet of copper or aluminium covered with insulation material.
- tube - it is a hollow insulated wire which in addition to current conduction may provide a path for cooling liquid [69].

Each conductor technology comes with a defined cost/performance ratio. The foil winding is the cheapest but it causes a large parasitic capacitance of the winding. The tube conductor requires a specific manufacturing process and results with the significant conductor diameter. The litz wire offers a good performance but it comes with a relatively high cost.

The insulation of MFT may be ensured by solid or liquid material. The solid insulation offers the dielectric strength of some tens of kV/mm. Usually it is realised by the impregnation of a material placed between the windings. In case of a breakdown the insulation material is definitively damaged. The advantage of the solid insulation is a limited maintenance. The liquid insulation, in addition to its primary function offers a good cooling. A liquid-insulated transformer would be generally smaller than a solid-insulated one. However, the liquid insulation requires more maintenance effort and depending on the liquid used it may be more or less environmentally friendly. In MFT design, the high frequency effect on insulation material should be taken into account [16], [65].

The cooling of the MFT may be ensured by the natural or forced air convection or liquid cooling [136]. The liquid cooling offers the best performance but it requires more complex cooling system and more important maintenance effort. The liquid cooling may be considered where a very high-power density is required or if the liquid cooling participates in the insulation. The thermal design of MFT is very challenging due to the high-power loss density of a small size MFT.

# 3. Modelling of medium frequency transformer

## 3.1. Introduction to modelling methods

The modelling of transformers has been extensively studied for the electromagnetic transient simulations of power systems. However, in the modern power systems: HVDC grids, smart grids, photovoltaic power plants, wind power plants and electric vehicle charging, the transformer is usually a component of the isolated DC-DC power converters [4], [34], [38], [63], [181]. Considering the 3-phase DAB detailed in §2.3, the transformer design is different from the grid connected transformers, considering in particular the operating frequency that can be much higher than 50/60 Hz and the non-sinusoidal voltage and current waveforms. The modelling requirements differ accordingly.

The transformer modelling methods can be categorised in: electromagnetic field computation-based methods, equivalent circuit-based methods and hybrid methods. The most common technique of solving the electromagnetic field is the finite element method (FEM) [32]. Other techniques are also used including the finite difference method which has been used since more than 60 years and the boundary element method. According to [76], in the FEM, the solution domain is divided into small subdomains, called finite elements. The FEM can be applied to 2D and 3D domains [33]. The size of the elements can be variable in the domain. Smaller finite elements can be used in the regions where we anticipate larger variations in fields. Each finite element can contain a different material so the element boundaries must coincide with the interface between materials. The collection of elements forms a mesh. In 2D FEM the intersection of two edges is called a node. The FEM modelling of transformers allows to make precise multi-physics analysis, including electromagnetic, mechanical, thermal, etc. However, the FEM simulations require significant computational effort what makes it impractical in the analysis of large electrical systems, including the power converters and power systems. The equivalent circuit model simplifies the calculations what makes the analysis of large electrical systems more convenient. A simple linear transformer model enables a rapid analysis of isolated DC-DC converters as it was presented in chapter 2. However, such a model has many limitations in different analyses which should take into account: nonlinearity, power losses and frequency effects.

A precise equivalent circuit model of a medium frequency transformer suitable in power converter transient analysis should take into account:

- the winding inductances - involving self and mutual values which include at least:
    - the leakage inductances - they have a major influence on the operation of isolated DC-DC converters, DAB in particular,
    - the magnetizing inductances - they have an influence on the transient analysis of isolated DC-DC converters and play an important role in the LLC DC-DC resonant converter operation,
- the winding resistances - they model the power losses in the windings,
- the equivalent resistance for the modelling of power losses in the core including:
    - hysteresis effects,
    - eddy current effects,
- the winding capacitances - involving self and mutual values.

The transformer equivalent circuit models can be categorized into distributed and lumped parameter types. The distributed parameter models are used in the analysis of electromagnetic wave propagation based on the transmission line theory. The model taking into account the transformer winding capacitances was proposed in [147] and has been further extended in the scientific literature, including [31], [154]. In [72], a distributed parameter model of a buck converter was presented.

The lumped parameter models allow to analyse geometrically complex structures based on *R*, *L* and *C* elements, where the inductance and capacitance may involve self and mutual values. In the most advanced models, a lumped element may correspond to a physical transformer element, for example a winding turn or layer. Detailed lumped parameter models were proposed in [28], [48], [105], [153]. These models are suitable for high frequency analysis of internal transformer voltages and currents.

The lumped parameter models can also be applied in magnetic core modelling based on magnetic reluctance. The equations of the magnetomotive force (MMF) and the magnetic flux can be transformed to an equivalent electric circuit [157], [174], [189]. The reluctance model can involve a magnetic hysteresis [35]. A hybrid model based on lumped electric and magnetic parameters suitable in electromagnetic transient simulation was proposed in [127], [128].

The power system analysis, obviously including transformers, has been widely studied in the Electromagnetic Transient Program (EMTP) [116]. The leading simulation software are EMTP [46] and PSCAD [113]. In power system analyses, interest is usually focused on transformer's terminal voltages and currents, while neglecting its internal voltages and currents. In [29], [103], [134], methods were proposed to simplify the detailed models, to make them more suitable in power system analyses. In case a detailed model is not available, some measurement techniques can be used to establish the model in time or frequency domain [89], [125], [167], [176], [192], [193].

Many transformer models for power system transient analysis neglect magnetic nonlinearity. The nonlinear 3-phase transformer model built as three single-phase transformer models makes the analysis of transient states imprecise. The majority of nonlinear 3-phase transformer models neglect the effects of cross couplings between different limbs due to saturation, even if the magnetic cross saturation has been well studied in rotating electrical machines [21], [177]. In [36], a 3-phase 50 Hz transformer model including magnetic cross saturation was proposed. The authors of [36] claim that their model is superior when compared to a classical nonlinear model based on three single-phase transformers and neglecting magnetic cross saturation, since it allows to analyse precisely the transformer inrush and fault conditions.

This dissertation proposes an equivalent circuit model of an isolated DC-DC converter with a 3-phase medium frequency transformer. The model is developed according to the Lagrange energy method described in [120], [184]. This method was applied to the transformer modelling in [188]. In [133], [175], it was used to model magnetic components of power converters allowing to derive a physically motivated model. The proposed nonlinear MFT model is composed of magnetizing and leakage inductance matrices including self and mutual values according to [45], [171]. The inductances are calculated based on the magnetic flux multi-dimensional characteristic $\mathbf{\Phi}(\mathbf{\Theta})$. The model takes into account the magnetic cross saturation. The magnetic hysteresis model is developed based on the feedback Preisach model.

## 3.2. Model derivation

### 3.2.1. General transformer model

The general model of the 3-phase core type MFT is presented in Fig. 3.1. On each column there are 3 windings representing the primary, secondary and additional equivalent circuit for core power loss. Each winding is modelled with the lumped resistance *R* and the flux linkage

*Ψ*(**i**). The core power loss related to hysteresis and eddy current effects is modelled with an equivalent circuit composed of three additional coils. The winding capacitance is neglected since it has a minor effect on the no-load and full-load tests of the considered MFT, what will be presented later in this dissertation.

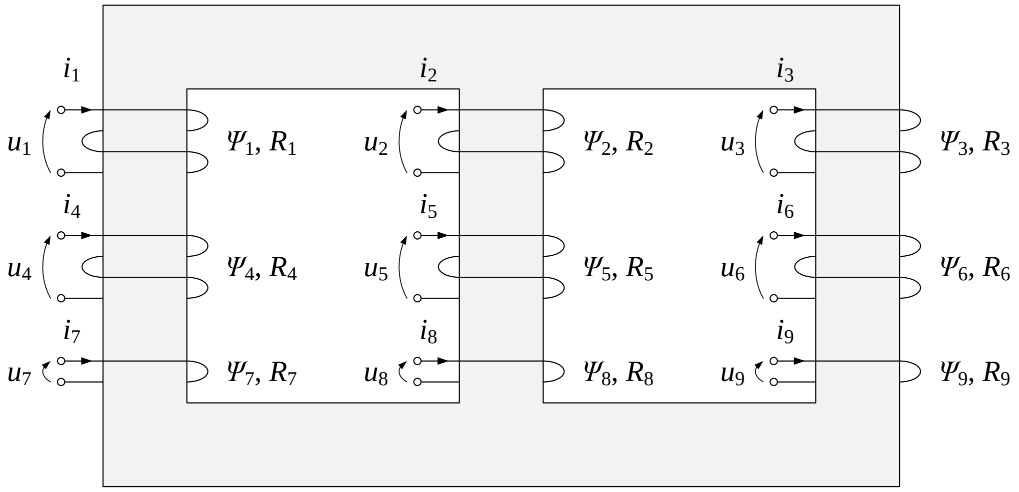

Fig. 3.1. General model of 3-phase MFT with primary winding 1-3, secondary winding 4-6, and equivalent circuit 7-9 for core power loss

The system can be described with the equation:

$$\frac{d}{dt}\mathbf{\Psi}(\mathbf{i}) + \mathbf{Ri} = \mathbf{u}(t) \tag{3.1}$$

where

$$\mathbf{u} = [u_1 \quad u_2 \quad \cdots \quad u_9]^{\mathrm{T}} \tag{3.2}$$

$$\mathbf{i} = [i_1 \quad i_2 \quad \cdots \quad i_9]^{\mathrm{T}} \tag{3.3}$$

$$\mathbf{\Psi}(\mathbf{i}) = [\Psi_1(\mathbf{i}) \quad \Psi_2(\mathbf{i}) \quad \cdots \quad \Psi_9(\mathbf{i})]^{\mathrm{T}} \tag{3.4}$$

$$\mathbf{R} = \begin{bmatrix} R_1 & 0 & \cdots & 0 \\ 0 & R_2 & \cdots & 0 \\ \vdots & \vdots & & 0 \\ 0 & 0 & 0 & R_9 \end{bmatrix} \tag{3.5}$$

The flux linkage *Ψ*(**i**) is a nonlinear function of all transformer currents. The time derivative of the flux linkage vector **Ψ**(**i**(*t*)) defines the electromotive force in each winding and can be expressed as the matrix of dynamic inductances $\mathbf{L_d}$:

$$\frac{d}{dt}\mathbf{\Psi}\big(\mathbf{i}(t)\big) = \begin{bmatrix} \frac{\partial \Psi_1}{\partial i_1} & \cdots & \frac{\partial \Psi_1}{\partial i_9} \\ \vdots & & \vdots \\ \frac{\partial \Psi_9}{\partial i_1} & \cdots & \frac{\partial \Psi_9}{\partial i_9} \end{bmatrix} \frac{d}{dt}\begin{bmatrix} i_1 \\ \vdots \\ i_9 \end{bmatrix} = \mathbf{L_d}(\mathbf{i})\frac{d}{dt}\mathbf{i} \tag{3.6}$$

According to [45], [171], it can be assumed that the matrix of dynamic inductances $\mathbf{L_d}$ contains a nonlinear term resulting from core magnetization and a linear term resulting from flux leakage. The flux linkage can be represented as follows:

$$\Psi_k(\mathbf{i}) = N_k \Phi_k\big(\mathbf{\Theta}(\mathbf{i})\big) + \sum_{n=1}^{9} L_{\sigma k,n} i_n \tag{3.7}$$

where $k$=1, 2, ..., 9 is the winding index, $N$ is the number of turns, and

$$\mathbf{\Theta} = [i_1 N_1 \quad i_2 N_2 \quad \cdots \quad i_9 N_9]^{\mathrm{T}} \tag{3.8}$$

A further assumption is made that there is a magnetizing flux $\mathbf{\Phi_m}$ which is coupled with all windings:

$$\mathbf{\Phi_m} = \begin{bmatrix} \Phi_{m1}(\mathbf{\Theta_m}) \\ \Phi_{m2}(\mathbf{\Theta_m}) \\ \Phi_{m3}(\mathbf{\Theta_m}) \end{bmatrix} \tag{3.9}$$

where $\mathbf{\Theta_m}$ is the magnetizing MMF defined as:

$$\mathbf{\Theta_m} = \begin{bmatrix} i_1 N_1 + i_4 N_4 + i_7 N_7 \\ i_2 N_2 + i_5 N_5 + i_8 N_8 \\ i_3 N_3 + i_6 N_6 + i_9 N_9 \end{bmatrix} \tag{3.10}$$

Finally, the matrix of dynamic inductances $\mathbf{L_d}$ is:

$$\mathbf{L_d} = \begin{bmatrix} N_1 \dfrac{\partial \Phi_{m1}}{\partial \Theta_{m1}} N_1 & N_1 \dfrac{\partial \Phi_{m1}}{\partial \Theta_{m2}} N_2 & \dots & N_1 \dfrac{\partial \Phi_{m1}}{\partial \Theta_{m3}} N_9 \\ N_2 \dfrac{\partial \Phi_{m2}}{\partial \Theta_{m1}} N_1 & N_2 \dfrac{\partial \Phi_{m2}}{\partial \Theta_{m2}} N_2 & \dots & N_2 \dfrac{\partial \Phi_{m2}}{\partial \Theta_{m3}} N_9 \\ \vdots & \vdots & & \vdots \\ N_9 \dfrac{\partial \Phi_{m3}}{\partial \Theta_{m1}} N_1 & N_9 \dfrac{\partial \Phi_{m3}}{\partial \Theta_{m2}} N_2 & \dots & N_9 \dfrac{\partial \Phi_{m3}}{\partial \Theta_{m3}} N_9 \end{bmatrix} + \begin{bmatrix} L_{\sigma 1,1} & L_{\sigma 1,2} & \dots & L_{\sigma 1,9} \\ L_{\sigma 2,1} & L_{\sigma 2,2} & \dots & L_{\sigma 2,9} \\ \vdots & \vdots & & \vdots \\ L_{\sigma 9,1} & L_{\sigma 9,2} & \dots & L_{\sigma 9,9} \end{bmatrix} \tag{3.11}$$

The magnetic circuit nonlinearity is involved in $\partial\Phi_m/\partial\Theta_m$ of the first matrix. The author highlights that the leakage inductance matrix includes mutual values.

### 3.2.2. Equivalent circuit model

The equivalent circuit model of an isolated DC-DC converter is presented in Fig. 3.2. In this model, each VSC is modelled with three controlled voltage sources with $U_{dc1}$ or $U_{dc2}$ input. The MFT is connected in Yy vector group. The equivalent circuit for core power loss is included in the model with the resistances $R_7$, $R_8$ and $R_9$. In order to facilitate the further analysis, these resistances are star-connected. Finally, the loop currents $i_{g1}$, $i_{g2}$, ..., $i_{g6}$ are defined.

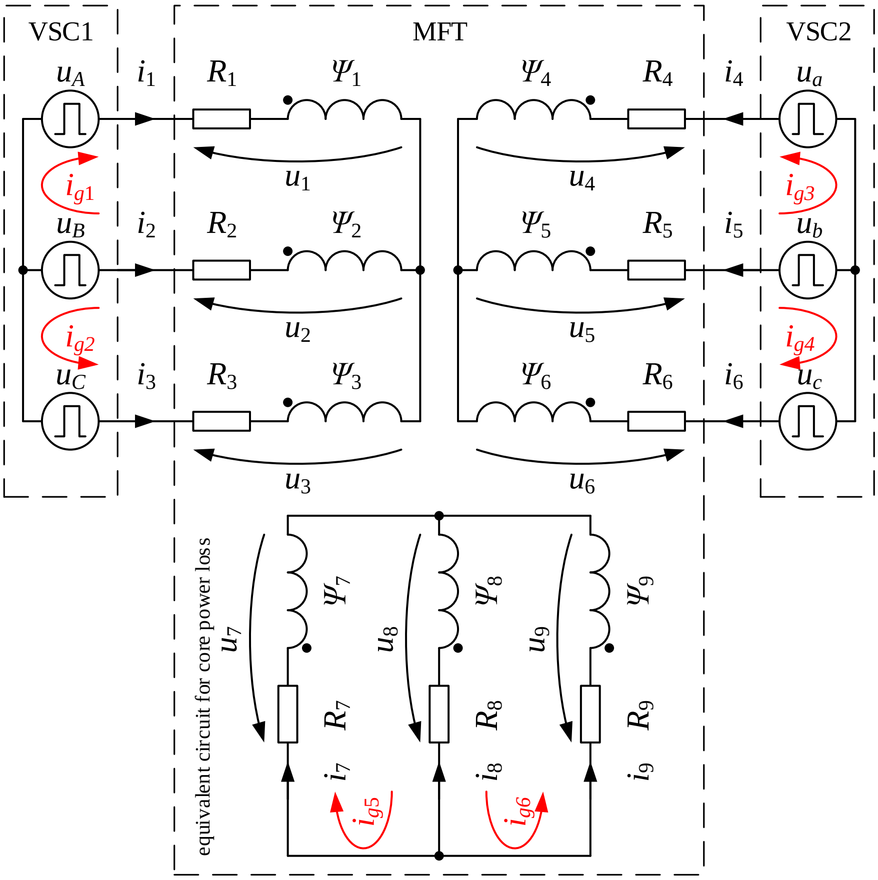

Fig. 3.2. Equivalent circuit model of 3-phase DAB converter including the Yy connected MFT with equivalent circuit for core power loss

### 3.2.3. Lagrange energy method

The transformer model is further developed according to the Lagrange energy method [120], [184]. The Lagrange function and the Rayleigh dissipation function in nongeneralized coordinates are defined as (considering the linear resistance):

$$\mathcal{L}(\mathbf{i}) = \sum_{k=1}^{9} \int_0^{i_k} \Psi_k(\mathbf{i})\, di_k \tag{3.12}$$

$$P_e(\mathbf{i}) = \frac{1}{2} \sum_{k=1}^{9} R_k {i_k}^2 \tag{3.13}$$

The equation of constraints is defined according to Fig. 3.2 as:

$$\mathbf{i} = \mathbf{C}\mathbf{i_g} \tag{3.14}$$

where **C** is the matrix of constraints:

$$\mathbf{C} = \begin{bmatrix} 1 & 0 & 0 & 0 & 0 & 0 \\ -1 & -1 & 0 & 0 & 0 & 0 \\ 0 & 1 & 0 & 0 & 0 & 0 \\ 0 & 0 & 1 & 0 & 0 & 0 \\ 0 & 0 & -1 & -1 & 0 & 0 \\ 0 & 0 & 0 & 1 & 0 & 0 \\ 0 & 0 & 0 & 0 & 1 & 0 \\ 0 & 0 & 0 & 0 & -1 & -1 \\ 0 & 0 & 0 & 0 & 0 & 1 \end{bmatrix} \tag{3.15}$$

and $\mathbf{i_g}$ is the vector of currents representing the set of generalized coordinates:

$$\mathbf{i_g} = [i_{g1} \quad i_{g2} \quad \cdots \quad i_{g6}]^{\mathrm{T}} \tag{3.16}$$

Equation (3.14) is inserted into (3.12) and (3.13) to obtain the Lagrange function and the Rayleigh dissipation function in generalized coordinates.

The general form of the Euler-Lagrange equation system, neglecting the energy stored in capacitances, is:

$$\frac{d}{dt}\frac{\partial \mathcal{L}(\mathbf{i_g})}{\partial i_{gk}} + \frac{\partial P_e(\mathbf{i_g})}{\partial i_{gk}} = Q_k \tag{3.17}$$

where $k$=1, 2, ..., 6, and $Q_k$ is the generalized force defined as:

$$\mathbf{Q} = \begin{bmatrix} u_A - u_B \\ u_C - u_B \\ u_a - u_b \\ u_c - u_b \\ 0 \\ 0 \end{bmatrix} \tag{3.18}$$

The final matrix form of the Euler-Lagrange equation is:

$$\mathbf{M_s}(\mathbf{i_g})\frac{d}{dt}\mathbf{i_g} + \mathbf{R_s}\mathbf{i_g} = \mathbf{Q} \tag{3.19}$$

where

$$\mathbf{R_s} = \begin{bmatrix} R_1 + R_2 & R_2 & \cdots & 0 \\ R_2 & R_2 + R_3 & \cdots & 0 \\ \vdots & \vdots & & \vdots \\ 0 & 0 & \cdots & R_8 + R_9 \end{bmatrix} \tag{3.20}$$

$$\mathbf{M_s} = \begin{bmatrix} \frac{\partial \Psi_1}{\partial i_{g1}} - \frac{\partial \Psi_2}{\partial i_{g1}} & \frac{\partial \Psi_1}{\partial i_{g2}} - \frac{\partial \Psi_2}{\partial i_{g2}} & \cdots & \frac{\partial \Psi_1}{\partial i_{g6}} - \frac{\partial \Psi_2}{\partial i_{g6}} \\ \frac{\partial \Psi_3}{\partial i_{g1}} - \frac{\partial \Psi_2}{\partial i_{g1}} & \frac{\partial \Psi_3}{\partial i_{g2}} - \frac{\partial \Psi_2}{\partial i_{g2}} & \cdots & \frac{\partial \Psi_3}{\partial i_{g6}} - \frac{\partial \Psi_2}{\partial i_{g6}} \\ \vdots & \vdots & & \vdots \\ \frac{\partial \Psi_9}{\partial i_{g1}} - \frac{\partial \Psi_8}{\partial i_{g1}} & \frac{\partial \Psi_9}{\partial i_{g2}} - \frac{\partial \Psi_8}{\partial i_{g2}} & \cdots & \frac{\partial \Psi_9}{\partial i_{g6}} - \frac{\partial \Psi_8}{\partial i_{g6}} \end{bmatrix} \tag{3.21}$$

According to §3.2.1, the matrix $\mathbf{M_s}$ can be split into nonlinear and linear terms, which gives:

$$\begin{aligned} \mathbf{M_s} = & \begin{bmatrix} N_p \frac{\partial \Phi_{m1}}{\partial \Theta_{g1}} N_p - N_p \frac{\partial \Phi_{m2}}{\partial \Theta_{g1}} N_p & \cdots & N_p \frac{\partial \Phi_{m1}}{\partial \Theta_{g2}} N_e - N_p \frac{\partial \Phi_{m2}}{\partial \Theta_{g2}} N_e \\ \vdots & & \vdots \\ N_e \frac{\partial \Phi_{m3}}{\partial \Theta_{g1}} N_p - N_e \frac{\partial \Phi_{m2}}{\partial \Theta_{g1}} N_p & \cdots & N_e \frac{\partial \Phi_{m3}}{\partial \Theta_{g2}} N_e - N_e \frac{\partial \Phi_{m2}}{\partial \Theta_{g2}} N_e \end{bmatrix} \\ & + \begin{bmatrix} L_{\sigma1,1} - L_{\sigma2,1} & \cdots & 0 \\ \vdots & & \vdots \\ 0 & \cdots & 0 \end{bmatrix} \end{aligned} \tag{3.22}$$

where $\mathbf{\Theta_g}$ is the magnetizing MMF in generalized coordinates:

$$\mathbf{\Theta_g} = \begin{bmatrix} \Theta_{g1} \\ \Theta_{g2} \end{bmatrix} = \begin{bmatrix} i_{g1} N_p + i_{g3} N_s + i_{g5} N_e \\ i_{g2} N_p + i_{g4} N_s + i_{g6} N_e \end{bmatrix} \tag{3.23}$$

and $N_p$ is the number of primary turns, $N_s$ is the number of secondary turns, $N_e$ is the number of turns in the equivalent core loss coil. The leakage inductances of the equivalent circuit for core power loss are assumed to be equal to zero.

It is noted that for the Yy transformer, the magnetizing flux $\mathbf{\Phi_m}$ is simplified to:

$$\mathbf{\Phi_m} = \begin{bmatrix} \Phi_{m1}(\mathbf{\Theta_g}) \\ \Phi_{m2}(\mathbf{\Theta_g}) \\ \Phi_{m3}(\mathbf{\Theta_g}) \end{bmatrix} \tag{3.24}$$

being a function of 2 variables ($\Theta_{g1}$ and $\Theta_{g2}$). Consequently, it can be easily analysed and visualized.

## 3.3. Modelling of magnetic hysteresis

### 3.3.1. Review of macroscopic models of hysteresis

The magnetic materials are characterized by the nonlinear relationship $B(H)$ between the magnetic flux density $B$ and the magnetic field strength $H$. The $B(H)$ relationship is history dependent. The shape of the $B(H)$ depends on the material properties and the maximum value of $H$. The hysteresis has a significant effect on the analysis of the transformer inrush, transformer core remanence, resonant circuits involving a transformer and core power loss. A review of different hysteresis models was presented in [107].

The macroscopic models of hysteresis [107] are the most suitable in finite element and equivalent circuit modelling. In the equivalent circuit modelling the hysteresis nonlinearity can be involved directly in the function $\Phi(\Theta)$ [185] or indirectly through the coupled equivalent reluctance model and the function $B(H)$ [35]. The macroscopic models of hysteresis include: Tellinen [169], Stoner-Wolhfart [165], Globus [62], Jiles-Atherton [84] and Preisach [143]. The most accurate models have been considered the Jiles-Atherton model and the Preisach model, especially their modifications [79], [194].

The Jiles-Atherton model can be used in the analysis of electromagnetic, thermal and motion phenomena [66], [81], [112]. It is based on reversible and irreversible components of the total magnetization in the magnetic material. An algorithm and its implementation was presented in [91] allowing to determine the model parameters.

A mathematical form of the Preisach model (PM) was proposed in [92] and further developed in [117]. The PM involves a double integral of Preisach distribution function allowing to calculate the magnetic flux density $B$ as a function of the magnetic field strength $H$. In the PM, the magnetic flux density depends on the magnetic field strength and on the material magnetization history. There have been many modifications of the original PM: generalized PM, moving PM, dynamic PM, vector PM which are reviewed in [79]. In [18], [87] the feedback Preisach model was proposed allowing to gain the accuracy in the hysteresis nonlinearity modelling. In [110] the Preisach model was implemented in a circuit simulation of an isolated DC-DC converter. The Preisach model is selected for further analysis.

### 3.3.2. Feedback Preisach model of hysteresis

The Preisach theory is based on a two-dimensional integration of a function called the Preisach distribution function (PDF) $\mu(\alpha,\beta)$. The PDF is a kind of a material constant defined as a finite weight function having nonzero values within the limits of major hysteresis loop. In the Preisach theory, a ferromagnetic material is made up of an infinite set of rectangular hysteresis operators $\gamma(H)$, each defined with two separate and randomly distributed parameters $\alpha$ and $\beta$. The rectangular hysteresis operator $\gamma(H)$ is presented in Fig. 3.3.

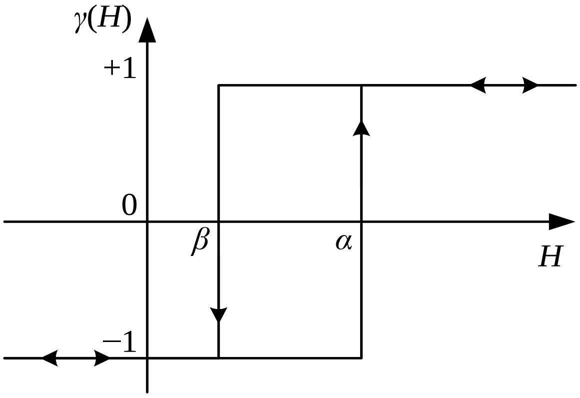

Fig. 3.3. Rectangular hysteresis operator $\gamma(H)$

The classical Preisach model does not represent precisely the minor hysteresis loops due to the congruency property [87]. The feedback Preisach model (FPM) allows to remove the congruency property. The FPM block diagram is presented in Fig. 3.4 where the upper block represents the classical Preisach model and the lower block represents the feedback function.

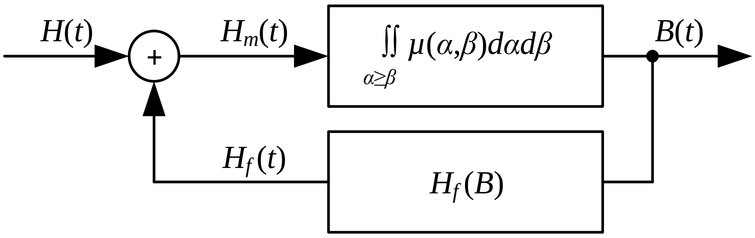

Fig. 3.4. Block diagram of the feedback Preisach model of hysteresis

The FPM with the PDF $\mu(\alpha,\beta)$ and the feedback function $H_f(B)$ is defined as:

$$B(t) = \iint_{\alpha\geq\beta} \mu\big[\alpha + H_f(B), \beta + H_f(B)\big]\gamma_{\alpha,\beta}\big[H + H_f(B)\big]\, d\alpha d\beta \tag{3.25}$$

In order to implement the FPM, it is necessary to determine the PDF $\mu(\alpha,\beta)$ and the feedback function $H_f(B)$. Some methods have been proposed in [30], [118], [144]. In this dissertation the PDF is approximated by a $N$-term two-dimensional Gauss functional series and the feedback function is a 3rd degree polynomial:

$$\mu(\alpha,\beta) = \frac{1}{2\pi}\sum_{n=1}^{N}\frac{A_n}{S_{x,n}S_{y,n}} exp\left(\frac{-(\alpha+\beta)^2}{2{S_{x,n}}^2}\right) exp\left(\frac{-(\alpha-\beta)^2}{2{S_{y,n}}^2}\right) \tag{3.26}$$

$$H_f(B) = K_1 B + K_3 B^3 \tag{3.27}$$

where $A_n$, $S_{x,n}$, $S_{y,n}$, $K_1$ and $K_3$ are constant parameters.

# 4. Design of prototype transformer

## 4.1. Design requirements and constraints

In chapter 2 the benefits and challenges of the 3-phase MFT are presented. According to the author's knowledge, no 3-phase MFT at high power and high frequency has been reported. A 10 kVA 1 kHz 3-phase MFT prototype was reported in [101] and a 2 kVA 100 kHz 3-phase MFT was reported in [132]. A 5 MW DAB3 was presented in [158] but using three single-phase MFTs.

In order to validate this novel and promising technology it has been decided to develop 2 prototypes of the 3-phase MFT according to the main requirements presented in Table 4.1 and according to the constraints of the existing DC-DC 100 kW 1.2 kV 20 kHz converter. The prototypes enable to validate the model developed in chapter 3.

Table 4.1. Main requirements of the 3-phase MFT prototypes

| Requirement | Prototype T1 | Prototype T2 |
|---|---|---|
| Purpose | Flexibility in laboratory tests of DAB converter | Demonstration of small size with high efficiency |
| Ratio | 1 or 0.5 allowing to use different power modules | 1 |
| Vector group | Yy and Dd for DAB converter investigations | Yy |

The DC-DC 100 kW converter was developed at SuperGrid Institute in 2015 [95]. The author was involved in the system design, testing and project management. The converter is based on the DAB topology and it has been designed to operate in single-phase and 3-phase configurations. The nominal power is 100 kW, the input voltage range is 900...1200 V and the step-down ratio is equal to 1 ±10% or 0.5 ±10%. The AC link operates in the frequency range 20 kHz ±3 kHz allowing to optimise the efficiency according to the operating point [97]. The objective efficiency was set to 98% and in [95] there are presented some measurements in single-phase configuration showing a good fit. The cooling of the converter is forced air ensuring the compact size but without a complex water-cooling system. The converter exists in 2 generations:

- generation 1 - based on commercially available SiC MOSFET power modules [190],
- generation 2 - based on SiC MOSFET power modules developed at SuperGrid Institute [95].

The converter prototype generation 2 is approximately a cube of 50 cm and weights 83 kg in single-phase configuration. It is presented in Fig. 4.1. The converter specification is summarised in Table 4.2.

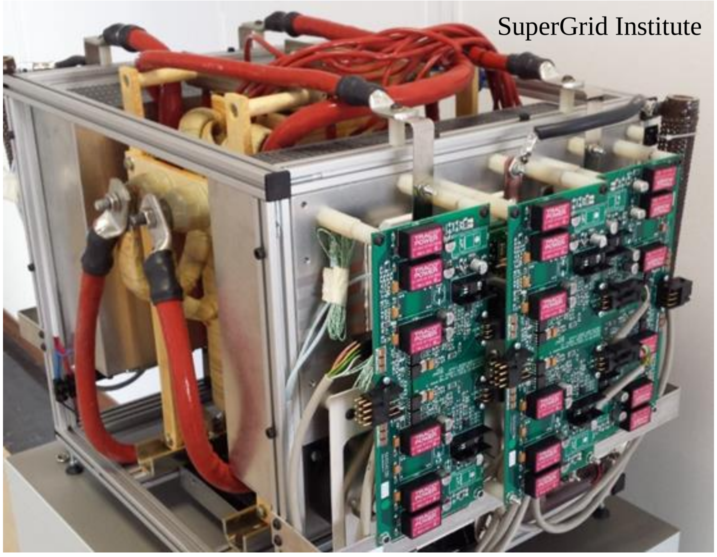

Fig. 4.1. DC-DC 100 kW converter prototype generation 2 with single-phase MFT

Table 4.2. DC-DC 100 kW converter specification

| Parameter | Value |
|---|---|
| Nominal power | 100 kW |
| Nominal input DC voltage | 1200 V |
| Minimum input DC voltage | 900 V |
| Nominal step-down ratio | 1 or 0.5 |
| Maximum converter step down ratio variation | ±10% |
| Maximum operating frequency | 23 kHz |
| Minimum operating frequency | 17 kHz |
| Nominal efficiency | 98% |
| Cooling | Forced air |

In order to perform the comparative analysis between the single-phase and 3-phase MFT it has been decided to use the same core material - MnZn ferrite 3C90 from Ferroxcube [49], even if recently there have been some improvements in ferrite materials. The core-type magnetic circuit was assumed according to [13]. The magnetic circuit has to be assembled from I-cores because C-cores and E-cores do not exist for such big transformers.

It has been observed that the single-phase MFT had quite high winding capacitances causing important undesirable voltage oscillations (Appendix 2). It has been decided to avoid the foil winding and to focus on litz winding.

The control of the DC-DC 100 kW converter was implemented in: microprocessor at 200 µs, FPGA at 20 ns and analogue circuit. According to the controller requirements, it has been evaluated that the minimum phase shift $\delta_{min}$ at the nominal power has to respect the condition:

$$\delta_{min} \geq 2\pi f \cdot 2\ \mu\text{s} \tag{4.1}$$

Thanks to the equation (2.10) one can calculate the minimum value of $L_{ac}$ which is 17 µH for $P_{ac}$ = 100 kW, $U_{dc}$ = 1200 V, $f$ = 20 kHz. It is assumed that the minimum leakage inductance of the MFT should be 15 µH considering 2 µH for the VSC-transformer connection wires.

The design of prototype T2 is presented hereafter and it was reported by the author in [41]. The design of prototype T1 is not presented but the same design process was used.

## 4.2. Preliminary design

The transformer design methodology for power electronics applications was described in [75] and it is well documented in the scientific literature [7], [14], [58], [64], [73], [102], [155]. Due to the high-power density of MFT, the design is highly dependent to the thermal performance. This requires an iterative design process with some preliminary assumptions. This chapter presents the final design iteration result because the MFT design methodology is not in the scope of this work. In [54] the complete MFT design methodology is presented. The presented preliminary design assumes the fundamental frequency model according to [25]. The presented numeric values are rounded.

The preliminary assumptions are gathered in Table 4.3. The assumed current density is rather conservative, even considering the use of litz wire. Accounting the high frequency material as ferrite, the assumed flux density is relatively high.

Table 4.3. Preliminary design assumptions

| Parameter | Value |
|---|---|
| Maximum winding current density | 3 A/mm$^2$ |
| Maximum core flux density | 0.3 T |

The nominal apparent power of the transformer is calculated 150 kVA with:

$$S_n = \sqrt{{P_{ac}}^2 + {Q_{ac}}^2} \tag{4.2}$$

where $P_{ac}$ = 100 kW and $Q_{ac}$ is calculated according to (2.11) for the degraded mode with $U_{dc1}$ = 1200 V and $U_{dc2} = 0.8U_{dc1}$ according to Table 4.2.

The nominal winding current is calculated 90 A thanks to the nominal apparent power (4.2) and the phase voltage (2.9) at the minimum DC voltage $U_{dc1}$ = 900 V. Assuming the current density of 3 A/mm$^2$ (Table 4.3) the winding wire section is set to 30 mm$^2$.

The core cross section can be calculated according to the Faraday's law of induction for sinusoidal excitation:

$$A_c = \frac{\sqrt{2}U_{ac1}}{2\pi f_{min} N_p B_{max}} \tag{4.3}$$

where $U_{ac1}$ is calculated from (2.9) at maximum DC voltage $U_{dc1}$ = 1200 V, $N_p$ is the number of turns which considering 27 V/turn is fixed to 20, $f_{min}$ = 17 kHz and maximum flux density $B_{max}$ = 0.3 T according to Table 4.2 and Table 4.3. Finally, the dimensions of available 3C90 I-cores have to be considered so the core cross section is set to 12.5 cm$^2$.

The arrangement of windings is defined in order to achieve the required leakage inductance $L_f$ = 15 µH. The core dimensions are calculated using simple arithmetic operations. The resulting transformer dimensions are presented in Fig. 4.2 and Fig. 4.3.

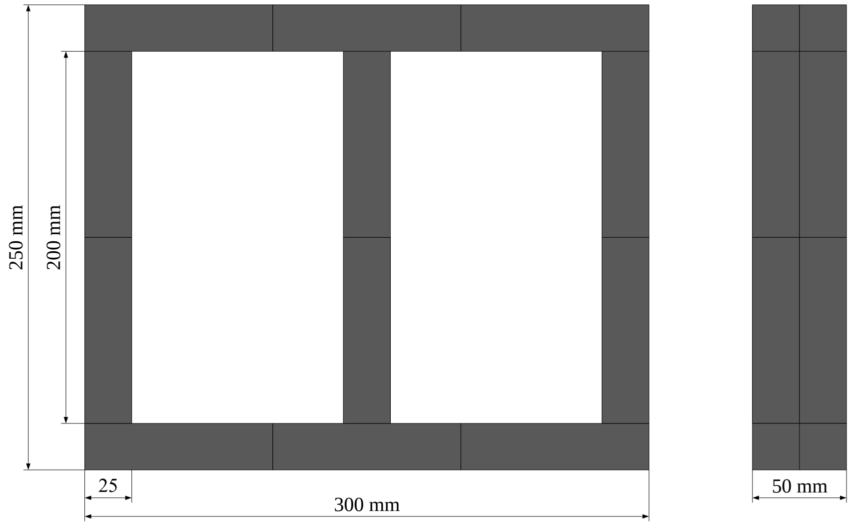

Fig. 4.2. 3-phase MFT core dimensions

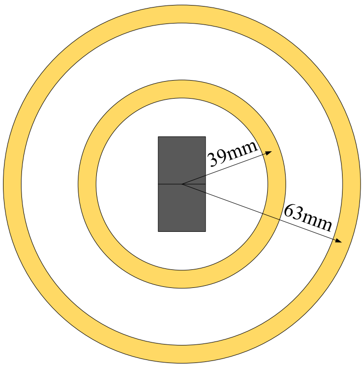

Fig. 4.3. 3-phase MFT winding radius

## 4.3. Winding design and power loss

The DC resistance of transformer winding can be simply calculated based on dimensions. However, the AC resistance is far more complex to calculate due to skin and proximity effects. The analytical equation of AC resistance for foil winding was proposed by Dowell in [37]. In [173] it was proposed the equation for round litz wire. The normalised AC resistance of the litz wire is defined as:

$$K_d = \frac{R_{AC}}{R_{DC}} \tag{4.4}$$

and it is a function of frequency, wire conductivity, wire diameter, number of strands, packing factor and number of winding layers. Obviously the best performance is obtained for the thinnest strand but due to mechanical constraints, for large wires the strand diameter is limited to 0.1 mm. Eventually, the litz wire defined in Table 4.4 has been developed with a specialised industrial partner (Sofilec, France). The single layer winding was selected. The circular winding shape was required due to the high bending radius of the wire.

Table 4.4. Litz wire parameters

| Parameter | Value |
|---|---|
| Strand diameter | 0.1 mm |
| Number of strands | 3870 |
| Nominal cross section | 30.39 mm$^2$ |
| Packing factor | 0.56 |

The evaluation of $R_{AC}$ requires a harmonic decomposition of the winding current in order to calculate the $K_d$ for each harmonic. The idealised winding current can be calculated with (2.13) for two extreme cases according to Table 4.2:

- nominal mode with $U_{dc1} = U_{dc2} = 1200$ V,
- degraded mode with $U_{dc1} = 1200$ V and $U_{dc2} = 0.8U_{dc1}$.

The idealised voltage and current waveforms are presented in Fig. 4.4 for the nominal and in Fig. 4.5 for the degraded mode. The corresponding harmonic decomposition is presented in Fig. 4.6. It can be observed a higher current in the degraded mode but the current harmonic distortion is higher in the nominal mode.

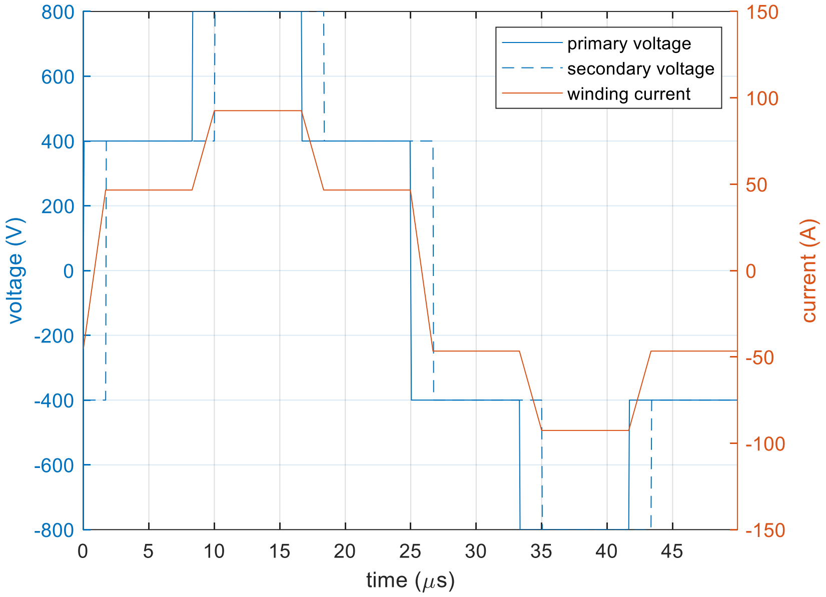

Fig. 4.4. Idealised voltage and current waveforms of the DAB3 for the nominal mode

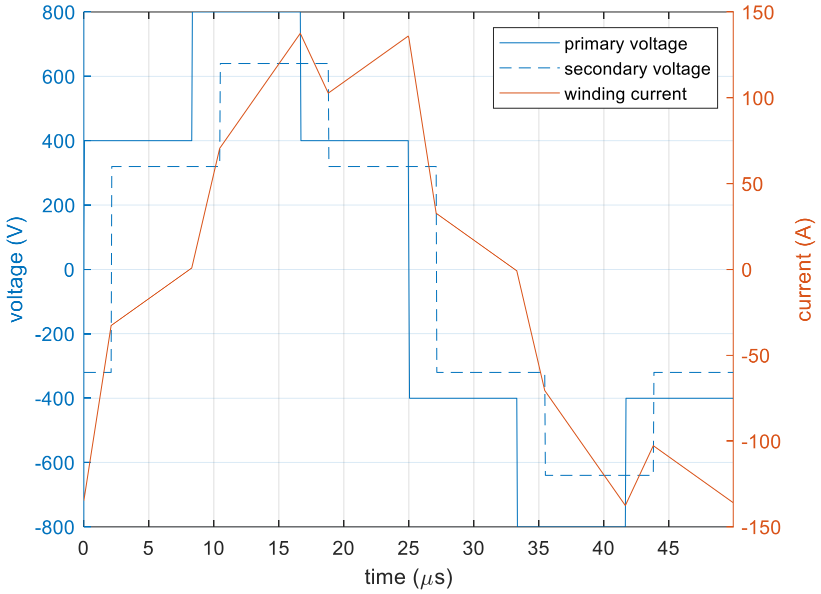

Fig. 4.5. Idealised voltage and current waveforms of the DAB3 for the degraded mode

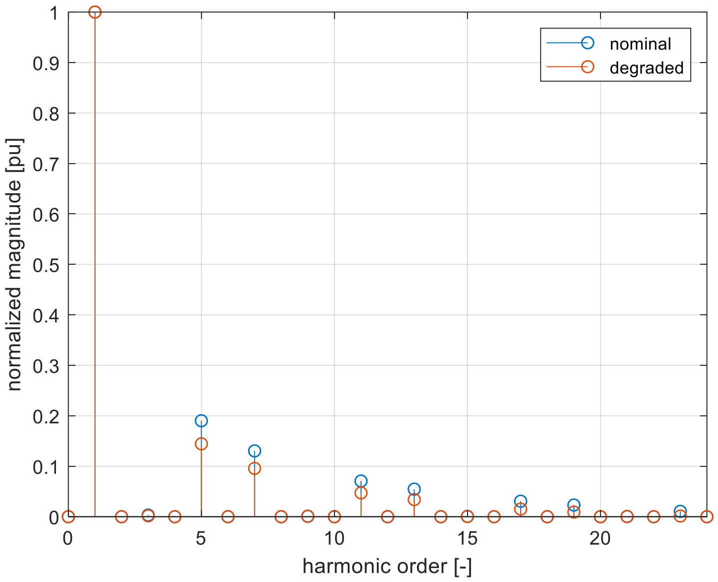

Fig. 4.6. Winding current harmonics of the DAB3 for the nominal mode and degraded mode

Thanks to the current harmonics presented in Fig. 4.6 and the function (2.12) the normalised AC resistance can be calculated for the nominal mode as presented in Fig. 4.7.

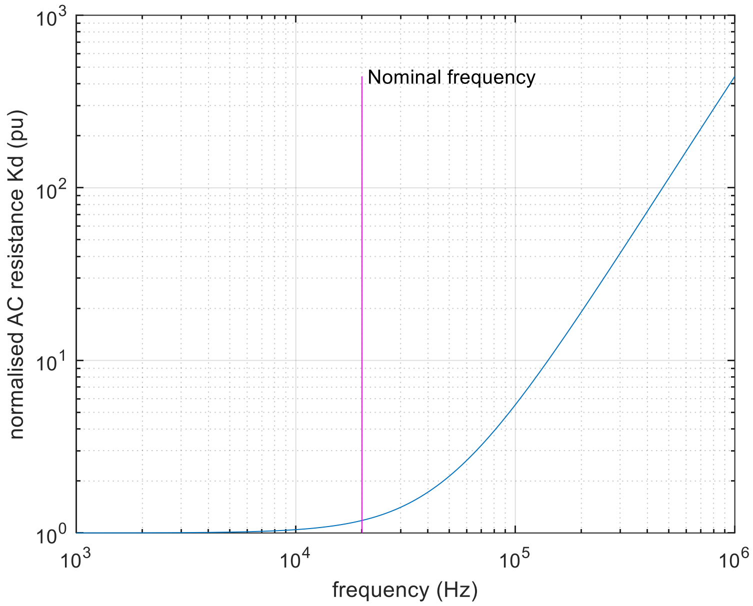

Fig. 4.7. Litz wire normalised AC resistance for the nominal mode at 60°C

Moreover, a current harmonic loss factor can be calculated which shows the excess loss generated by a given harmonic *h*:

$$K_{loss}(h) = \frac{K_{d_h} {I_h}^2}{\sum_{k=1}^{h} {I_h}^2} \tag{4.5}$$

This indicates the effect of current harmonics on the winding loss. The winding with no skin and proximity effect has $K_{loss}$ equal to 1 at the fundamental frequency and 0 at any other harmonic. In the Fig. 4.8 it can be observed that for the selected litz wire the 5th harmonic adds nearly 20% power loss in the nominal mode whereas it is only 10% in the degraded mode. It can also be observed that the harmonics above 13th have a negligible effect on the winding power loss even if the resistance factor $K_d$ is very high according to Fig. 4.7.

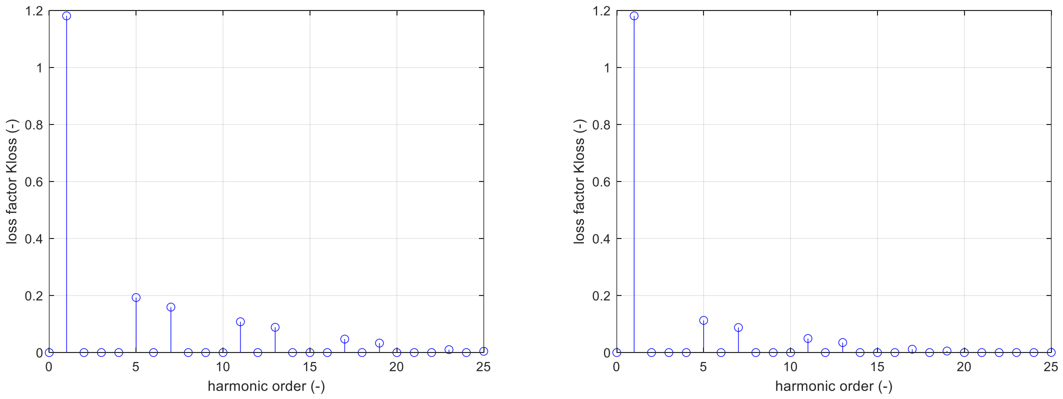

Fig. 4.8. Current harmonic loss factor for the nominal mode (left) and degraded mode (right) at 60°C

Finally, the winding power loss can be calculated for the 6 windings with:

$$P_w = \sum_{k=1}^{6} {I_{RMS}}_k^{\ 2} \, {R_{AC}}_k \tag{4.6}$$

where $I_{RMS\,k}$ is the RMS current of the $k$-th winding.

The winding design parameters are gathered in Table 4.5. The equivalent series resistance is higher in the nominal mode due to higher harmonic distortion. However, the winding RMS current is higher in the degraded mode. Overall, the winding power loss is higher in the degraded mode so this should be considered in the thermal design.

Table 4.5. Winding design parameters at 60°C

| | Nominal mode | Degraded mode |
|---|---|---|
| Equivalent series resistance $R_{ac}$ | 16.5 mΩ | 13.6 mΩ |
| Winding RMS current $I_{RMS}$ | 65 A | 92 A |
| Winding power loss $P_w$ | 206 W | 347 W |

## 4.4. Core design and power loss

The analytical equation of core power loss for sinusoidal excitation was proposed by Steinmetz in [163]. A complete formula taking into account the core temperature is presented in [50] and it is defined as follows:

$$P_{c_{sin}} = k f^{\alpha} {B_{max}}^{\beta} k_T V_c \tag{4.7}$$

$$k_T = c_0 - c_1 T + c_2 T^2 \tag{4.8}$$

where $f$ is the frequency, $B_{max}$ is the maximum flux density, $V_c$ is the core volume, $T$ is the core temperature, $c_x$ are the temperature coefficients and $k$, $\alpha$, $\beta$ are the Steinmetz coefficients presented in Table 4.6.

In [178] it was proposed a modification of power loss formula for non-sinusoidal excitations but still using the Steinmetz coefficients only. The core power loss is defined as:

$$P_c = k_i k_T V_c (2B_{max})^{\beta-\alpha} \frac{1}{T} \int_0^T \left| \frac{u_1(t)}{N_1 A_c} \right|^{\alpha} dt \tag{4.9}$$

where $u_1$ is the primary winding 1 voltage, $T=f^{-1}$, $N_1$ is the number of primary turns, $A_c$ is the core cross section and $k_i$ is defined as:

$$k_i = \frac{k}{2^{\beta+1}\pi^{\alpha-1}\left(0.2761 + \dfrac{1.7061}{\alpha + 1.354}\right)} \tag{4.10}$$

Table 4.6. Ferrite 3C90 Steinmetz coefficients [50]

| Parameter | Value |
|---|---|
| $k$ | 3.2 |
| $\alpha$ | 1.46 |
| $\beta$ | 2.75 |
| $c_0$ | 2.45 |
| $c_1$ | $3.1e^{-2}$ °$C^{-1}$ |
| $c_2$ | $1.65e^{-4}$ °$C^{-2}$ |

The evaluation of core loss requires a knowledge of voltage and flux density waveforms. According to Fig. 2.16 the idealised flux density waveform can be plotted as presented in Fig. 4.9 and the maximum flux density $B_{max} = 0.27$ T is captured.

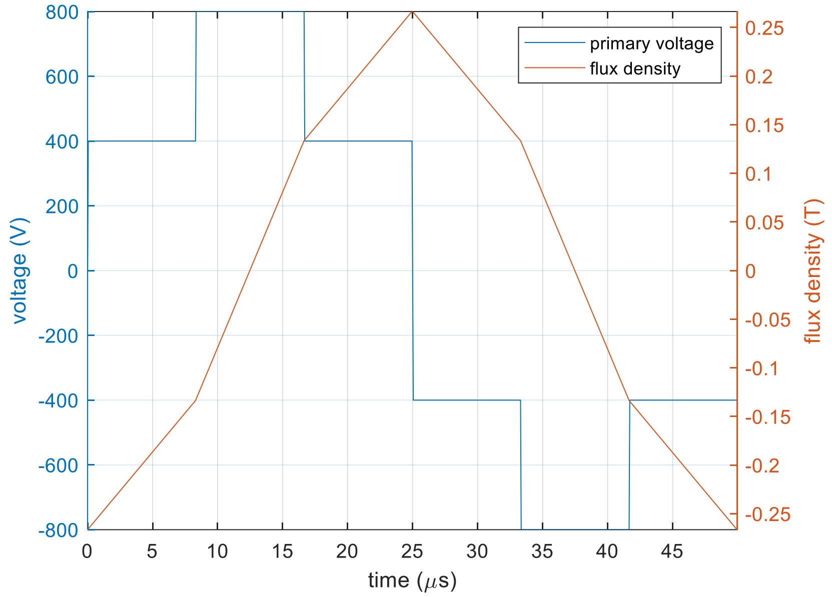

Fig. 4.9. Idealised voltage and flux density waveforms of the DAB3

Knowing the voltage waveform and the maximum flux density the core power loss can be calculated with (4.9). The core power loss is 255 W at 120°C.

Moreover, a sensibility analysis is performed for a sinusoidal voltage according to (4.7) as it is simpler to implement and as it gives comparable results to (4.9). Analysing Fig. 4.10 it can be observed that for a given thermal design, the ferrite 3C90 can be used in a wide frequency range but the maximum flux density must be decreased with the frequency increase. There is a minimum core loss at 95°C and the power loss doubles at low and very high temperature. The maximum core temperature should be kept below 100...120°C in order to avoid the thermal runaway. The Curie temperature of 3C90 is 220°C.

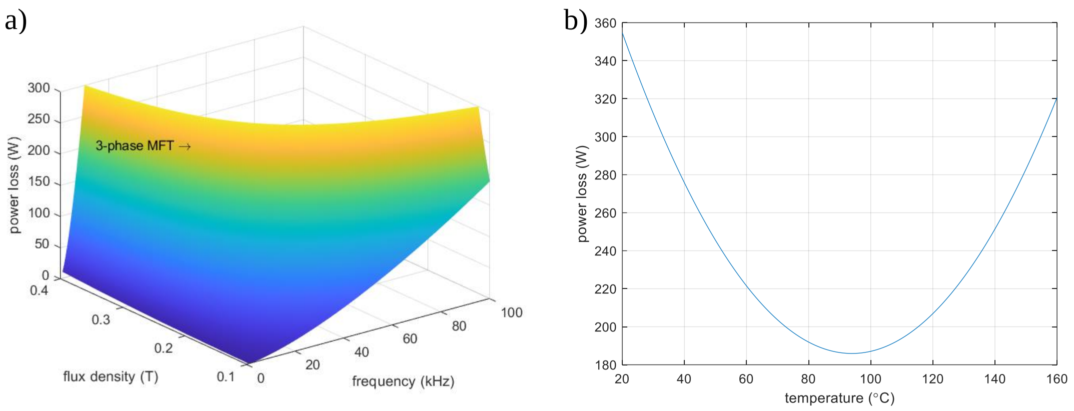

Fig. 4.10. Core loss sensibility analysis for sinusoidal voltage: a) at different frequency and flux density at 120°C, b) at different temperature at 20 kHz and 0.27 T

## 4.5. Thermal design

In order to calculate the MFT temperature, a 3D transformer model was developed in Ansys Icepak (which is based on the Ansys Fluent solver). The model presented in Fig. 4.11 was divided into four computational domains and the material properties were set as follows:

- $\Omega_1$ is the homogenized ferrite core with the thermal conductivity $\lambda = 4.25$ W/mK, specific heat $c = 750$ J/kgK, density $\rho = 4800$ kg/m$^3$ [49],
- $\Omega_2$ is the litz wire winding; in [93] a thermal model of a litz wire was proposed showing that the transverse thermal conductivity is below 1 W/mK; in the Icepak library, the material which has similar properties is epoxy resin with $\lambda = 0.2$ W/mK; hence, this homogenized material was used,
- $\Omega_3$ is the background region with the air temperature 40°C,
- $\Omega_4$ is the volume of fans with the same material properties as $\Omega_3$.

The emissivity coefficient of the core and winding was set to $\varepsilon = 0.8$. A turbulent air flow was considered.

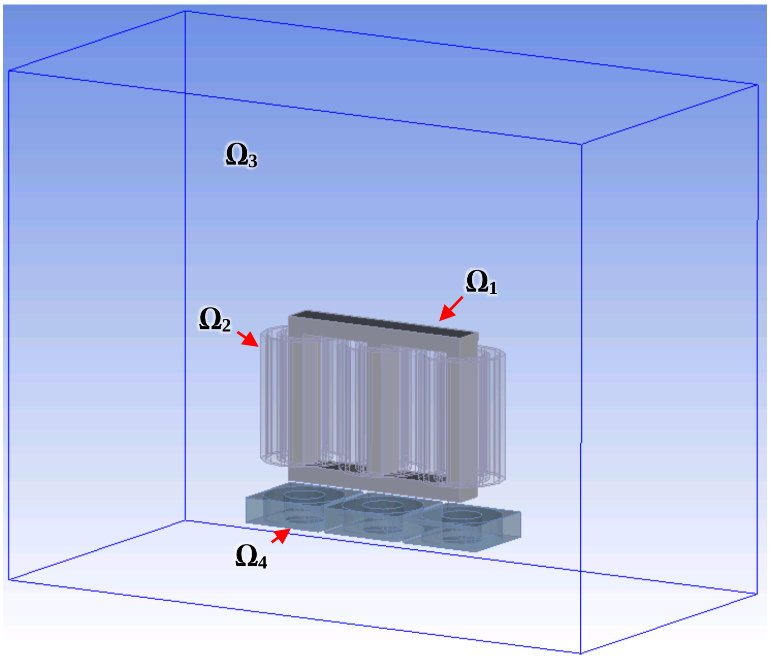

Fig. 4.11. 3D transformer model and simulation region for the CFD simulation including the domains: $\Omega_1$ core, $\Omega_2$ winding, $\Omega_3$ background and $\Omega_4$ fans

The model was discretised as presented in Fig. 4.12. The mesh is composed of 2.5 million elements. Icepak meshing procedure uses tetrahedral, hexahedral, polyhedral, pyramid, or wedge cell elements.

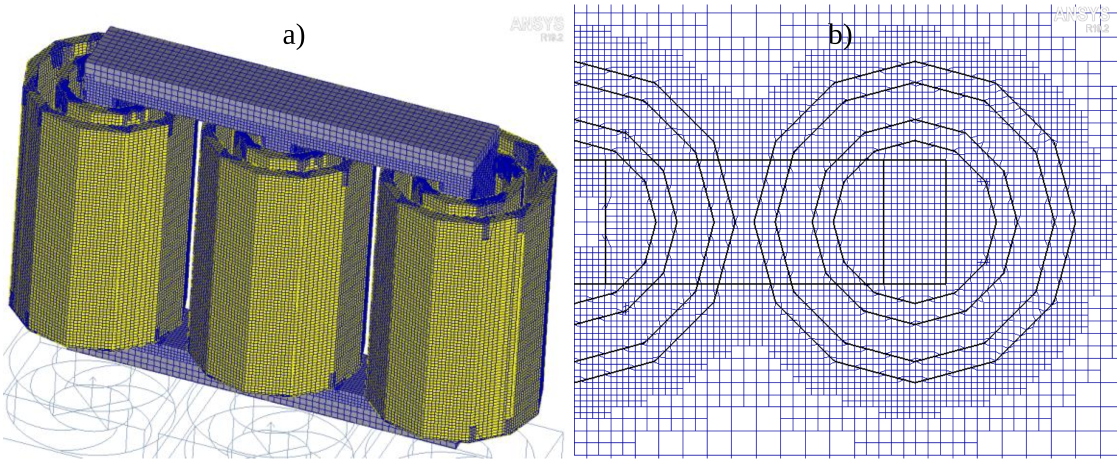

Fig. 4.12. Mesh for CFD simulation: a) plot on core and windings, b) plot on plane passing horizontally across the middle of the column

Three fans EBM papst 5214 NHH [43] were implemented with the linearized pressure-flow curve as presented in Fig. 4.13.

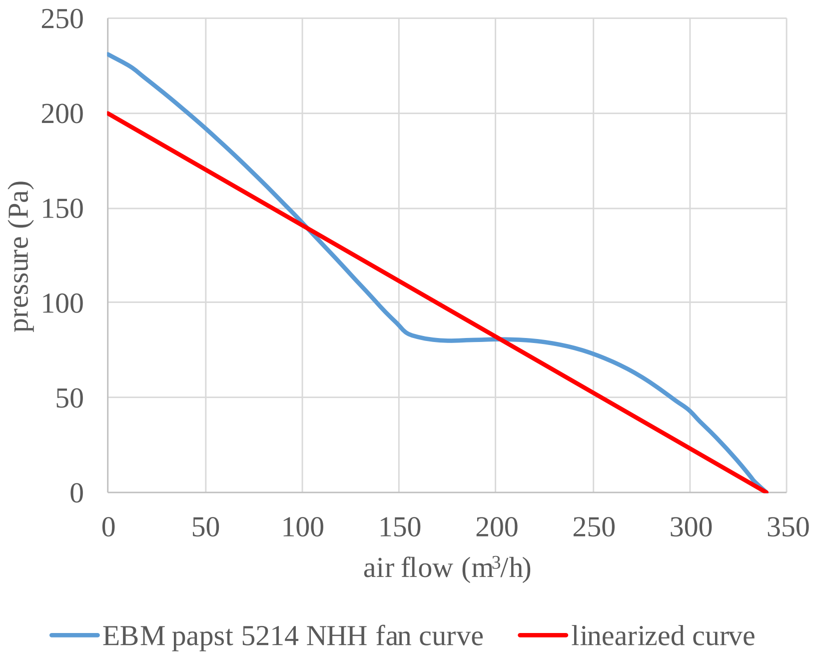

Fig. 4.13. EBM papst 5214 NHH fan curve [43] (blue) and linearized curve for CFD simulation (red)

The heat source was assigned according to the power loss presented in §4.3 and §4.4 corresponding to the degraded mode. The simulation result is presented in Fig. 4.14 showing the temperature distribution on a front view plane passing vertically across the middle of transformer. The core hotspot temperature is 122°C which is at the design limit and the average temperature is 93°C. The winding hotspot temperature is 90°C whereas its average temperature is 57°C giving a comfortable design margin. In Fig. 4.15 the air velocity vectors are displayed on a side view plane passing vertically across the middle of transformer. It is observed that the windings are well cooled thanks to the air passing between the windings. The core is not cooled well.

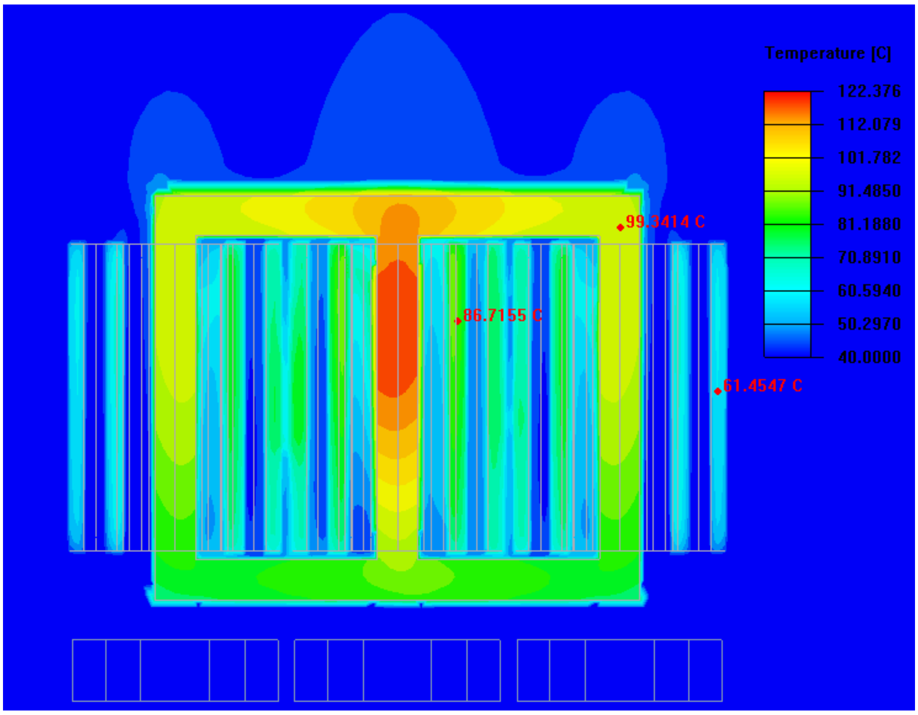

Fig. 4.14. Thermal simulation result in steady state showing the temperature distribution on a plane passing vertically across the middle of transformer, front view

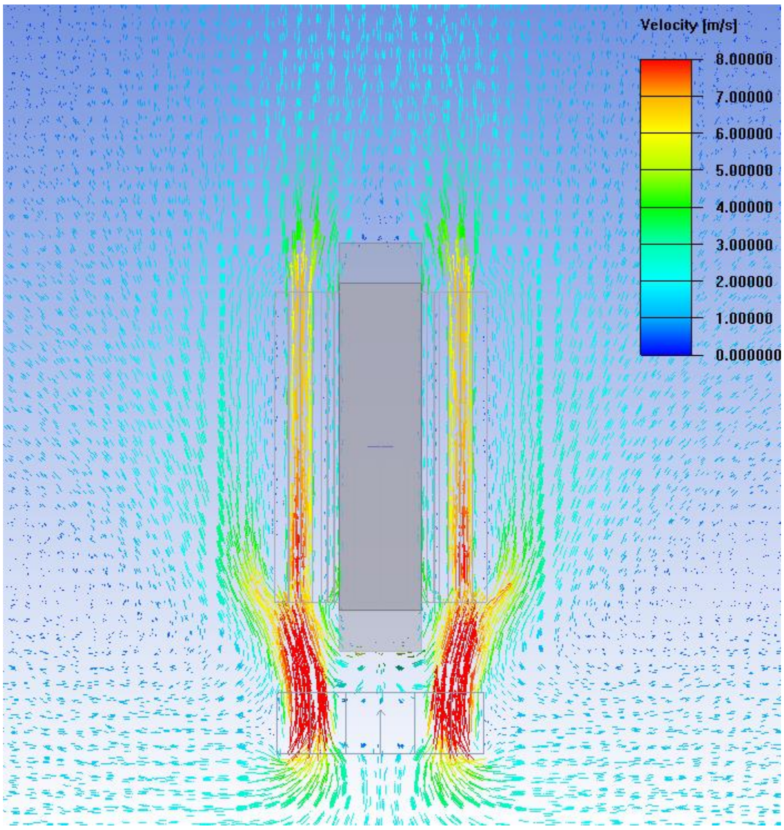

Fig. 4.15. Thermal simulation result in steady state showing the air velocity vectors on a plane passing vertically across the middle of transformer, side view

## 4.6. Mechanical assembly and prototyping

The detailed mechanical design was performed with a specialised industrial partner (Exxelia, France). The detailed 3D drawing of the 3-phase MFT prototype T2 is presented in Fig. 4.16.

According to this detailed 3D geometry a new CFD simulation was performed. The results were similar to the ones presented in §4.5 confirming the validity of the design. However, the simulation model was much more complex resulting in high number of finite elements and much longer simulation. The author concludes that the CFD simulation with simplified model is sufficient in the MFT thermal design.

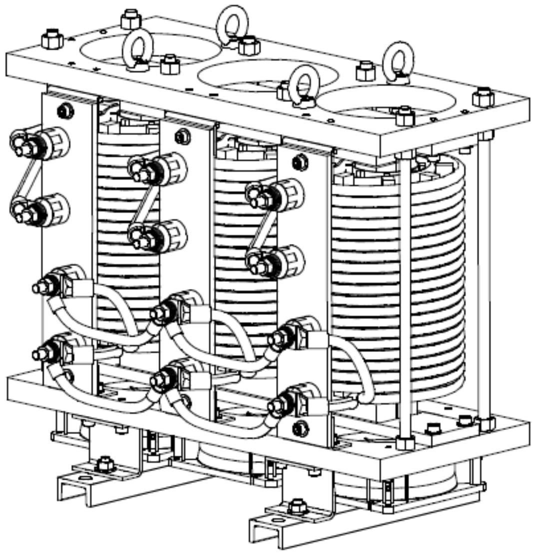

Fig. 4.16. 3D drawing of the 3-phase MFT prototype T2 by Exxelia

The manufacturing resulted in two prototypes T1 and T2 presented in Fig. 4.17.

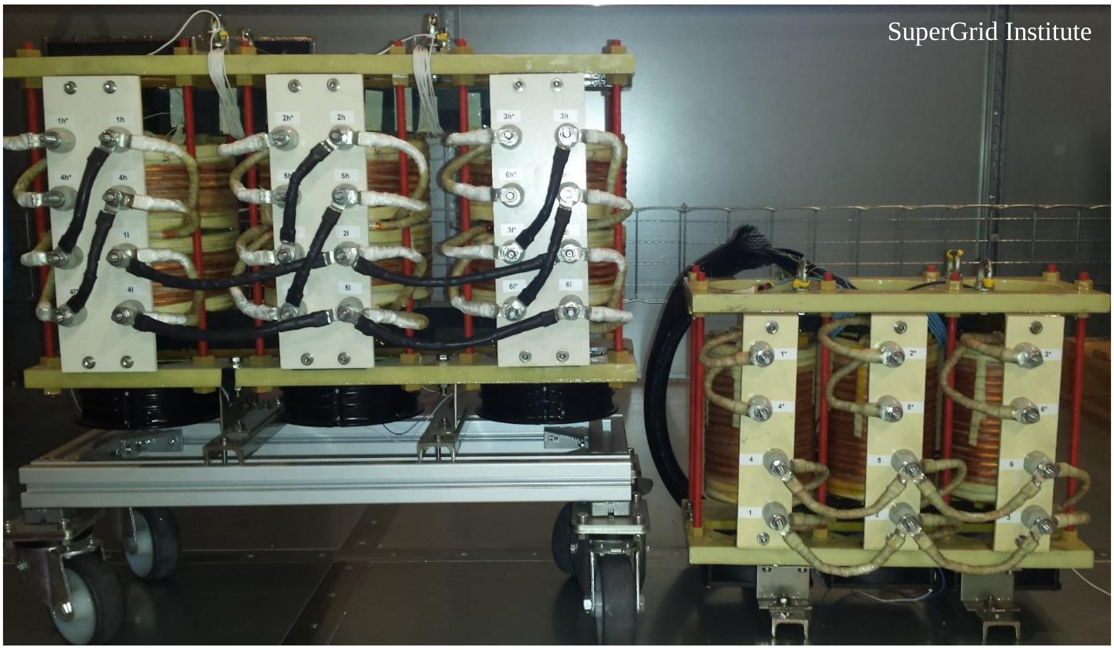

Fig. 4.17. 3-phase MFT prototype T1 (left) and T2 (right)

The weight of the 3-phase MFT T2 is 36 kg. This results in the transformer power density of 4 kVA/kg at $S_n$ according to (4.2). A comparable 50 Hz transformer, at 400 V and natural air cooling, has the power density of less than 0.4 kVA/kg [3]. The 3-phase MFT T2 at 20 kHz is more than 10 times lighter than the 3-phase 50 Hz transformer.

The 3-phase MFT T2 has roughly the same power density as the single-phase MFT (Appendix 2).

# 5. Model parameters

## 5.1. Introduction

The model developed in chapter 3 requires the parameters defined in the equivalent circuit Fig. 3.2.

The calculation of winding resistances is presented in §4.3. In this chapter the calculated values are compared against the measurement on the MFT prototype. The model resistance values $R_1$, $R_2$, ..., $R_6$ are defined.

The MFT model requires the magnetizing flux multi-dimensional characteristic $\mathbf{\Phi_m}(\mathbf{\Theta_g})$ and the corresponding derivatives $\partial\mathbf{\Phi_m}/\partial\mathbf{\Theta_g}$ as well as the leakage inductance matrix according to (3.22). In [36], these parameters were calculated based on a large number of measurements on the existing low power transformer. This approach can be challenging when applied to high power transformers. That is why in this dissertation an alternative approach is proposed. It is based on a single measurement of an equivalent $B(H)$ and a simplified FEM simulation model using homogenized winding and core materials.

The model parameters of the feedback Preisach model of hysteresis are calculated based on the equivalent $B(H)$ measurement on the MFT prototype. The hysteresis model is ready to be integrated in the equivalent circuit simulation according to Appendix 3 and allowing a good estimation of hysteresis power loss. However, the equivalent circuit model presented in Fig. 3.2 uses a simplified approach based on the equivalent circuit for core power loss. The resistances $R_7$, $R_8$ and $R_9$ are calculated in this chapter.

The proposed MFT model does not take into account the parasitic winding capacitances even if they can be easily integrated into the model (see Appendix 2). In this chapter the calculation of capacitances based on a FEM simulation is presented and compared against a measurement on the MFT prototype. The potential low impact of the parasitic winding capacitance is discussed.

Finally, a basic VSC model is presented.

## 5.2. Resistances

In this section the resistance values calculated in §4.3 are compared against the measurement. The resistance was measured using the impedance analyser Wayne Kerr 6500B (Fig. 5.1, [183]) according to the circuit presented in Fig. 5.2. The measurement of transformer AC resistance must be performed on the primary winding with the corresponding secondary in short circuit in order to achieve the equilibrium of magnetomotive forces. The measured value is equal to the primary plus secondary resistance.

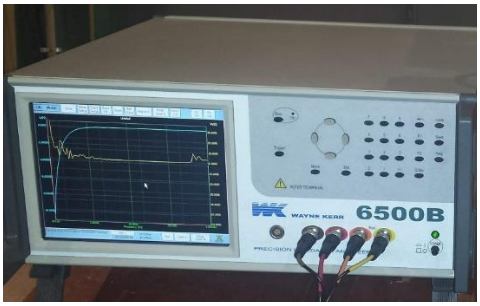

Fig. 5.1. Precision impedance analyser Wayne Kerr 6500B

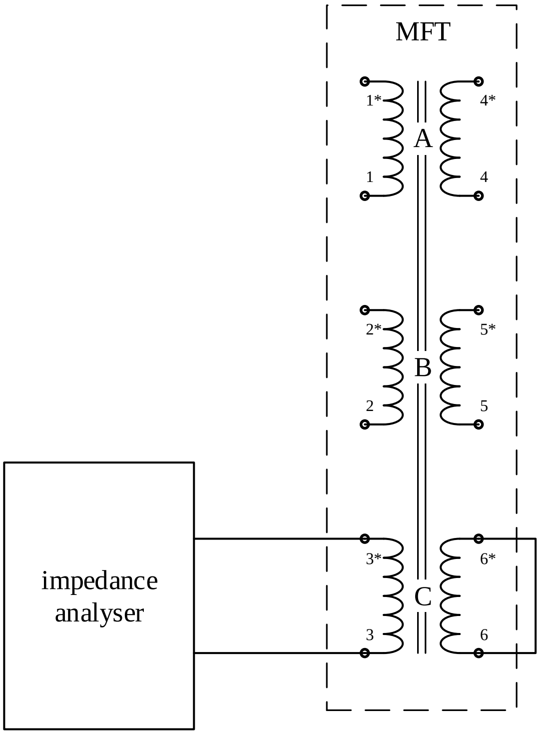

Fig. 5.2. Winding resistance and leakage inductance measurement circuit for column C

The measurement was performed at the ambient temperature of 20°C. The comparison between the calculated and measured resistance in function of frequency is presented in Fig. 5.3. It shows quite a good fit over the entire frequency range. The difference can be explained by some inaccuracies in winding dimensions, simplifying assumptions in analytical resistance calculation method and accuracy of the measurement method.

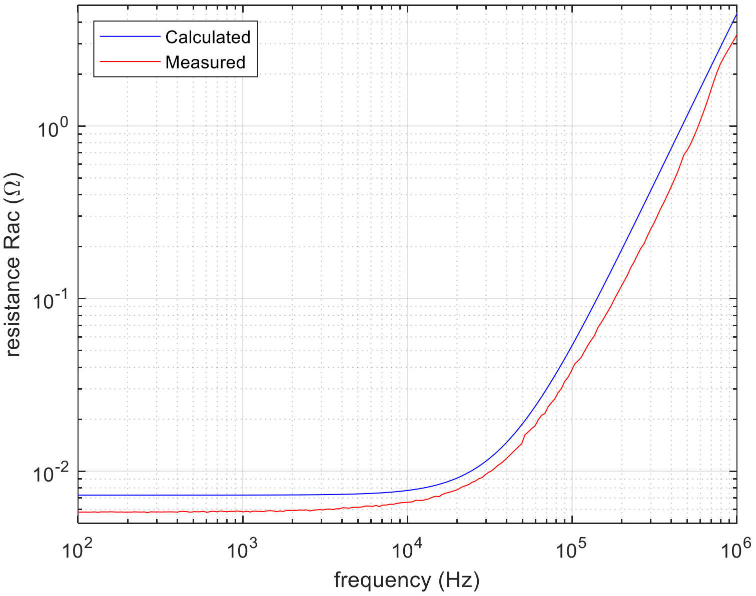

Fig. 5.3. Comparison of calculated and measured winding resistance

Since the validity of the analytical calculation has been proven then the individual primary and secondary winding resistances are calculated according to the §4.3.

Moreover, the connection wire resistance, between the VSC and the transformer terminals, and the VSC power semiconductor switch on-state resistance and switching losses have to be taken into account. According to [190], the MOSFET on-state resistance varies from 8 mΩ at 25°C and 16 mΩ at 150°C. The model resistance values are calculated as a sum of the above-mentioned components. The values are presented in Table 5.1, according to Fig. 3.2.

Table 5.1. Resistances of the equivalent circuit model of 3-phase DAB (mΩ)

| parameter | value |
|---|---|
| $R_1=R_2=R_3$ | 20 |
| $R_4=R_5=R_6$ | 24 |

## 5.3. Magnetic flux characteristic **Φ(Θ)**

### 5.3.1. Review of magnetic flux characteristic measurement methods

The nonlinear magnetic properties of core material are represented by the magnetic permeability which relates the magnetic induction $B$ with magnetic field strength $H$. Technical conditions for performing measurements of the hysteresis cycle are defined in international standards [205] and more specific in IEC 60404-2 for measurements with the Epstein apparatus [206] and IEC 60404-3 for measurements with the single sheet tester [207]. Specific requirements for measuring the magnetic properties of electrical steel strips and sheets at medium frequencies are defined in IEC 60404-10 [208]. Measurement of the magnetizing characteristics of cores made of soft ferrite materials should take into account the operating frequency range [170], [209] and temperature dependence of parameters [86], [109].

The measurement conditions defined in the standards differ from the conditions in which the core is placed during the operation of the transformer. Technological processes also have an impact on the magnetic properties of the finished transformer core [149]. The equivalent constitutive relation $B(H)$ of a multi air gap core structure is usually not known. However, the nonlinear magnetic properties of a transformer core can be described by the current-dependent flux linkage characteristics $\Psi(i)$ using the experimental approach. From the flux linkage characteristics, the $B(H)$ curve can be determined under certain simplifying assumptions. The measurement of $\Psi(i)$ hysteretic characteristics for inherently asymmetric three-phase transformer with three columns was reported in [56]. In this approach, to determine $\Psi(i)$ characteristics for each winding, only two phases are excited in a special manner. A good quality $\Psi(i)$ characteristics can be obtained at periodical voltage excitation with DC control offset as proposed in [20], [203]. The methods for determining the nonlinear characteristics $\Psi(i)$ of electromagnetic devices at different waveforms of the supply voltages (stepwise changing, sinusoidal, periodical with offset) and current responses were presented in [166]. A relatively new approach using several evolutionary methods [44] (the Genetic Algorithm, Differential Evolution, Teaching-Learning Based Optimization and Artificial Bee Colony) was reported in [82]. These methods can be implemented to determine a smooth magnetization characteristic but in order to obtain the best result, the combination of different methods is recommended. In this work the method reported in [56] is used and it is detailed in the following section.

### 5.3.2. Equivalent $B(H)$ measurement setup

A dedicated static $B(H)$ measurement setup was developed as presented in Fig. 5.4. It is composed of a high current AC power supply, oscilloscope and probes. The primary and secondary windings of each phase were connected in series in order to achieve a high magnetomotive force (MMF). The windings of two columns were connected in anti-parallel so that their MMFs add. Two additional auxiliary coils (AUX1 and AUX2) were placed on the yoke allowing the measurement of the magnetic flux in the core (see the blue wire in Fig. 5.5) and minimizing the magnetic coupling in the air. The voltage of the remaining winding (so-called zero-coil) was measured in order to verify that the magnetic flux coupled with this winding was close to zero.

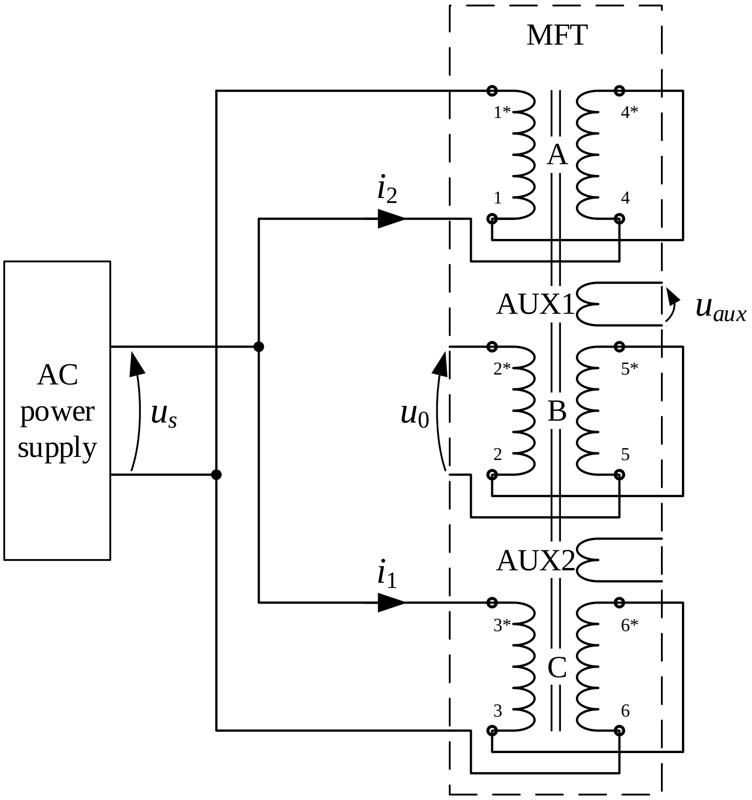

Fig. 5.4. Circuit diagram of the equivalent *B*(*H*) measurement setup where the windings C and A are supplied

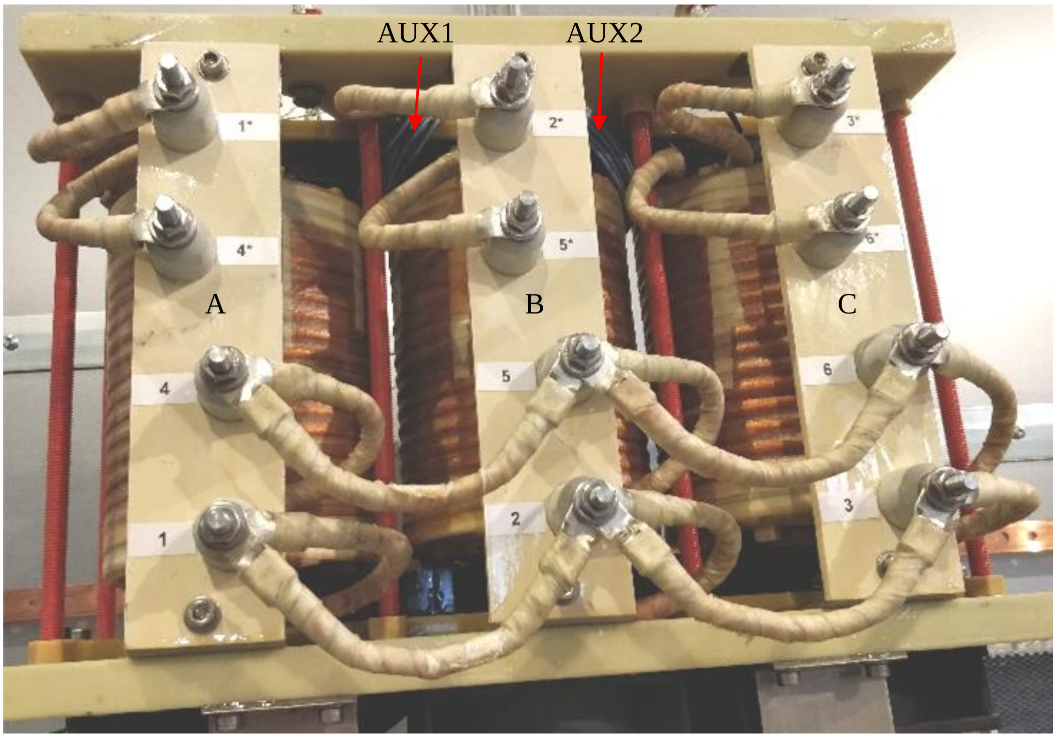

Fig. 5.5. Medium frequency transformer prototype T2 showing primary winding terminals: 1*-1, 2*-2, 3*-3, secondary winding terminals: 4*-4, 5*-5, 6*-6, three columns A, B, C, and additional auxiliary coils AUX1 and AUX2 for flux measurement (blue wire around the yoke)

Three measurements were performed according to the winding configurations presented in Table 5.2. The frequency of the power supply in the static $B(H)$ measurement setup was set to 100 Hz. This value was considered in order to minimize the effect of eddy currents (considering a high frequency material as ferrite) and to achieve a good performance of the available power supply.

The waveforms of the magnetic flux density $B(t)$ and the magnetic field strength $H(t)$ are calculated with:

$$H(t) = \frac{N_{exc}[i_1(t) + i_2(t)]}{l_m} \tag{5.1}$$

$$\Phi(t) = \int_0^T u_{aux}(t)\, dt \tag{5.2}$$

$$B(t) = \frac{\Phi(t)}{N_{aux} A_c} \tag{5.3}$$

where $i_1$ and $i_2$ is the current of the first and second excitation winding respectively, $N_{exc}$ is the number of turns of each excitation winding, $l_m$ is the average magnetic circuit length (visualized in Table 5.2), $u_{aux}$ is the voltage of the auxiliary coil placed on the yoke, $T$ is the period of the excitation voltage, $\Phi$ is the core magnetic flux, $N_{aux}$ is the number of turns of the auxiliary coil, $A_c$ is the average cross-section of the core.

Table 5.2. Winding configurations of the equivalent *B*(*H*) measurement circuits

| $u_s$ | $u_{aux}$ | $u_0$ | Magnetic flux path |
|---|---|---|---|
| A+B | AUX1 | C | 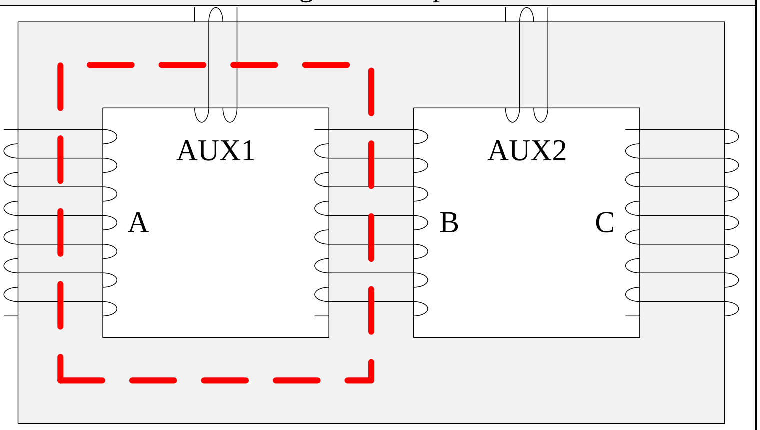 |
| B+C | AUX2 | A | 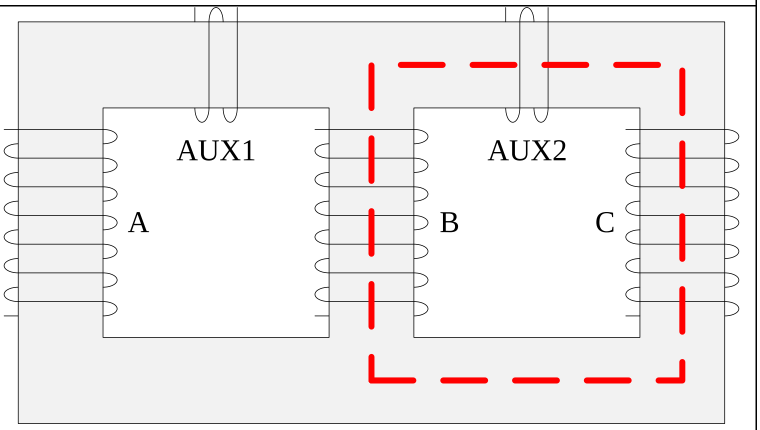 |
| C+A | AUX1<br>or<br>AUX2 | B | 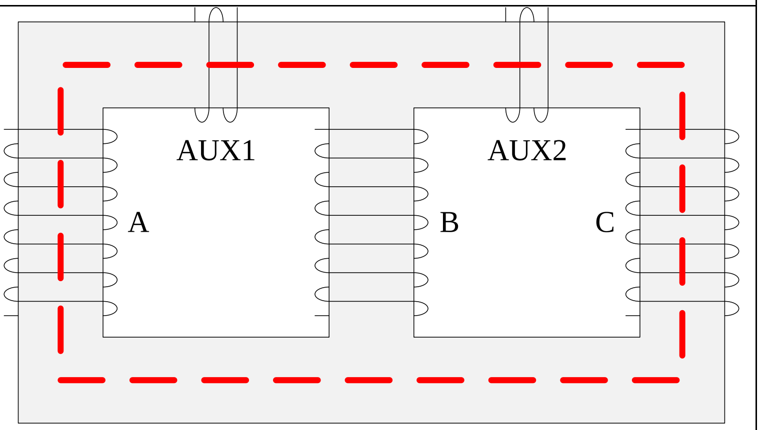 |

### 5.3.3. Equivalent *B*(*H*) measurement results

The measured waveforms for the example case where the C and A windings of T2 are supplied are presented in Fig. 5.6. The measurement was performed with the transformer temperature equal to ambient at 25°C. It can be observed that the supply voltage is close to sinusoidal. The currents in two excitation windings show the core saturation. The amplitude of the zero-coil voltage is relatively low.

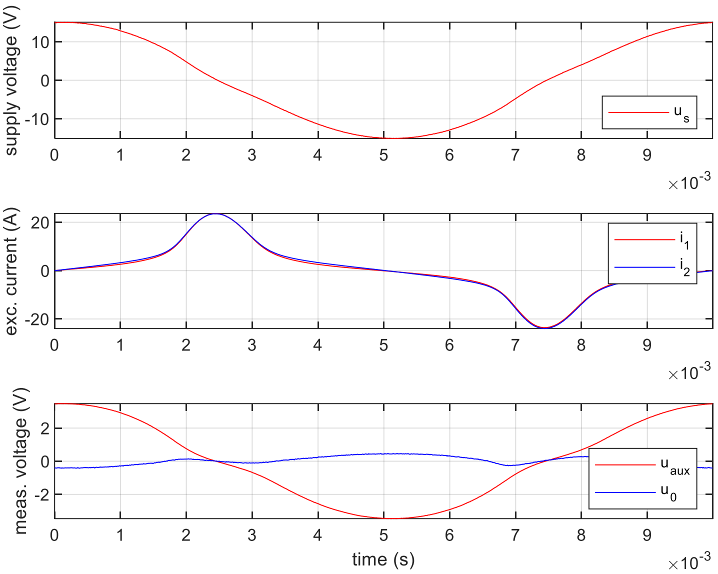

Fig. 5.6. Measured waveforms of the T2 supplied with C and A windings: supply voltage $u_s$, excitation currents $i_1$ (C) and $i_2$ (A), auxiliary coil voltage $u_{aux}$ (AUX1) and zero coil voltage $u_0$ (B)

Fig. 5.7 presents the waveforms of the magnetic flux calculated according to (5.2). The $\Phi_{aux}$ correspond to the main magnetic flux in two side columns and two yokes. The $\Phi_0$ corresponds to the magnetic flux in the central column. It is observed that the magnetic flux in the central column is below 5% of the main flux so it seems fair to neglect it.

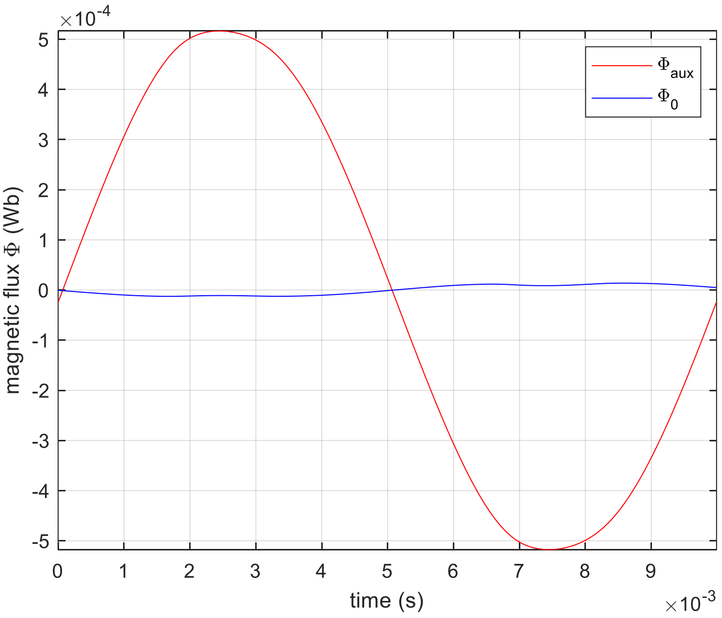

Fig. 5.7. Measured waveforms of the T2 supplied with C and A windings: magnetic flux of the auxiliary coil $\Phi_{aux}$ (AUX1) and magnetic flux of the zero coil $\Phi_0$ (B).

Thanks to (5.1) and (5.3) the magnetic field strength $H$ and the magnetic flux density $B$ are calculated. In Fig. 5.8, the resulting $B(H)$ is plotted for the positive values of $H$. The $B(H)$ is separated into the upward and downward curves which are then interpolated with piecewise linear functions in order to facilitate the data analysis. The anhysteretic $B(H)$ curve is calculated as the average of the interpolated upward and downward curves and further filtered to achieve a smooth curve adequate for further processing.

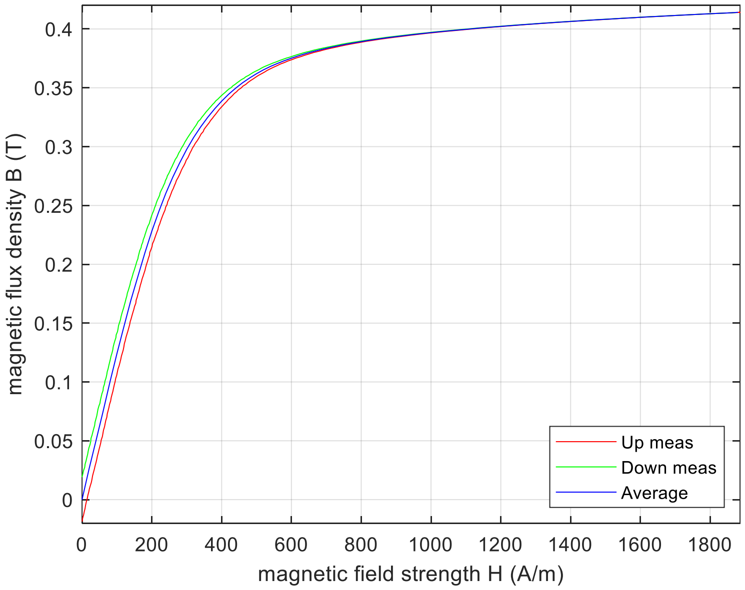

Fig. 5.8. Measured equivalent *B*(*H*) of the T2 supplied with C and A windings according to test circuit diagram from Fig. 5.4: upward curve (red), downward curve (green) and interpolated anhysteretic curve (blue)

### 5.3.4. Transformer finite element model

In the transformer core structure characterized by a construction periodicity (ferromagnetic material - air gap, ferromagnetic material - diamagnetic material, etc.) it is possible to utilize the homogenization technique or multiscale methods in the description of magnetic properties (reluctance of homogenized core, equivalent magnetic permeability, equivalent *B*(*H*), etc.). The use of the homogenization technique in FEM analysis of step-lap joints in steel sheet transformers was proposed in [131]. The homogenization technique was further developed in 2D FEM of steel sheet cores [67], [70], [141] and amorphous cores [138]. The multiscale methods were proposed in the analysis of magnetic properties of transformer cores in [71]. In order to increase the accuracy of magnetic computations, it was proposed the higher order FEM [68] and a step-wise method [111].

A 3D MFT model was developed in Ansys Maxwell. A simplified geometry was considered to achieve rapid simulation without accuracy decrease. Different 3D models of the winding were analysed and the cylinder winding was found offering the best performance/computation time ratio. The model was divided into three computational domains, as shown in Fig. 5.9. The domain $\mathbf{\Omega}_1$ is the volume of the windings, the domain $\mathbf{\Omega}_2$ is the volume of the core, and the domain $\mathbf{\Omega}_3$ consists of the air surrounding the MFT. The material properties have been considered isotropic and homogenized, so the Maxwell's equations can be simplified to:

$$\nabla \times \mathbf{H} = \begin{cases} \mathbf{j} & \text{in } \Omega_1 \\ \sigma\mathbf{E} & \text{in } \Omega_2 \\ 0 & \text{in } \Omega_3 \end{cases} \tag{5.4}$$

$$\nabla \times \mathbf{E} = -\frac{\partial \mathbf{B}}{\partial t}; \quad \nabla \bullet \mathbf{B} = 0; \quad \mathbf{B} = \nabla \times \mathbf{A} \tag{5.5}$$

where $\sigma$ = 0.25 S/m at 25˚C. The magnetic permeability $\mu$, which for nonlinear properties describes the relation between $dB$ and $dH$ in the constitutive equation [32], is calculated based on the equivalent anhysteretic $B(H)$ presented in Fig. 5.8.

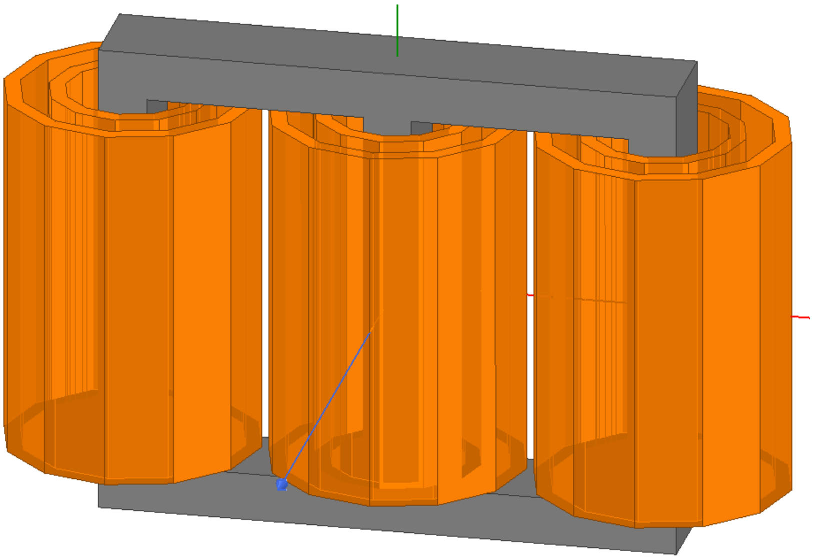

Fig. 5.9. 3D MFT model divided into three computational domains: $\Omega_1$ - volume of windings (orange), $\Omega_2$ - volume of homogenized core (grey), and $\Omega_3$ - air surrounding the MFT (white)

The core and winding were discretised as presented in Fig. 4.10. The mesh is composed of 267 thousand tetrahedral quadratic elements. In Maxwell the mesh is improved during the successive simulation iterations.

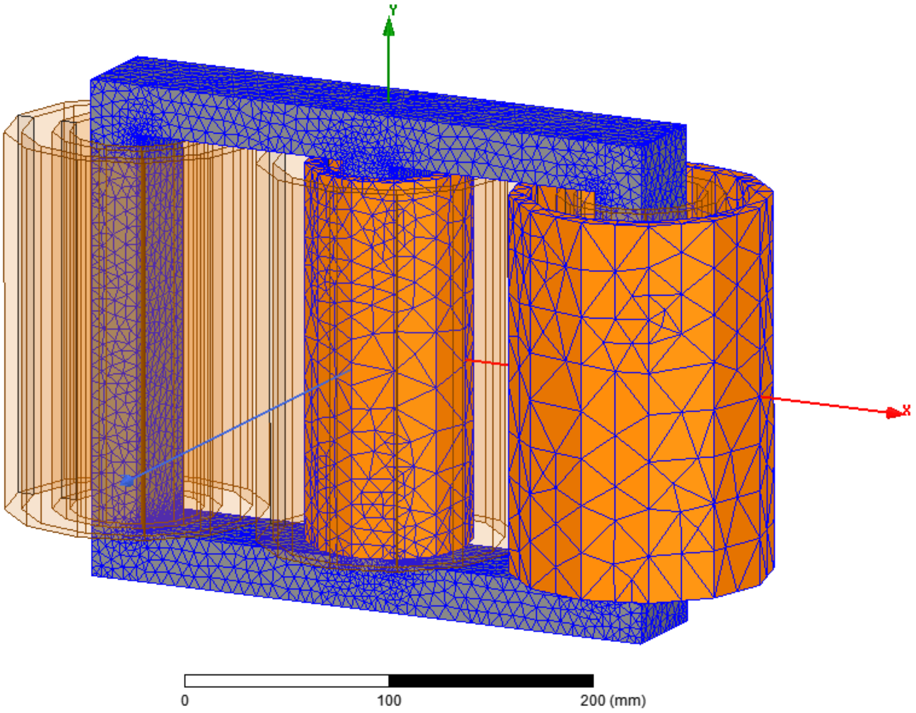

Fig. 5.10. Mesh for FEM simulation, plot on core surface and selected windings

### 5.3.5. FEM magnetostatic simulation

To calculate the $\mathbf{\Phi}(\mathbf{\Theta})$ multi-dimensional characteristic required for the circuit model, a series of magnetostatic simulations was performed with different MMFs. Considering the Yy vector group, the series of simulations can be reduced since the sum of primary MMFs is equal to zero and so of secondary. Practically, the author defines the primary and secondary MMFs as:

$$\mathbf{\Theta_p} = [\Theta_1 \quad \Theta_2 \quad \Theta_3] \tag{5.6}$$

$$\mathbf{\Theta_s} = [\Theta_4 \quad \Theta_5 \quad \Theta_6] \tag{5.7}$$

where $\Theta_1$, $\Theta_3$, $\Theta_4$ and $\Theta_6$ have discrete values in the range [-20e3, 20e3] A-turns, and

$$\Theta_2 = -\Theta_1 - \Theta_3 \tag{5.8}$$

$$\Theta_5 = -\Theta_4 - \Theta_6 \tag{5.9}$$

Fig. 5.11 presents a sample result of magnetostatic simulation. The magnitude of the flux density is plotted on the core surface corresponding to the MMF $\Theta_1$ = 200 A, $\Theta_2$ = -100 A, $\Theta_3$ = -100 A and $\Theta_4 = \Theta_5 = \Theta_6$ = 0 A.

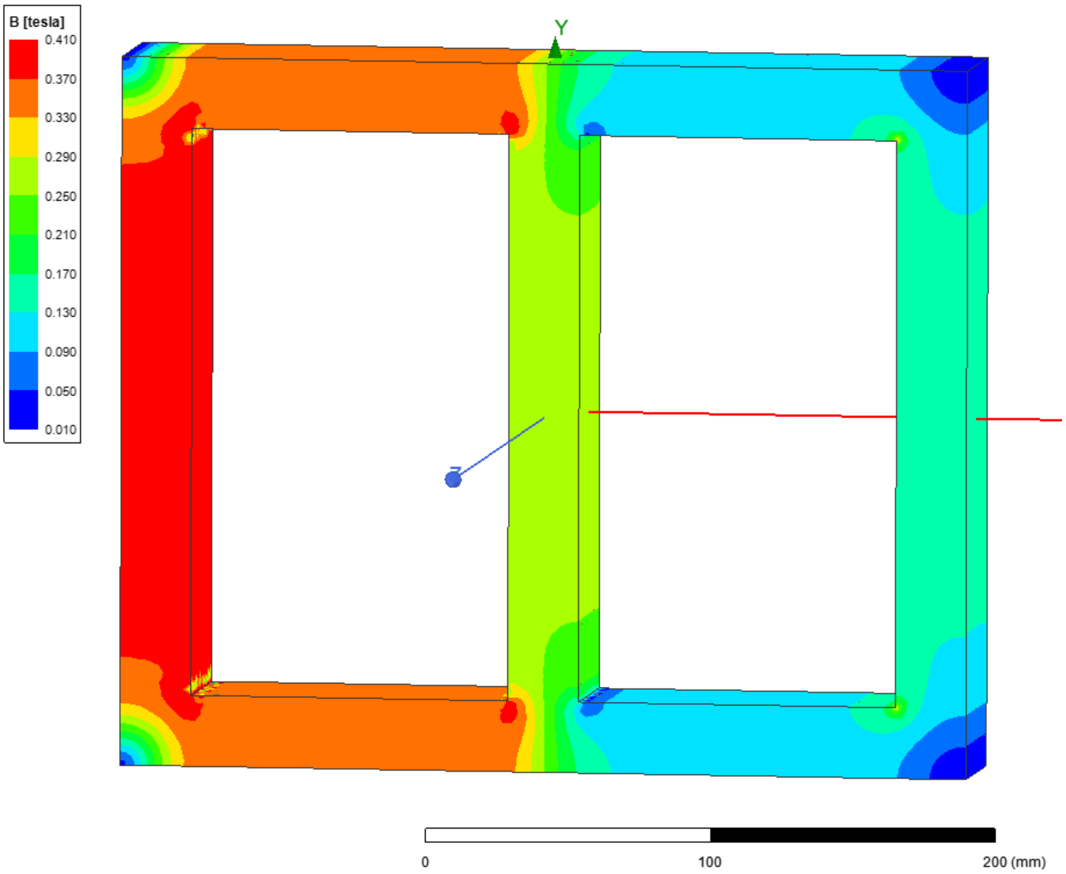

Fig. 5.11. Magnitude of magnetic flux density $B$ on core surface with the excitation $\Theta_1$ = 200 A, $\Theta_2$ = -100 A, $\Theta_3$ = -100 A and $\Theta_4 = \Theta_5 = \Theta_6$ = 0 A

### 5.3.6. Magnetizing flux $\mathbf{\Phi}_{\mathbf{m}}(\mathbf{\Theta})$

The transformer model presented in chapter 3 requires the $\mathbf{\Phi}(\mathbf{\Theta})$ to be split into magnetizing flux and leakage flux. The magnetizing flux is captured thanks to the magnetostatic simulation presented in §5.3.5. The magnetizing flux of side columns $\Phi_{m1}$ and $\Phi_{m3}$ is measured in the yoke in order to minimize the leakage flux contribution, in a similar manner to the measurement presented in §5.3.2. The magnetizing flux of the central column is calculated with:

$$\Phi_{m2} = -\Phi_{m1} - \Phi_{m3} \tag{5.10}$$

Fig. 5.12 presents the result of the series of magnetostatic simulations for column A and the corresponding surface interpolation. The magnetizing flux $\Phi_{m1}$ is presented as a function of the magnetizing MMF in generalized coordinates $\Theta_{g1}$ and $\Theta_{g2}$ according to (3.23). The effect of magnetic cross saturation can be observed as the shape of the curve $\Phi_{m1}(\Theta_{g1}, \Theta_{g2}=\text{const.})$ depends on the value of $\Theta_{g2}$. The maximum value of the magnetizing flux is 0.55 mWb, which corresponds to the magnetic flux density of 0.44 T.

Fig. 5.13 presents the result for column B. The magnetizing flux $\Phi_{m2}$ is presented as a function of the magnetizing MMF in generalized coordinates $\Theta_{g1}$ and $\Theta_{g2}$. Compared to $\Phi_{m1}$, the symmetry for $\Theta_{g1}$ and $\Theta_{g2}$ is observed.

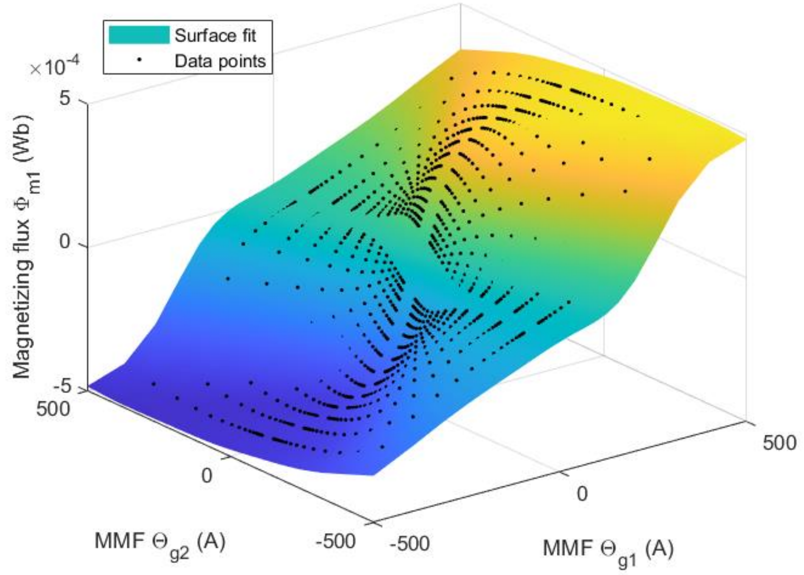

Fig. 5.12. Magnetizing flux $\Phi_{m1}$ as function of magnetizing MMF in generalized coordinates $\Theta_{g1}$ and $\Theta_{g2}$

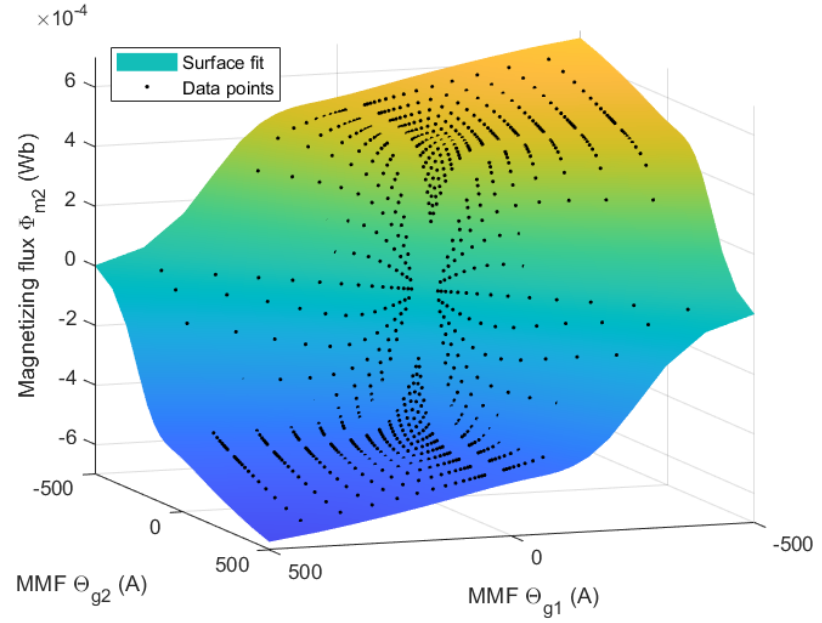

Fig. 5.13. Magnetizing flux $\Phi_{m2}$ as function of magnetizing MMF in generalized coordinates $\Theta_{g1}$ and $\Theta_{g2}$

Thanks to the magnetizing flux $\mathbf{\Phi_m}$ surface interpolation, the partial derivatives $\partial\mathbf{\Phi_m}/\partial\mathbf{\Theta_g}$ can be easily calculated. The partial derivatives for column A are presented in Fig. 5.14 for $\partial\Phi_{m1}/\partial\Theta_{g1}$ and Fig. 5.15 for $\partial\Phi_{m1}/\partial\Theta_{g2}$. The values of $\partial\Phi_{m1}/\partial\Theta_{g1}$ are always positive, with the maximum value of 4.6 µWb/A corresponding to the self-magnetizing inductance for generalized loop currents of 1.8 mH. The maximum value of $\partial\Phi_{m1}/\partial\Theta_{g2}$ is 1.5 µWb/A and it corresponds to the mutual magnetizing inductance for generalized loop currents of 0.6 mH. The partial derivative functions are directly used in the model presented in chapter 3 to calculate the values of the dynamic inductance matrix.

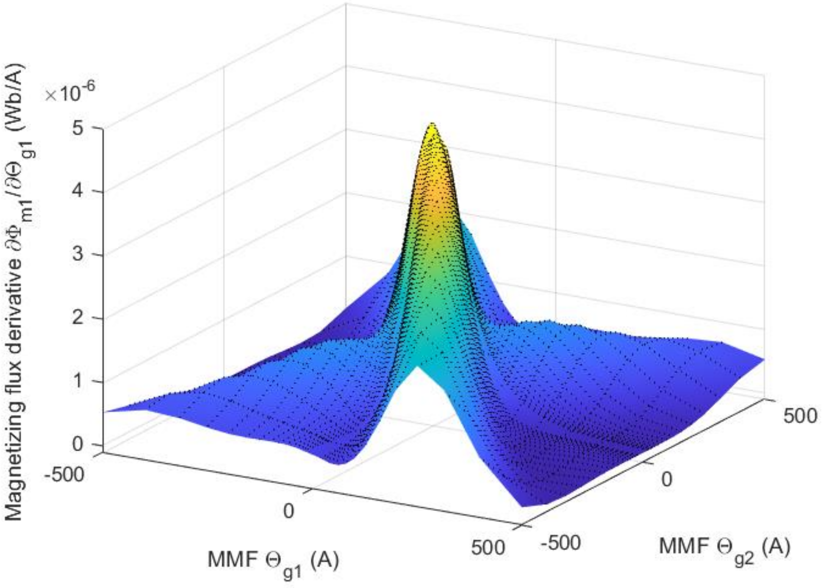

Fig. 5.14. Magnetizing flux partial derivative $\partial\Phi_{m1}/\partial\Theta_{g1}$ as function of magnetizing MMF in generalized coordinates $\Theta_{g1}$ and $\Theta_{g2}$

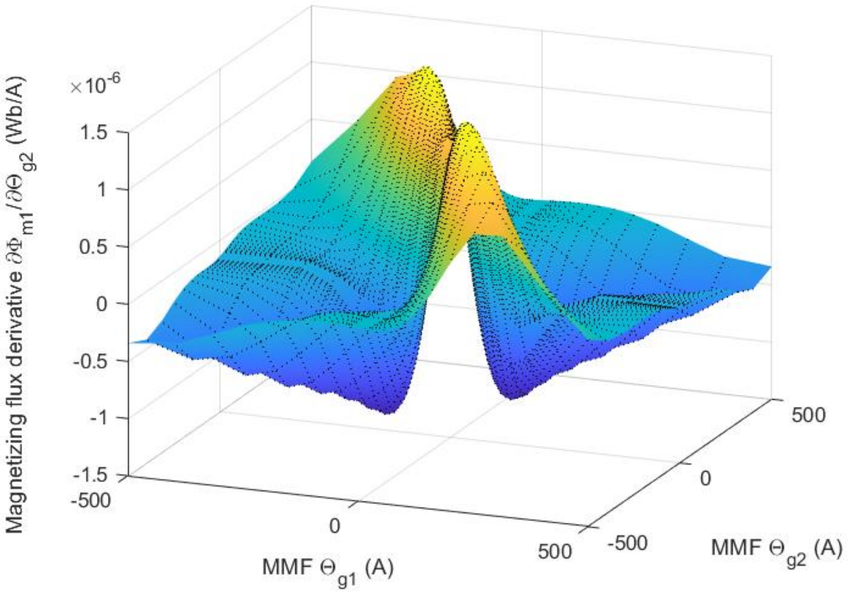

Fig. 5.15. Magnetic flux partial derivative $\partial\Phi_{m1}/\partial\Theta_{g2}$ as function of magnetizing MMF in generalized coordinates $\Theta_{g1}$ and $\Theta_{g2}$

### 5.3.7. Leakage flux $\mathbf{\Phi_{\sigma}(\Theta)}$

The leakage flux is calculated according to (3.7) where the flux linkage comes directly from the series of magnetostatic simulation. Fig. 5.16 presents the result for winding 1 and the corresponding surface interpolation. The leakage flux $\Phi_{\sigma 1}$ is presented as a function of MMF in generalized coordinates $\Theta_{g1}$ and $\Theta_{g2}$. It can be seen that the curve $\Phi_{\sigma 1}(\Theta_{g1}, \Theta_{g2}\text{=const.})$ is not linear and its shape depends on the value of $\Theta_{g2}$. However, for the further analysis the linearized $\Phi_{\sigma 1}(\Theta_{g1}, \Theta_{g2}\text{=const.})$ is assumed and independent from $\Theta_{g2}$.

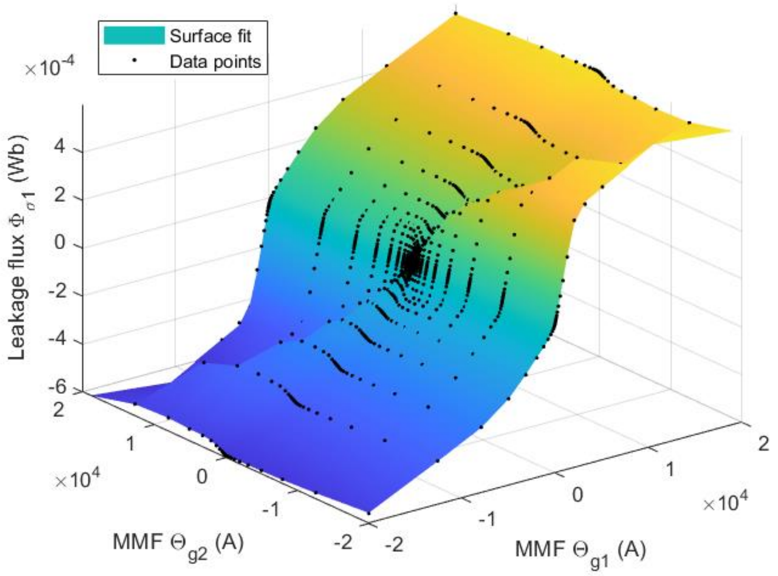

Fig. 5.16. Leakage flux $\Phi_{\sigma 1}$ as function of MMF in generalized coordinates $\Theta_{g1}$ and $\Theta_{g2}$

The leakage inductance matrix for generalized loop currents is calculated according to:

$$\mathbf{L_{\sigma g}} = \begin{bmatrix} N_p \frac{\partial \Phi_{\sigma 1}}{\partial \Theta_{g1}} N_p & N_p \frac{\partial \Phi_{\sigma 1}}{\partial \Theta_{g2}} N_p & N_p \frac{\partial \Phi_{\sigma 1}}{\partial \Theta_{g3}} N_s & N_p \frac{\partial \Phi_{\sigma 1}}{\partial \Theta_{g4}} N_s \\ N_p \frac{\partial \Phi_{\sigma 2}}{\partial \Theta_{g1}} N_p & N_p \frac{\partial \Phi_{\sigma 2}}{\partial \Theta_{g2}} N_p & N_p \frac{\partial \Phi_{\sigma 2}}{\partial \Theta_{g3}} N_s & N_p \frac{\partial \Phi_{\sigma 2}}{\partial \Theta_{g4}} N_s \\ \vdots & \vdots & \vdots & \vdots \\ N_s \frac{\partial \Phi_{\sigma 6}}{\partial \Theta_{g1}} N_p & N_s \frac{\partial \Phi_{\sigma 6}}{\partial \Theta_{g2}} N_p & N_s \frac{\partial \Phi_{\sigma 6}}{\partial \Theta_{g3}} N_s & N_s \frac{\partial \Phi_{\sigma 6}}{\partial \Theta_{g4}} N_s \end{bmatrix} \tag{5.11}$$

The leakage inductance matrix for phase currents is presented in Table 5.3. The leakage inductances for the central column (marked NA) are not calculated with the proposed method but they are not used in the model. Due to the linearization of the leakage flux, the leakage inductance matrix is symmetrical.

Table 5.3. Leakage inductance matrix (µH)

| $L_{\sigma k,n}$ | $n$=1 | $n$=2 | $n$=3 | $n$=4 | $n$=5 | $n$=6 |
|---|---|---|---|---|---|---|
| $k$=1 | 56.1 | NA | -2.9 | 48.2 | NA | -2.4 |
| $k$=2 | -9.4 | NA | -9.4 | 2.0 | NA | 2.0 |
| $k$=3 | -2.9 | NA | 56.1 | -2.5 | NA | 48.2 |
| $k$=4 | 48.2 | NA | -2.5 | 56.1 | NA | -2.1 |
| $k$=5 | -11.4 | NA | -11.4 | -15.5 | NA | -15.5 |
| $k$=6 | -2.4 | NA | 48.2 | -2.1 | NA | 56.1 |

The equivalent leakage inductance of the classical transformer model [83] for column A $L_{\sigma A}$ can be calculated with:

$$L_{\sigma A} = L_{\sigma 1,1} - L_{\sigma 1,4} + L_{\sigma 4,4} - L_{\sigma 4,1} \tag{5.12}$$

and it can be easily measured on the existing transformer. The value of $L_{\sigma C}$ is calculated accordingly. The value of $L_{\sigma B}$ is not calculated with the proposed method.

The equivalent leakage inductance of the classical transformer model was measured using the impedance analyser Wayne Kerr 6500B according to the circuit presented in Fig. 5.2. The comparison of the calculated and measured leakage inductances is presented in Table 5.4. A good fit is observed proving the validity of the proposed method for the calculation of the leakage flux $\mathbf{\Phi_\sigma(\Theta)}$.

Table 5.4. Equivalent leakage inductance of the classical transformer model (µH)

| | calculated | measured |
|---|---|---|
| $L_{\sigma A}$ | 15.8 | 16.0 |
| $L_{\sigma B}$ | NA | 15.8 |
| $L_{\sigma C}$ | 15.8 | 15.7 |

## 5.4. Hysteresis model parameters

The equivalent $B(H)$ measurement setup is presented in §5.3.2. A series of measurements was performed with MFT T2 and different excitation current amplitudes corresponding to the magnetic field strength amplitude from 35 A/m to 1900 A/m. It was found that above 800 A/m the width of the hysteresis loop does not change significantly. The selected measured hysteresis loops are presented in Fig. 5.17 for positive values of magnetic field strength. The coercive field $H_c$ and remanent flux density $B_r$ can be captured, which are 15 A/m and 20 mT respectively. These values are consistent with the material datasheet [51] which was realised according to IEC 62044 [210]. The datasheet $B(H)$ was measured on a ring core at 10 kHz.

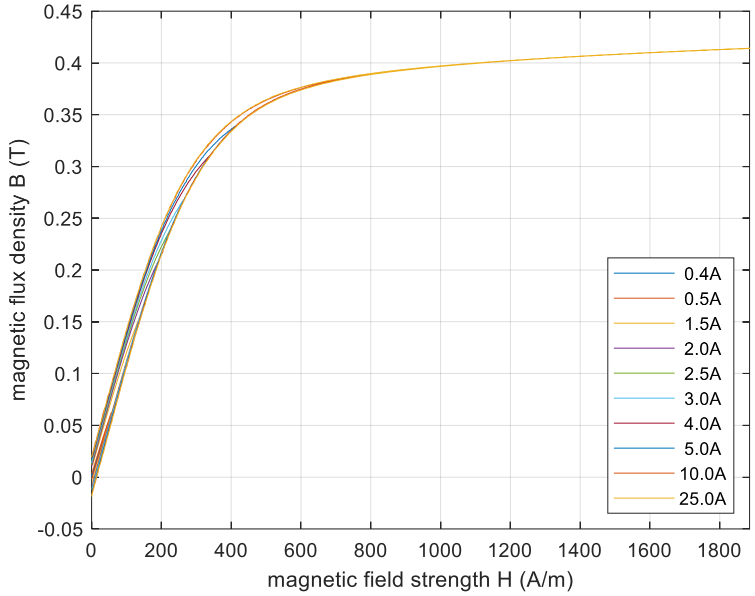

Fig. 5.17. Measured equivalent $B(H)$ of the T2 supplied with C and A windings according to test circuit diagram from Fig. 5.4 with different excitation current amplitudes

In order to calculate the hysteresis model parameters $A_n$, $S_{x,n}$, $S_{y,n}$, $K_1$ and $K_3$ the Levenberg-Marquardt optimization algorithm [126] was used. The model parameters were fitted for the upward and downward curves of the major hysteresis loop. The values of the hysteresis model parameters are presented in Table 5.5. It was found that 2 terms of the two-dimensional Gauss functional series are sufficient to model precisely the major hysteresis loop. The Preisach distribution function (PDF) $\mu(\alpha,\beta)$ is presented in Fig. 5.18 and the feedback function $H_f(B)$ is presented in Fig. 5.19.

Table 5.5. Feedback Preisach model parameters of MFT T2

| $A_1$ | $A_2$ | $S_{x,1}$ | $S_{x,2}$ | $S_{y,1}$ | $S_{y,2}$ | $K_1$ | $K_3$ |
|---|---|---|---|---|---|---|---|
| 0.31 | 1.35 | 1684 | 451 | 29.1 | 34.6 | 32.4 | -208 |

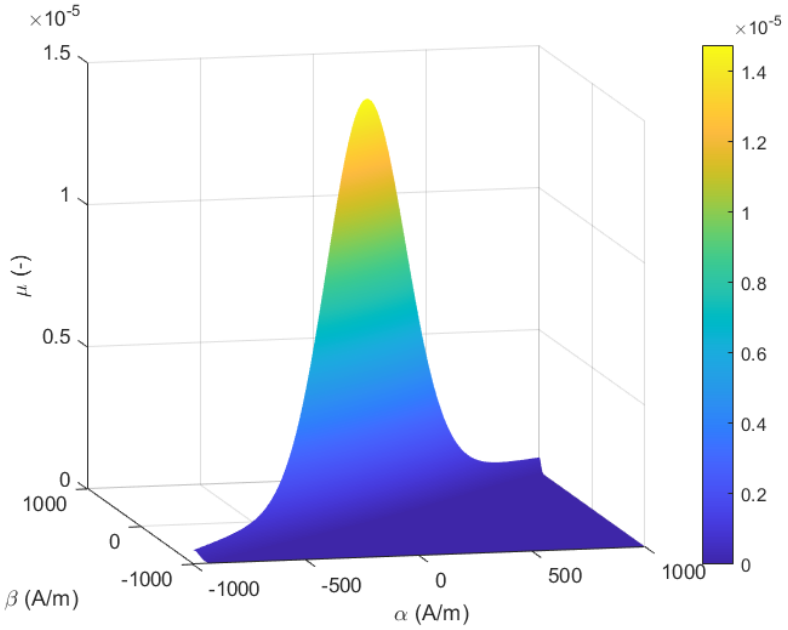

Fig. 5.18. Preisach distribution function $\mu(\alpha,\beta)$ of MFT T2

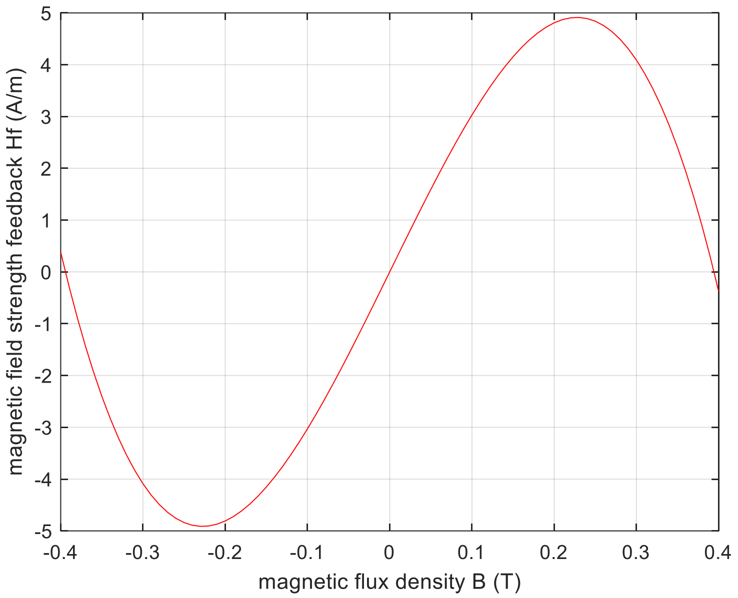

Fig. 5.19. Feedback function $H_f(B)$ of MFT T2

The feedback Preisach model of hysteresis was implemented with the above defined model parameters. The simulated major hysteresis loop is compared against the measurement in Fig. 5.20 showing a very good fit. The simulated minor hysteresis loop, corresponding to the MFT T2 nominal flux density is presented in Fig. 5.21. The width of the simulated hysteresis loop is slightly larger than the measurement but overall a good fit is observed.

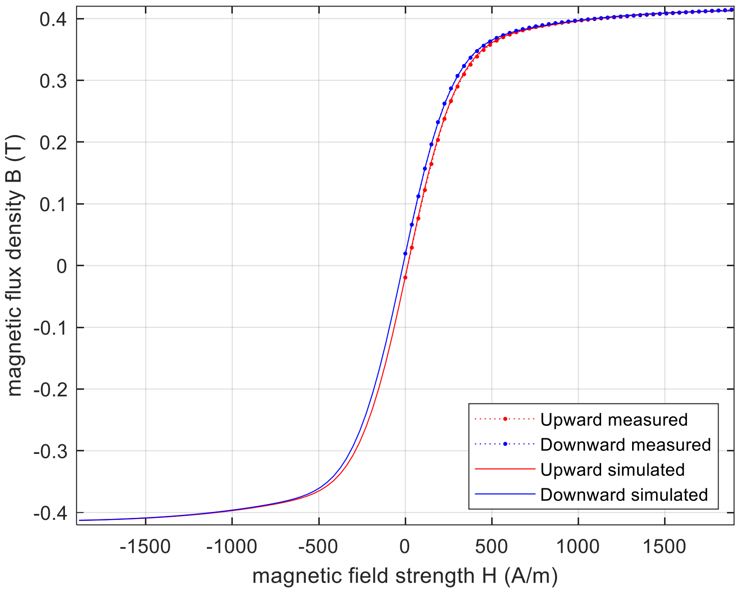

Fig. 5.20. Symmetrical major hysteresis loops: measured (dotted line) and simulated (solid line)

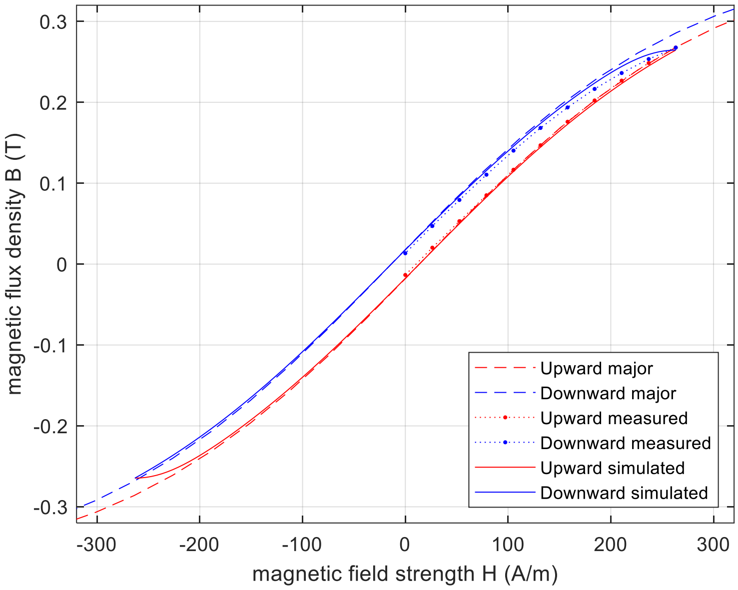

Fig. 5.21. Symmetrical minor hysteresis loops: measured (dotted line) and simulated (solid line); the major hysteresis loop (dashed line) is plotted for comparison

The hysteresis model is ready to be integrated in the equivalent circuit simulation allowing to evaluate the hysteresis power loss in transient and steady state simulations, and to represent precisely the magnetizing current waveforms.

This analysis has been submitted for publication in [121] and proves the thesis 1.

## 5.5. Equivalent circuit for core power loss

Assuming the number of turns for this equivalent circuit $N_e$=1, the resistance $R_7$=$R_8$=$R_9$=$R_{eh}$ is calculated with:

$$R_{eh} = 3\frac{\left(U_{ac1}\frac{N_e}{N_p}\right)^2}{P_{eh}} \tag{5.13}$$

where $U_{ac1}$ is defined in (2.3), $N_p$ is the number of primary turns and $P_{eh}$ is the core power loss calculated in §4.4. The value of $R_{eh}$ equals 5.3 Ω at 25°C.

## 5.6. Capacitances

The calculation of winding capacitance based on FEM electrostatic linear simulation was performed using the 3D model presented in §5.3.4. A constant voltage excitation of 1 V on primary windings and 0 V on secondary windings were set. The core was considered a floating charge. The electrostatic solver in Ansys Maxwell 3D allows to calculate automatically the complete transformer capacitance matrix [9]. Fig. 5.22 presents the self and mutual capacitances for winding 1. The capacitance matrix result is presented in Table 5.6. It can be observed that the capacitances are in the pico farad range.

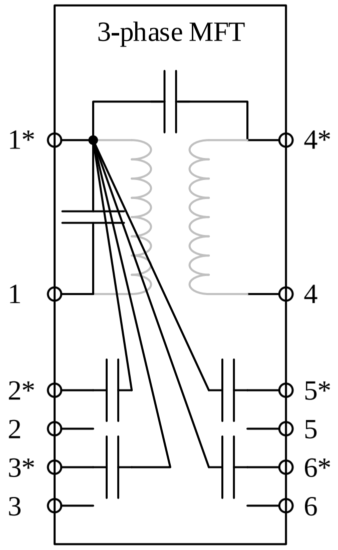

Fig. 5.22. 3-phase transformer capacitances of the winding 1

Table 5.6. Capacitance matrix simulation result (pF)

| | W1 | W2 | W3 | W4 | W5 | W6 |
|---|---|---|---|---|---|---|
| W1 | 64.7 | -10.8 | -10.0 | -38.3 | -3.4 | -2.3 |
| W2 | -10.8 | 65.2 | -10.8 | -2.5 | -38.6 | -2.5 |
| W3 | -10.0 | -10.8 | 64.7 | -2.3 | -3.4 | -38.3 |
| W4 | -38.3 | -2.5 | -2.3 | 57.5 | -12.9 | -1.6 |
| W5 | -3.4 | -38.6 | -3.4 | -12.9 | 71.0 | -12.9 |
| W6 | -2.3 | -2.5 | -38.3 | -1.6 | -12.9 | 57.5 |

The measurement of the transformer parasitic capacitance is difficult as the values are very low and there are multiple magnetic and capacitive couplings. In [108] a method for single-phase transformers was proposed but its application to the prototype 3-phase MFT did not give satisfactory results. Instead the measurement of mutual capacitances was performed using Wayne Kerr 6500B according to the circuit presented in Fig. 5.23. The estimation of self-capacitances was done based on the measurement of the first resonant frequency $f_r$ with:

$$C = \frac{1}{(2\pi f_r)^2 L_m} \tag{5.14}$$

where $L_m$ is the magnetizing inductance. An example measurement result for winding 1 is presented in Fig. 5.24 where the first resonance frequency is 560 kHz. The complete capacitance matrix measurement is presented in Table 5.7. Comparing the simulated (Table 5.6) and measured (Table 5.7) capacitances it can be observed that they are quite different but the order of magnitude is the same. The differences are due to the simplifications of the 3D model used in the FEM simulation. In particular, the geometry of the real winding is not a cylinder but a helix including the winding terminations and the insulation involves different materials (air, resin, insulation foil, etc.).

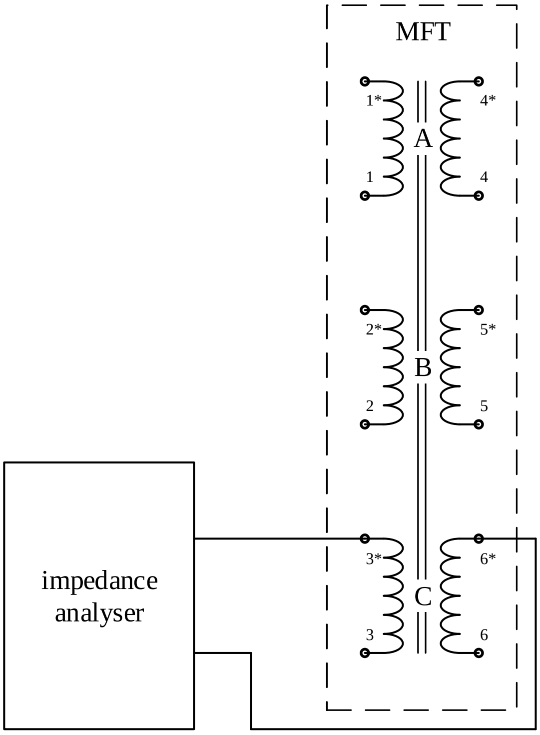

Fig. 5.23. Winding capacitance measurement circuit for column C

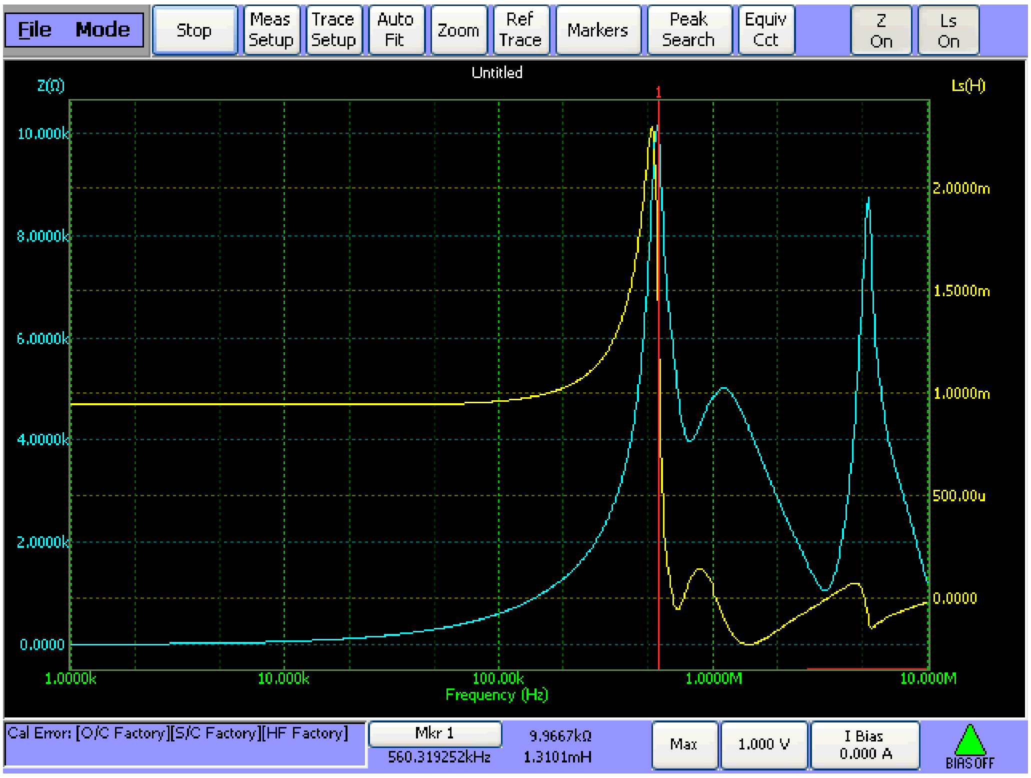

Cal Error: [O/C Factory][S/C Factory][HF Factory]

Mkr 1 560.319252kHz 9.9667kΩ 1.3101mH

1.000 V

I Bias 0.000 A

Fig. 5.24. Impedance of winding 1 showing the first resonant frequency at 560 kHz; the magnetizing inductance is approximately 0.9 mH at 20 kHz

Table 5.7. Capacitance matrix measurement (pF)

| | W1 | W2 | W3 | W4 | W5 | W6 |
|---|---|---|---|---|---|---|
| W1 | 92 | -30 | -21 | -80 | -31 | -19 |
| W2 | -31 | 61 | -29 | -28 | -86 | -26 |
| W3 | -21 | -29 | 82 | -19 | -29 | -78 |
| W4 | -79 | -28 | -19 | 92 | -29 | -17 |
| W5 | -31 | -86 | -29 | -29 | 61 | -28 |
| W6 | -19 | -26 | -78 | -17 | -28 | 82 |

The simulated and measured capacitance values are roughly in the range of tens of pico farad. Their influence is above 0.5 MHz where the resonance with the magnetizing inductance is observed and above 5 MHz where the resonance with the leakage inductance is observed (Fig. 5.24). They are not included in the circuit model due to their limited impact on the considered analysis. However, they are taken into account in an electromagnetic interference study reported in [60], [61] and involving the author's contributions.

## 5.7. Voltage source converter

Each VSC is modelled with three controlled ideal voltage sources. The voltage source signal is generated according to the rectangular modulation described in §2.3. The phase shift $\delta$ is calculated to achieve the required power flow according to (2.1). The voltage waveform slopes correspond to the average SiC inverter *dv*/*dt*.

# 6. Analysis and verifications

This chapter makes a benefit of the model developed in chapter 3 and the 3-phase MFT prototype designed in chapter 4. The chapter is divided into three independent sections dealing with:

- the experimental testing of the 3-phase MFT prototype proving the validity of the design,
- the analysis of the parasitic air gaps in ferrite core MFT what was revealed in this dissertation as a challenge in high power MFT,
- the model verification and the analysis of magnetic cross couplings and mutual leakage inductances which were possible thanks to the proposed MFT model.

## 6.1. Experimental testing

### 6.1.1. Introduction

A dedicated power test bench has been developed as a part of the DC-DC 100 kW project at SuperGrid Institute, France. It allows the experimental validation of the 3-phase DAB and the 3-phase MFT. The test bench layout is presented in Fig. 6.1 and it is composed of:

- power circuit - containing a controlled DC power supply, components and high voltage wiring presented in Fig. 6.2,
- controls - including a controller and low voltage wiring for VSCs, sensors and switchgear,
- cooling - realised with a set of fans for VSCs and transformer as well as an air conditioning unit,
- safety system - a Faraday cage containing the power circuit and controls coupled with a discharge, grounding and access interlock,
- acquisition system - a set of probes and a data acquisition device.

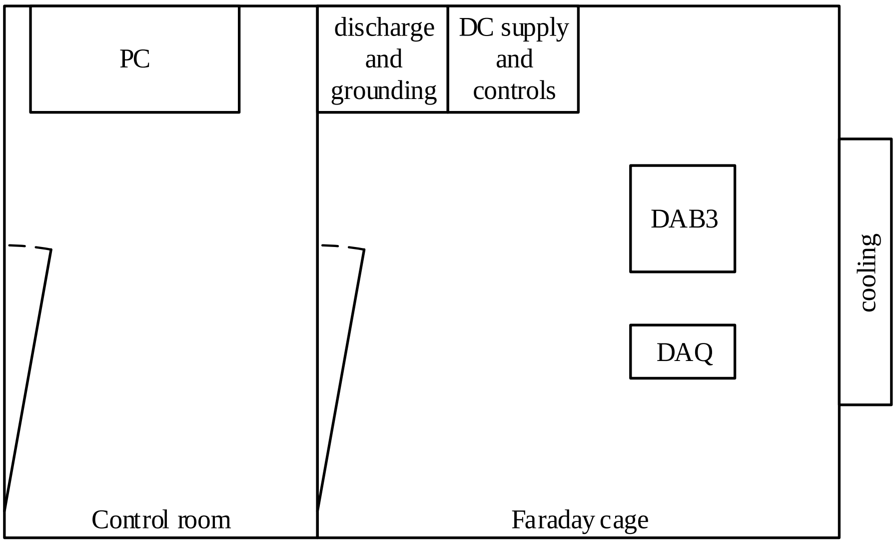

Fig. 6.1. DAB3 test bench layout

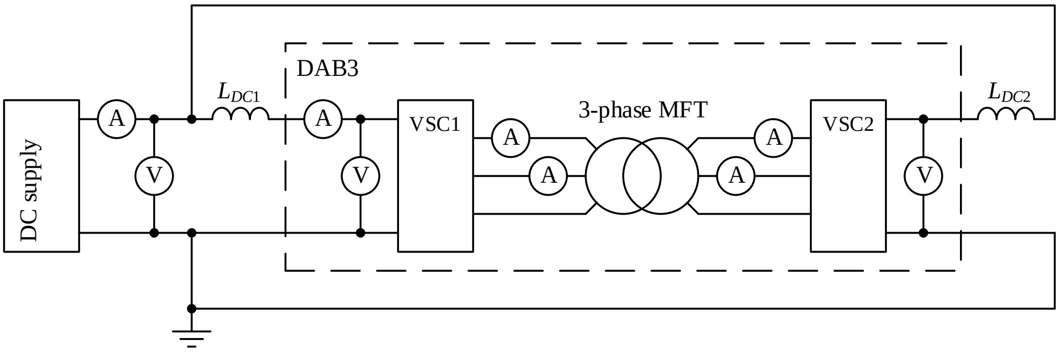

Fig. 6.2. DAB3 test bench power circuit diagram

The power circuit (Fig. 6.2) is arranged in back-to-back in order to test the DC-DC converter at full power with a minimum energy consumption. The converter output is connected to its input and the whole is supplied from the DC power supply which sets the voltage reference and supplies the test circuit power loss. If the DC-DC ratio is different from 1 then two DC-DC converters are required. The inductors $L_{DC}$ are used to decouple the VSCs.

The DC-DC converter operates in the power regulation mode. The controller uses the measurements provided by the DC voltage and DC current transducers. The current transducers in the AC link are necessary for the internal converter protection. They may be also used for the control of the transformer DC bias [182]. The control is implemented in Speedgoat real-time target [160] providing the firing orders for the VSC gate-drives (Fig. 6.3). The Speedgoat is interfaced with a PC through a fibre optic Ethernet network using the Matlab/Simulink real-time software [114].

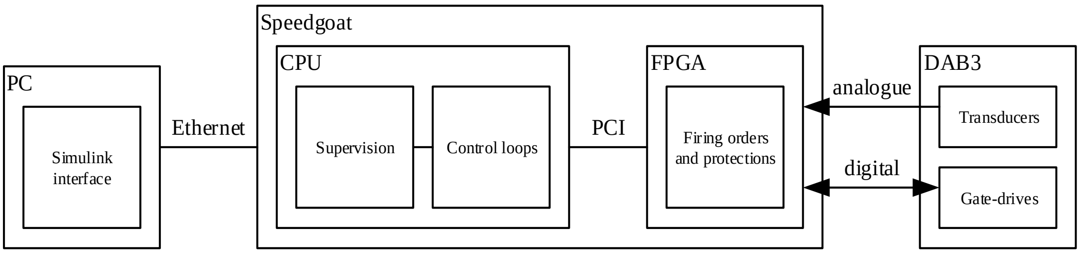

Fig. 6.3. DC-DC 100 kW test bench controls

The DC-DC 100 kW test bench implementation is presented in Fig. 6.4. A detailed view of the 3-phase DAB is presented in Fig. 6.5.

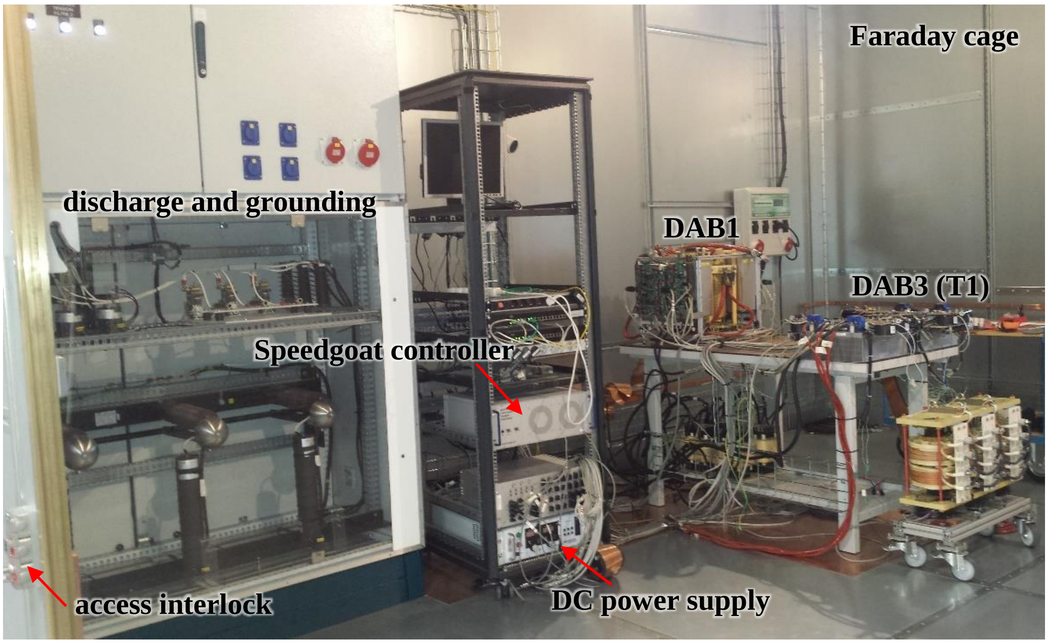

Fig. 6.4. DC-DC 100 kW test bench implementation with 3-phase MFT T1 at SuperGrid Institute

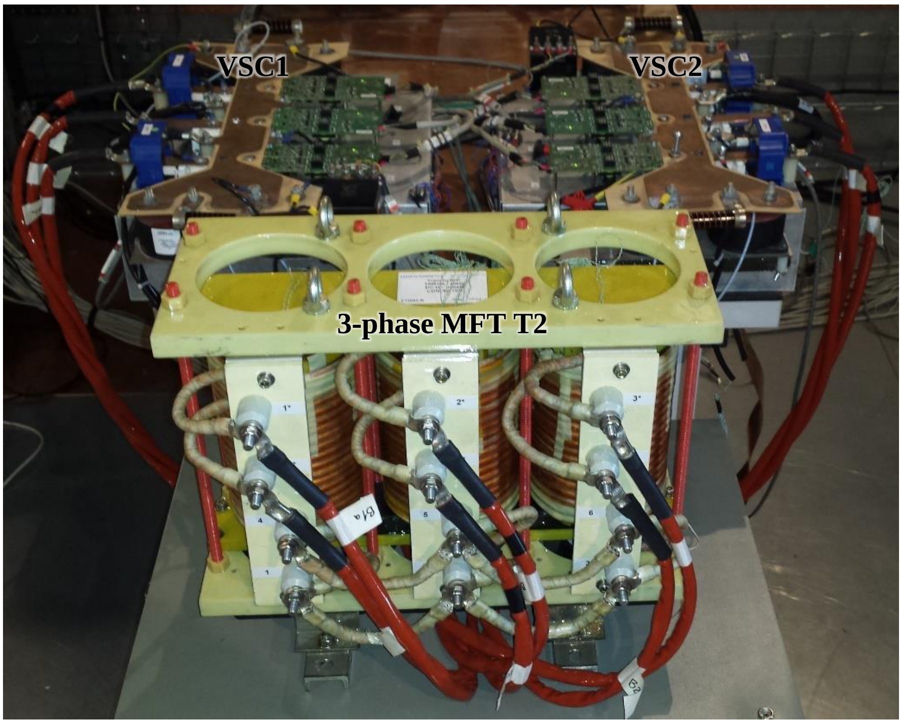

Fig. 6.5. 3-phase dual active bridge with MFT T2

A significant number of investigations and tests were performed with the DAB3 and the 3-phase MFT, including: power electronics, controls, EMI, magnetics, etc. Some of the results are published in [41], [60], [61], [96]. Two selected tests are presented in the following sections validating the 3-phase MFT prototype design presented in chapter 4.

### 6.1.2. MFT thermal test

The thermal test was performed using the 3-phase DAB operating at $U_{dc1} = U_{dc2} = 1200$ V and 100 kW corresponding to nominal operating mode. The purpose of this test was to validate the thermal design presented in §4.5. The test bench during the thermal test is presented in Fig.

6.6. The MFT temperature was measured with some thermocouples placed around the transformer during the manufacturing (Appendix 4). An additional measurement was done using a thermal camera.

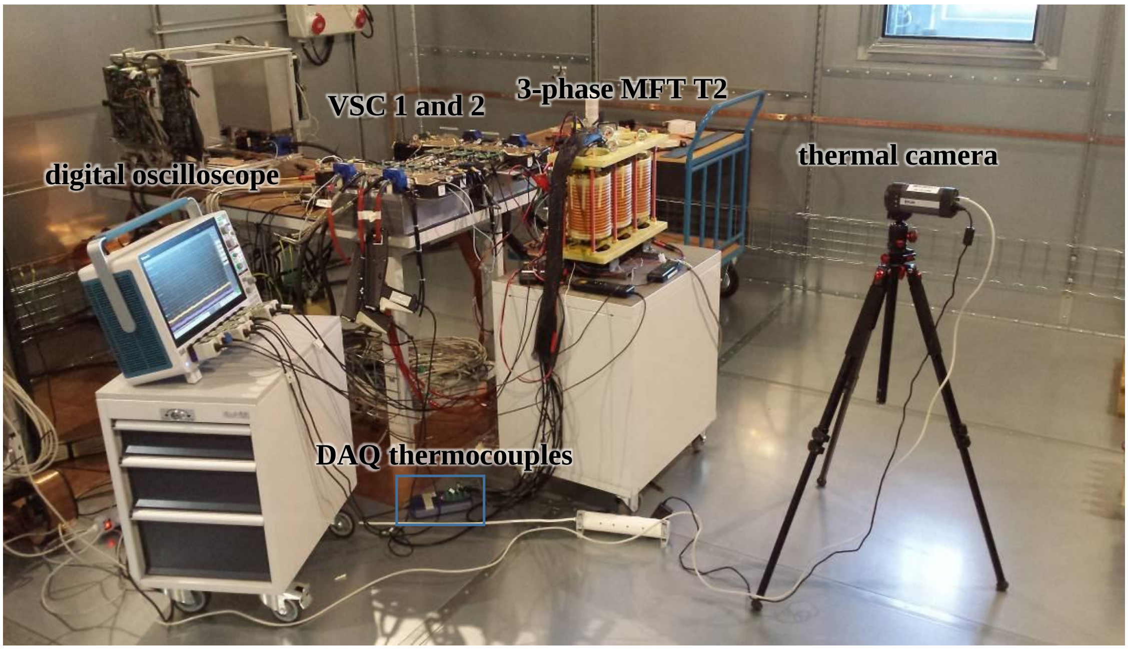

Fig. 6.6. Thermal test of the 3-phase MFT at SuperGrid Institute

In Fig. 6.7 the thermal test result is presented showing the values of temperature rise $\Delta T$. It lasted for 6 hours. Some disturbances are present in the waveforms due to unintentional converter stops related to gate-drive EMI problems. At the end of the record the temperatures are stabilized and it seems fair to consider them as final values. The ambient temperature varied during the test between 23 and 37°C. At the end of the test the ambient temperature was close to the design value 40°C so the test conditions are considered valid. As expected, the temperature of the central column (measured by thermocouples Tc2, Tc3, Tc4; position according to Appendix 4) is the highest, with Tc3 being the hotspot equal to 127°C ($\Delta T = 90$ K). The time constant of the hotspot is approximately 0.6 hours. The temperature of the side column (Tc10) is equal to 93°C. The primary winding temperature (Tc5) is 56°C and the secondary winding temperature (Tc6) is nearly the same as ambient.

The temperature of the insulation class H is respected. Moreover, it is likely that the transformer may be loaded with a higher power.

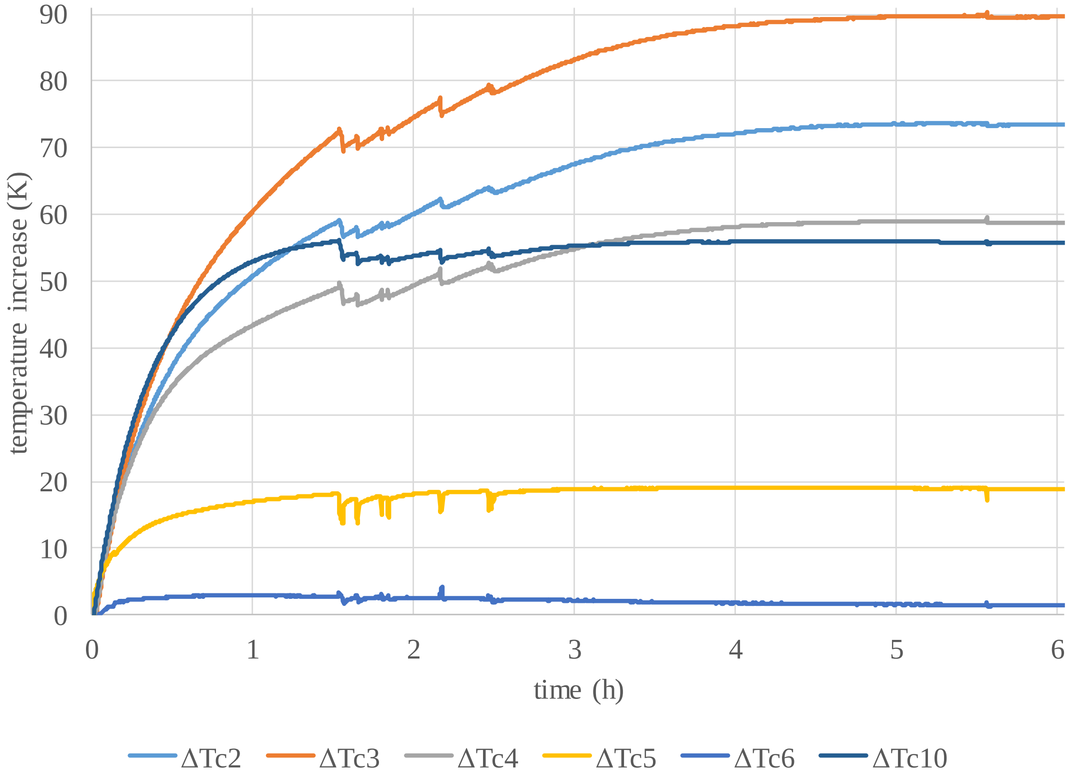

Fig. 6.7. Thermal test result of the 3-phase MFT: core (Tc2, Tc3, Tc4 and Tc10) and winding (Tc5 and Tc6) temperature increase $\Delta T$ at the maximum ambient temperature of 37°C

In Fig. 6.8 there is presented the measured temperature distribution on the MFT surface using a thermal camera Flir A325 [53]. The values should be considered approximate as the default thermal camera emissivity coefficients where used. The temperature measurement could be more precise if the emissivity coefficients were set. The general trend of temperature distribution is confirmed. The core central column is the hottest. The core yoke is cooler than the core side columns due to a better heat exchange. The external winding is nearly at the ambient temperature.

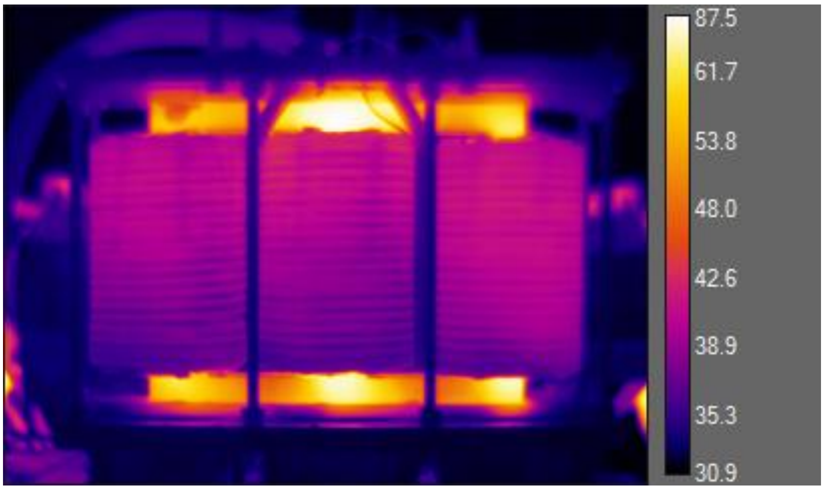

Fig. 6.8. Thermal image of the 3-phase MFT

In Fig. 6.9 it is presented the comparison between the thermal simulation and thermal measurement. The temperature on the core surface is plotted and the values at the thermocouple localisations are displayed. The red text gives the simulation result and the black text gives the measurement result. The temperature of the side column is very similar with the simulated value of 90°C and measured 93°C. The temperature of the central column is quite similar with the surface hotspot temperature simulated at 120°C and measured around 127°C. The distribution of the temperature along the column height is not the same. The simulation indicates the hotspot localisation in the 2/3 of the column height whereas the measurement indicates it in the column centre.

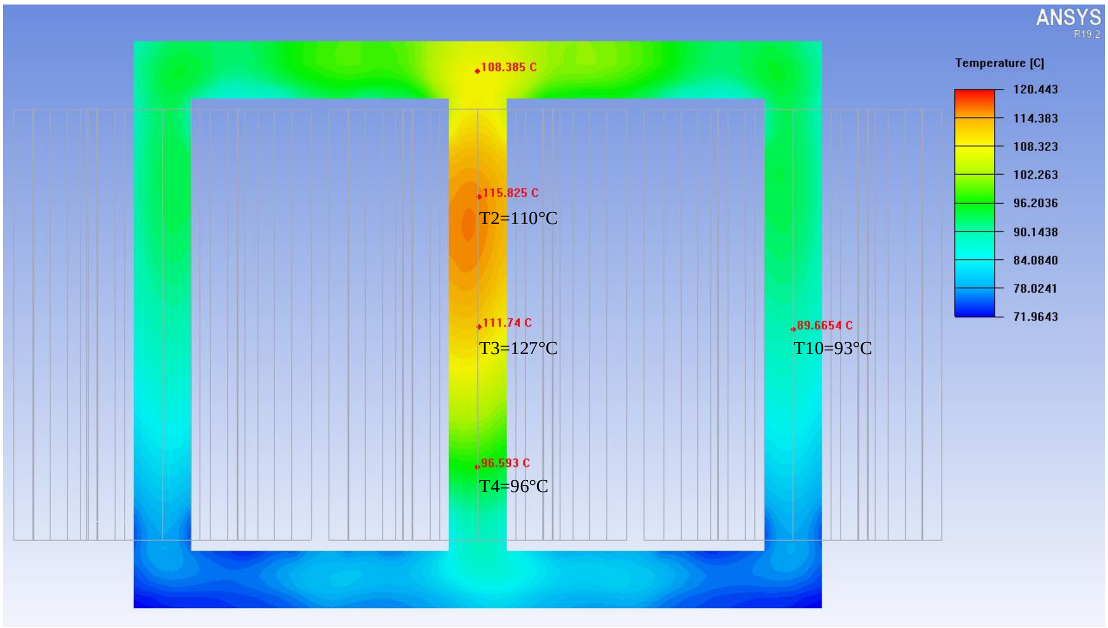

Fig. 6.9. Comparison of the thermal simulation and thermal measurement

### 6.1.3. Efficiency measurement

The measurement of the DC-DC converter efficiency was done based on the power measurement of the DC supply according to Fig. 6.2, using the precision power analyser ZES Zimmer LMG670 [201]. This measurement technique was proven to be the most effective and rather overestimating the DC-DC converter power loss. This measurement takes into account the power loss of the complete test bench, including the inductors and wiring.

The efficiency measurement result is presented in Fig. 6.10. At $U_{dc1} = U_{dc2} = 1200$ V and 100 kW, the DC-DC efficiency is 99.2%. A maximum efficiency of 99.25% is observed at 70 W. Considering the transformer power loss contribution, the shape of the curve is as expected. The low efficiency at low power is likely due to the loss of ZVS in the VSC [96], [98].

Assuming that the half of the power loss accounts for MFT and the half for the power semiconductors, the 3-phase MFT efficiency is approximately 99.6% what is a very good result. Some additional investigations are presented in Appendix 5.

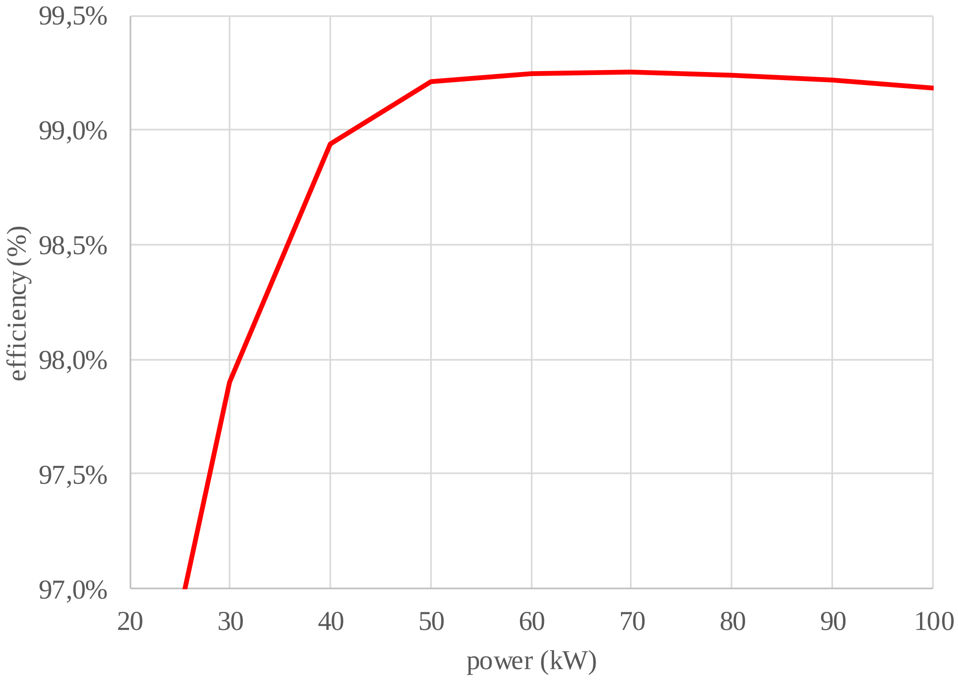

Fig. 6.10. Efficiency measurement result of the DAB3

## 6.2. Analysis of parasitic air gaps

### 6.2.1. Introduction

In chapter 4 the design of 3-phase MFT prototype is presented. In particular, the difficulty in the core assembly is highlighted. The core is assembled with multiple I-cores since the C-cores and E-cores do not exist for such big transformers. Each I-core measures 25 mm x 25 mm x 100 mm (see Appendix 4). The core assembly is presented in Fig. 6.11 for two MFT prototypes T1 and T2. In this core design, the I-cores are not interleaved. It can be seen that the core involves multiple parasitic air gaps. Moreover, due to manufacturing tolerances, the I-core is not an ideal rectangular cuboid and its dimensions vary from one sample to another. This causes the non-uniform parasitic air gaps in the core. There are at least two types of parasitic air gaps: perpendicular and longitudinal to the axis of the magnetic flux path. The author claim that the parasitic air gap size is unpredictable at the industrial design stage and that it cannot be modelled precisely.

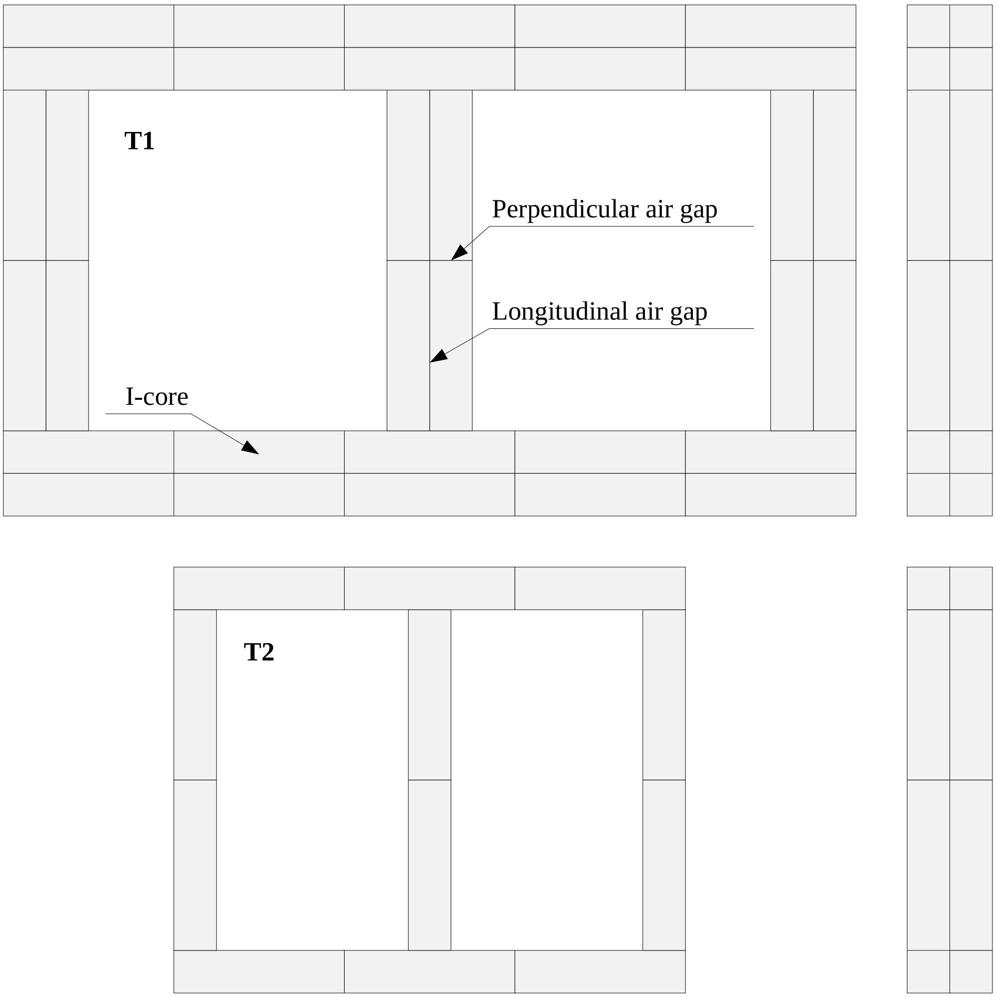

Fig. 6.11. 3-phase MFT core assembly composed of elementary I-cores: T1 (top) and T2 (bottom)

In Fig. 6.12, two example views of the ferrite core assembly are presented where the perpendicular and longitudinal parasitic air gaps can be observed up to about 0.5 mm. In each assembly, 4 randomly selected I-cores are aligned along a calliper on a flat surface. The I-cores are assembled tight together meaning that even if there is an air gap on the visible surface then there is somewhere a direct contact between the neighbour I-cores. In the 3-phase MFT core assembly, composed of tens of I-cores, the air gaps are even larger due to the cumulating I-core misalignments.

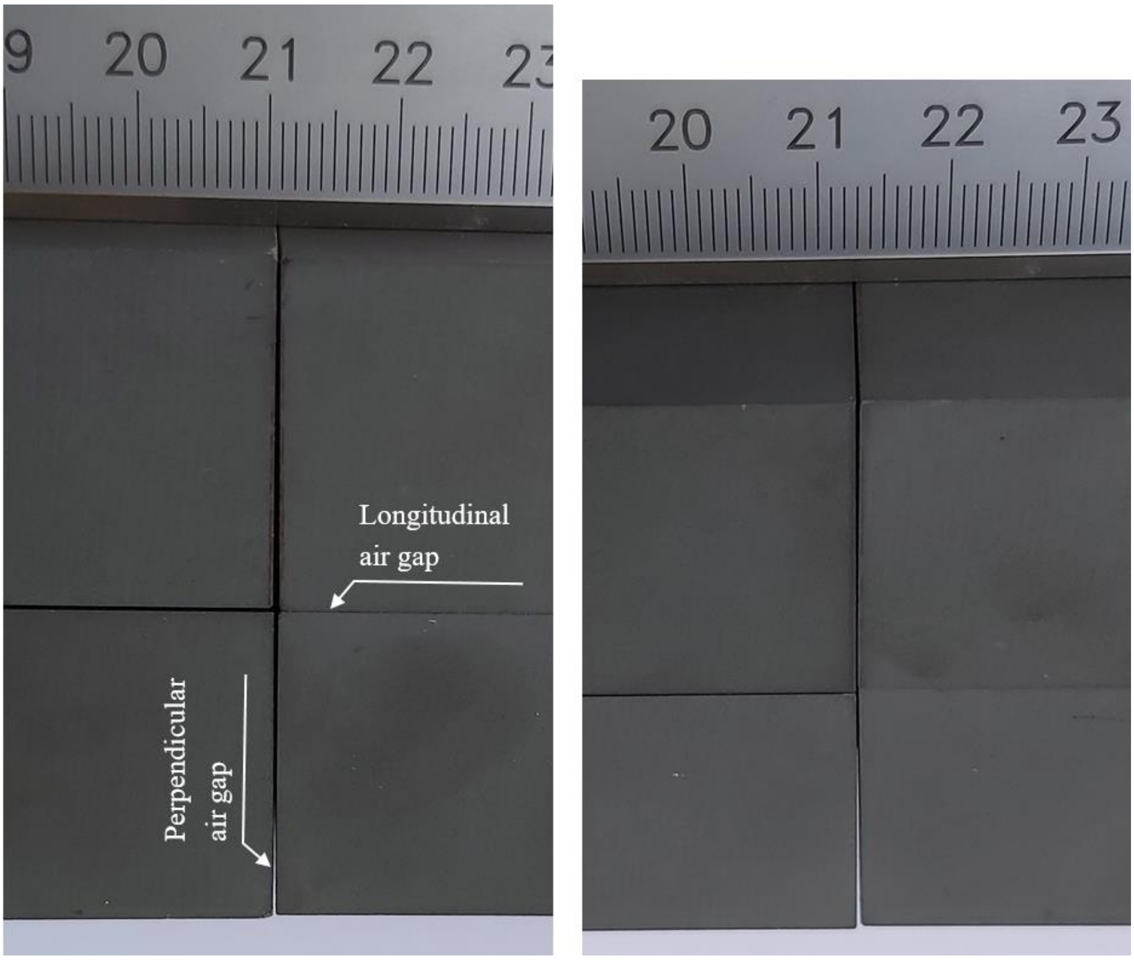

Fig. 6.12. Two assemblies of 4 randomly selected 3C90 ferrite I-cores showing the perpendicular parasitic air gap and the longitudinal parasitic air gap measuring up to about 0.5 mm

The influence of the perpendicular air gap on the relative permeability and power loss are discussed in two following sections.

### 6.2.2. Equivalent permeability and magnetizing inductance

In §5.3.2 the measurement setup for the equivalent *B*(*H*) of a 3-phase transformer is presented. The measurement was performed for two MFT prototypes T1 and T2. In Fig. 6.13 the equivalent *B*(*H*) measurement setup is presented with the MFT T2.

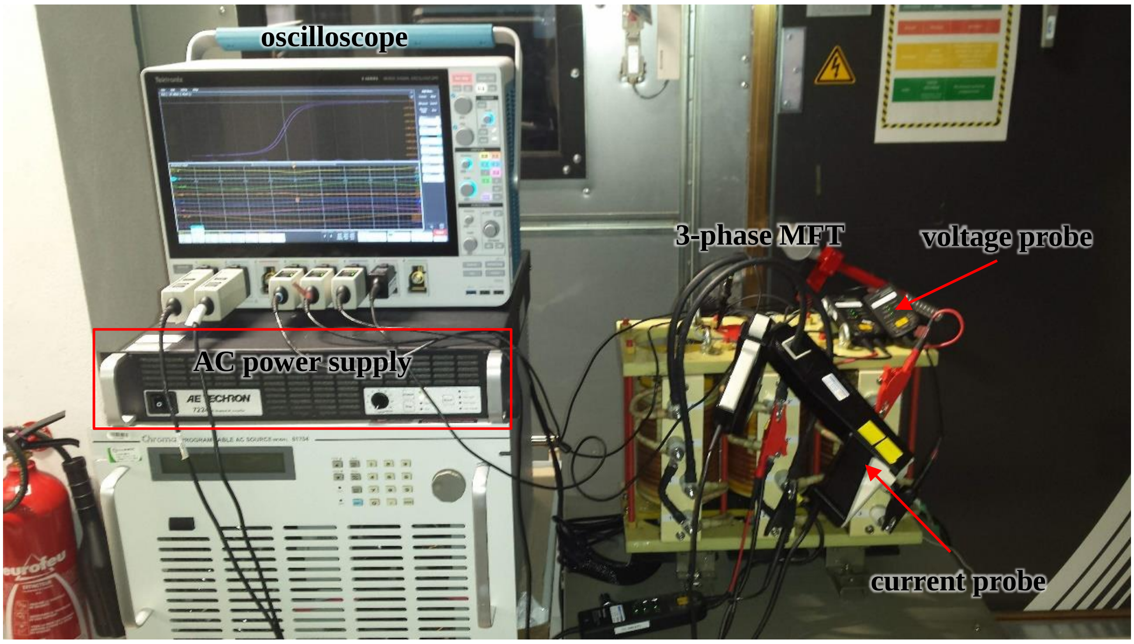

Fig. 6.13. Measurement of the equivalent *B*(*H*)

In Fig. 6.14 the measured equivalent anhysteretic *B*(*H*) is presented and compared against the material datasheet [51]. The *B*(*H*) curves are further linearized as presented in Fig. 6.14 (dashed line) and the corresponding linearized relative permeability is calculated.

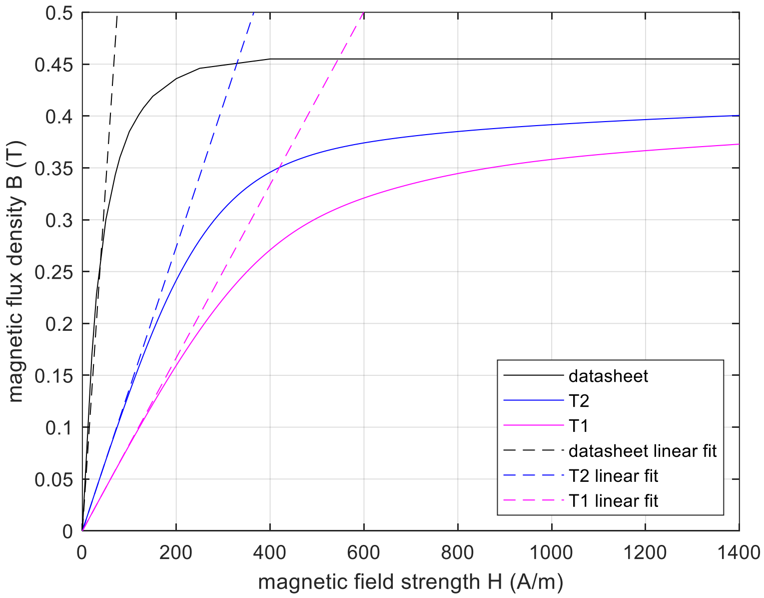

Fig. 6.14. Equivalent anhysteretic *B*(*H*): datasheet and measurement (solid line), linear interpolation (dashed line)

From Fig. 6.11 we can count the number of perpendicular parasitic air gaps along the magnetic path. This equals to 10 and 14 for T2 and T1 respectively. The core used for datasheet measurement had no air gaps according to standards [210]. The value of datasheet linearized relative permeability which equals $\mu_{r0} = 5300$ is read from Fig. 6.14. Thus, the equivalent relative permeability ratio $K_\mu$ of the multi air gap core can be calculated with:

$$K_\mu = \frac{\mu_r}{\mu_{r0}} \tag{6.1}$$

where $\mu_r$ is the equivalent relative permeability defined in Fig. 6.14 for T1 or T2. The equivalent relative permeability ratio is plotted in Fig. 6.15 as a function of a number of parasitic air gaps. It can be observed that the ratio is decreasing with the increase of the number of parasitic air gaps.

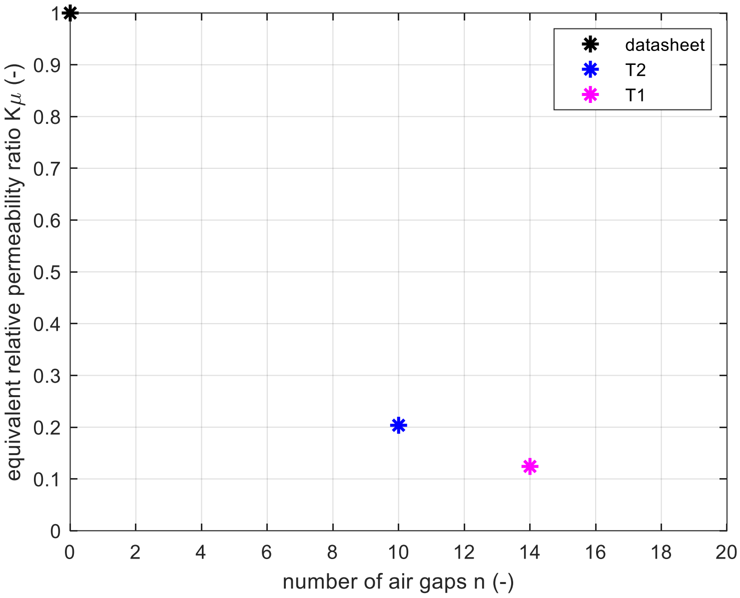

Fig. 6.15. Equivalent relative permeability ratio $K_\mu$ in the function of a number of parasitic air gaps $n$: datasheet, T2 and T1 measurement

In the MFT design process from-scratch, when evaluating the influence of magnetizing inductance on the performance of isolated DC-DC converters, the equivalent $B(H)$ cannot be measured because the transformer does not exist yet. However, the geometry of the transformer is known so the number of parasitic air gaps can be counted.

In Fig. 6.15 it is observed that the relative permeability ratio is nonlinearly decreasing with the increase of the number of parasitic air gaps $n$. An exponential interpolation function is proposed allowing to estimate the equivalent relative permeability for any high-power ferrite core MFT with similar core assembly. The exponential interpolation function is defined as:

$$K_\mu(n) = e^{-0.155n} \tag{6.2}$$

This function was validated with the experimental $B(H)$ measurement on two single-phase multi air gap (MAG) transformers presented in Appendix 4. The MAG4 transformer has four air gaps and MAG6 has six air gaps. Both use the same I-cores as T1 and T2. The resulting ratios are displayed in Fig. 6.16 and they are compared against the proposed exponential interpolation function showing a good fit. It can be seen that for MAG4 the ratio is slightly higher than the exponential interpolation. This is normal because for this transformer the I-cores were carefully selected to minimize the parasitic air gaps and the core assembly is simpler compared to the 3-phase MFT. However, a general trend of the equivalent relative permeability ratio is clearly observed even if the four MFT prototypes involve different technologies and different manufacturers.

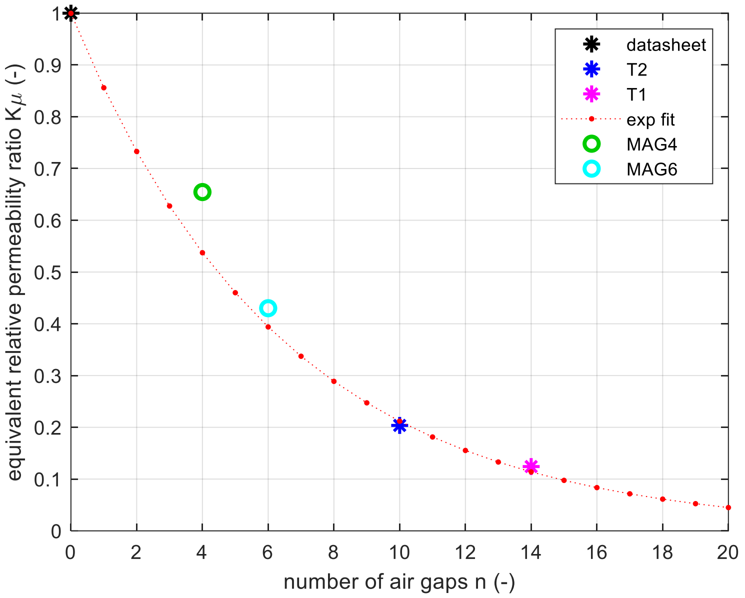

Fig. 6.16. Equivalent relative permeability ratio $K_\mu$ in the function of a number of parasitic air gaps *n*: datasheet, T2 and T1 measurement (stars), exponential interpolation (red dashed line), and single-phase multi air gap transformer MAG4 and MAG6 measurement (circles)

Furthermore, a simple reluctance model of the magnetic core neglecting the fringing effect is considered according to [10]. The total magnetic circuit reluctance can be related to the sum of the I-core and air gap reluctances as:

$$\frac{l_m}{\mu_0 \mu_r A_c} = n \frac{l_I}{\mu_0 \mu_{r0} A_c} + \frac{l_a}{\mu_0 A_c} \tag{6.3}$$

where $l_m$ is the average magnetic circuit length, $l_I$ is the length of the I-core, $l_a$ is the average air gap length, and $A_c$ is the average cross-section of the core. Assuming that the average magnetic circuit length $l_m$ is equal to $n \cdot l_I$, then it can be found the relative average air gap length $l_a/l_m$ defined as:

$$\frac{l_a}{l_m} = \frac{1}{\mu_r} - \frac{1}{\mu_{r0}} \tag{6.4}$$

Considering an ideal core assembly, where the average air gap length $l_a$ equals *n* times the known individual air gap length $l_g$, the relative average air gap length $l_a/l_m$ is a linear function of *n*:

$$\frac{l_a}{l_m} = \frac{l_g}{l_m} n \tag{6.5}$$

In Fig. 6.17, these linear functions are presented for four transformers T2, T1, MAG4, and MAG6. It was verified that the individual air gap length $l_g$ changes between prototypes. However, considering the proposed exponential interpolation (6.2), the effective relative average air gap length is a nonlinear function of *n* as presented in Fig. 6.17. This is due to the fact that the I-core is not an ideal rectangular cuboid and its dimensions vary from one sample to another. As a consequence, the mechanical assembly of the core gets more difficult when a large number of I-cores is assembled.

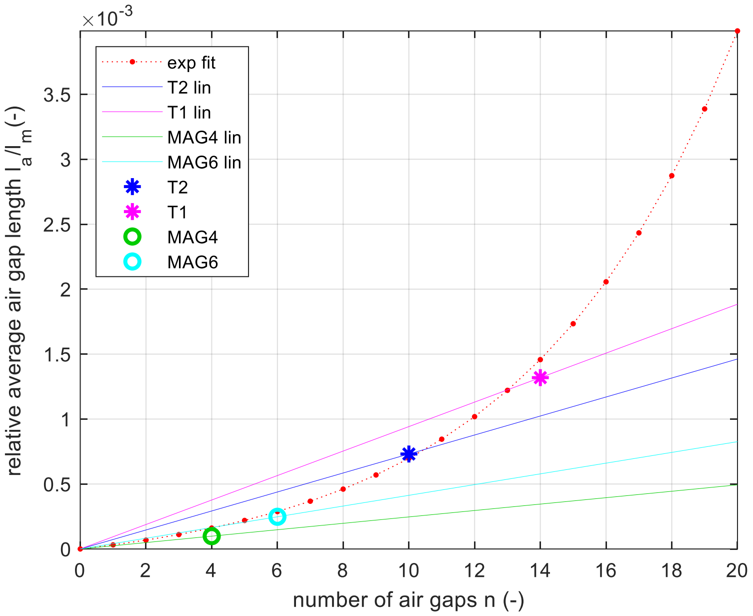

Fig. 6.17. Relative average air gap length $l_a/l_m$ in the function of a number of parasitic air gaps $n$: T2, T1, MAG4 and MAG6 measurement (stars/circle), the corresponding idealized reluctance model (solid lines), and the relative average air gap length calculated based on the proposed exponential interpolation (red dashed line)

The proposed approach can be used in scaling the datasheet $B(H)$ for a finite element simulation, in the rapid estimation of transformer magnetizing inductance or in evaluating the size of the equivalent parasitic air gap. The magnetizing inductance can be estimated based on the magnetic reluctance model according to:

$$L_m = K_\mu(n)\frac{\mu_0 \mu_{r0} N^2 A_c}{l_m} \tag{6.6}$$

where $N$ is the primary/secondary number of turns. It shall be mentioned that the proposed estimation is meant to provide an order of magnitude of the magnetizing inductance. This shall be sufficient when evaluating the performance of isolated DC-DC converters.

This analysis was reported by the author in [42] and proves the thesis 2.

### 6.2.3. Power losses

It is known that in gapped magnetic components the fringing flux may cause an increase of power loss and a local increase of the temperature [6], [145]. The fringing flux may generate the eddy current effect losses in any conductive material near the air gap. The transformer winding is usually placed close to the magnetic core so it may experience a power loss increase and a local temperature increase.

In [11] a modification of the Steinmetz equation for gapped magnetic cores was proposed. It shows that the increase of the air gap size causes a decrease of the core power loss density.

The author has contributed to the analysis reported in [187] showing the experimental investigations of the influence of the air gap size on the power losses in ferrite core transformers. In this work the MAG4 (Appendix 4) transformer was built allowing to easily change the size of the air gap. The thickness of the air gap was adjusted by two symmetrical diamagnetic spacers placed between the yoke and columns of the transformer as presented in Fig. 6.18.

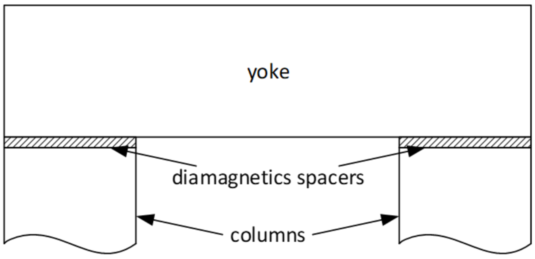

Fig. 6.18. Arrangement of the spacers in the multi air gap transformer for the controlled value of the air gap size

A special test bench was prepared for measuring the power losses of the MAG4 transformer as presented in Fig. 6.19. The parameters of the supply voltage were set in the signal generator and then amplified. The power measurement was made with a precision power analyser ZES Zimmer LMG670 [201]. The accuracy of the power measurement is guaranteed by the delay time between voltage and current input lower than 3 ns. The transformer was supplied by sinusoidal voltage with the frequency in the range from 10 kHz to 50 kHz and the amplitude up to 100 V. In order to perform measurements with invariable average magnetic flux density in the core, a constant *U*/*f* ratio of supply voltage was kept.

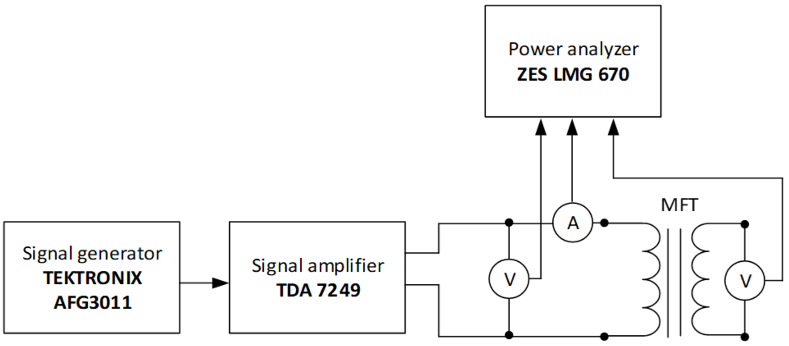

Fig. 6.19. Test bench for measuring the power losses of the multi air gap transformer

In Fig. 6.20 the transformer no load power loss as a function of supply frequency is presented. The measurements for the natural air gap are marked as D0, for the air gap increased by 100 µm as D1 and by 200 µm as D2. Due to the low magnetizing current and the litz type winding, the losses in the transformer winding are negligibly small. Analysing the results of measurements at the same frequency and flux density in the core, it can be noticed that the power loss decreases with the increase of the air gap. The maximum difference is about 20%, and the trend is noticeable at all flux density values in the core. This phenomenon was confirmed by the FEM simulations presented in [187].

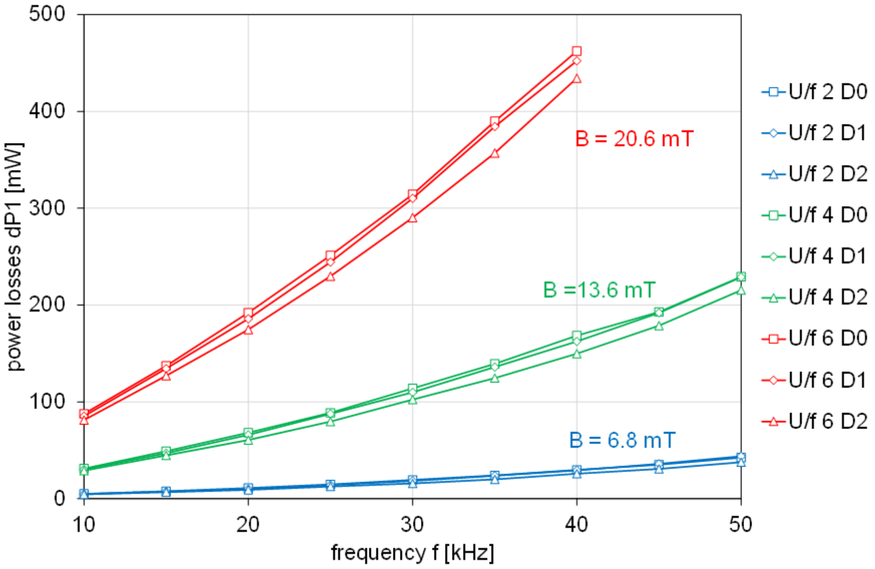

Fig. 6.20. Transformer no-load power losses as a function of a supply voltage frequency at different flux density values (constant *U*/*f* ratio) and various air gaps (D0, D1, D2)

Furthermore, the thermal test with the 3-phase MFT detailed in §6.1.2 did not reveal any noticeable influence of the air gaps neither on the core temperature distribution nor on the winding temperature distribution.

The presented analysis, also reported in [187], confirms the statement of [11] that the increase of the air gap size causes a decrease of the core power loss in the considered air gap range. Moreover, in the 3-phase MFT no noticeable influence was observed on the core and winding temperature distribution. It can be concluded that in terms of power loss and temperature, the MFT core assembly with multiple I-cores does not cause any undesirable effects in the core. Moreover, in the 3-phase MFT prototype the multiple parasitic air gaps do not cause any measurable effect on winding power loss and temperature.

## 6.3. Model verification and analysis

### 6.3.1. Introduction

In chapter 3 the model of the 3-phase MFT in a DAB converter is developed and in chapter 5 the model parameters are calculated. The model can be implemented in any computational software. The author has implemented it in a Matlab script according to Appendix 1. In the following sections the model is validated against the experiment and some analyses are performed.

### 6.3.2. Effect of magnetic cross saturation in no-load test

In the MFT no-load test, the VSC1 is supplied from the DC power supply, and the AC terminals of the VSC2 are disconnected. The VSC1 operates normally with $U_{dc1}$ = 1200 V. In Fig. 6.21 and Fig. 6.22, the simulation result is compared against the MFT no-load steady-state test measurement. The voltage waveforms show good synchronization between the simulation and the measurement. The measured magnetizing current is compared against two simulation models: a classical simplified model neglecting magnetic cross saturation [83], and the proposed complete model including the cross saturation. In reference to the cross-saturation model characterized by (3.24), the simplified model is characterized by:

$$\mathbf{\Phi_m} = \begin{bmatrix} \Phi_{m1}(\Theta_{g1}) \\ -\Phi_{m1}(\Theta_{g1}) - \Phi_{m3}(\Theta_{g2}) \\ \Phi_{m3}(\Theta_{g2}) \end{bmatrix} \tag{6.7}$$

The cross-saturation model shows quite a good fit with the measurement. Some small differences are due to the asymmetry between three columns. The classical simplified model fits a bit less, but it also gives acceptable results. Some current oscillations in the measured current are observed due to the effect of parasitic capacitances. However, these oscillations are relatively low so the validity of the model simplification neglecting winding capacitances is proven.

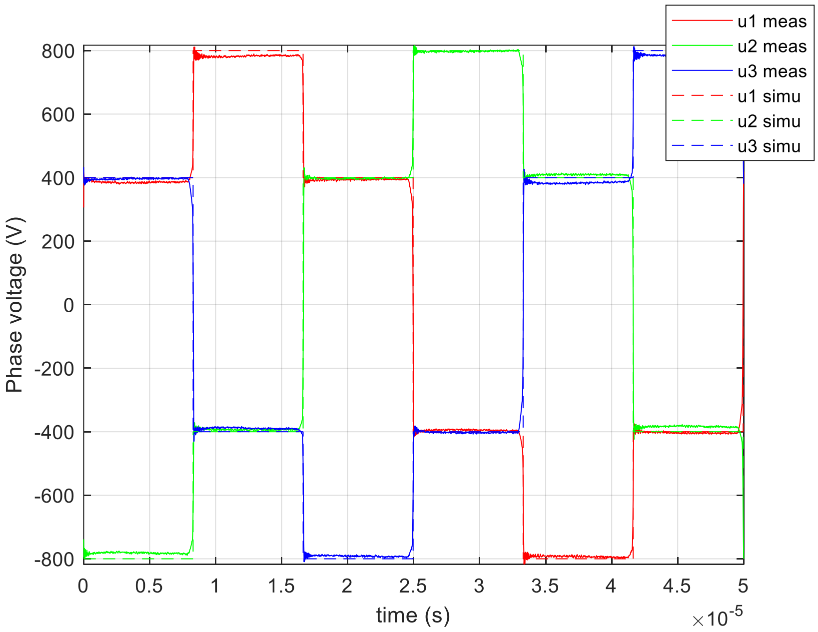

Fig. 6.21. MFT no-load steady-state test - comparison of transformer phase voltage waveforms: simulation model (dashed line) and measurement (solid line)

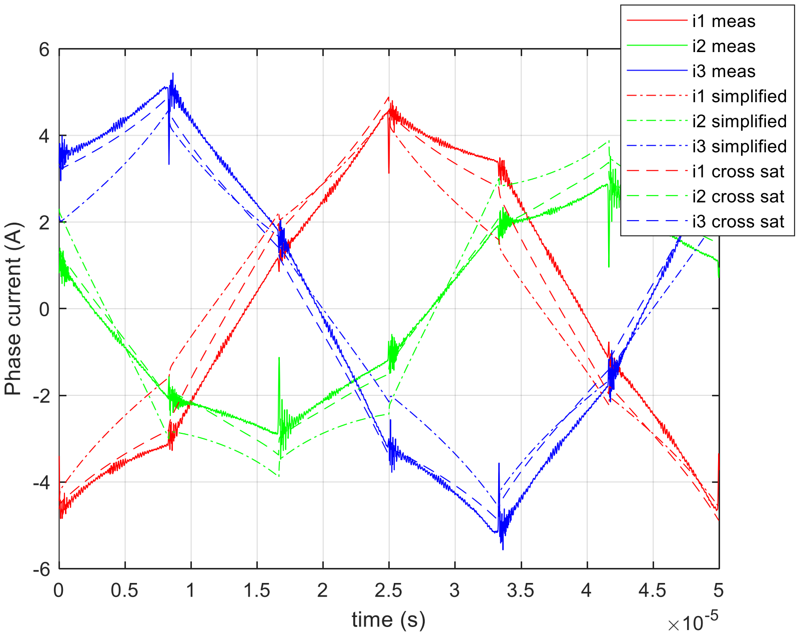

Fig. 6.22. MFT no-load steady-state test - comparison of magnetizing current waveforms: simplified model (dash-dotted line), cross saturation model (dashed line) and measurement (solid line)

In Fig. 6.23, the classical simplified model simulation result is compared against the MFT no-load inrush test measurement. A very significant difference is observed, especially in the current of the central column $i_2$. The amplitude of the simulated current is more than two times higher than the measured current.

In Fig. 6.24, the proposed cross saturation model simulation result is compared against the MFT no-load inrush test measurement. A very good fit is observed in the magnetizing current. This proves the accuracy of the proposed model and method for model parameter calculation. In particular, this test confirms the validity of the multi-dimensional characteristic of magnetizing flux $\mathbf{\Phi}_\mathbf{m}(\mathbf{\Theta})$ presented in §5.3.6.

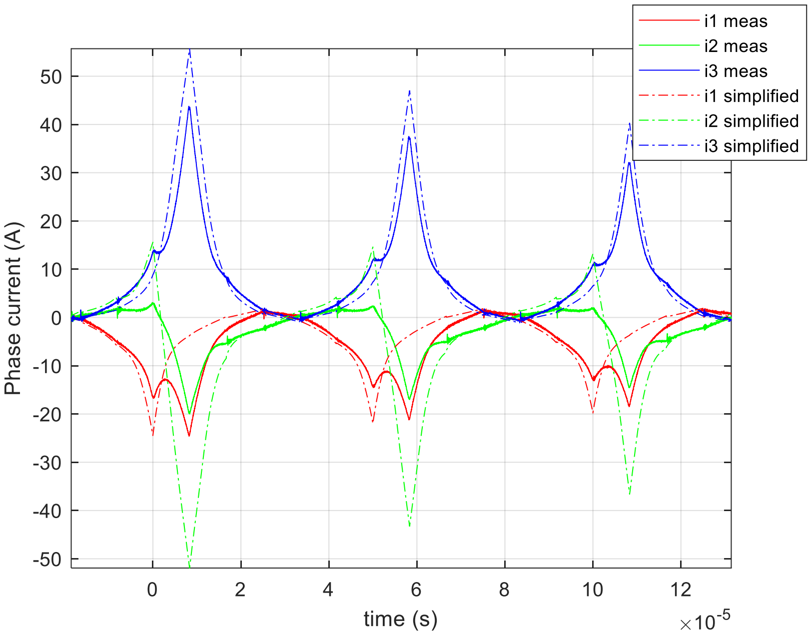

Fig. 6.23. MFT no-load inrush test - comparison of magnetizing current waveforms: simplified model (dash-dotted line) and measurement (solid line)

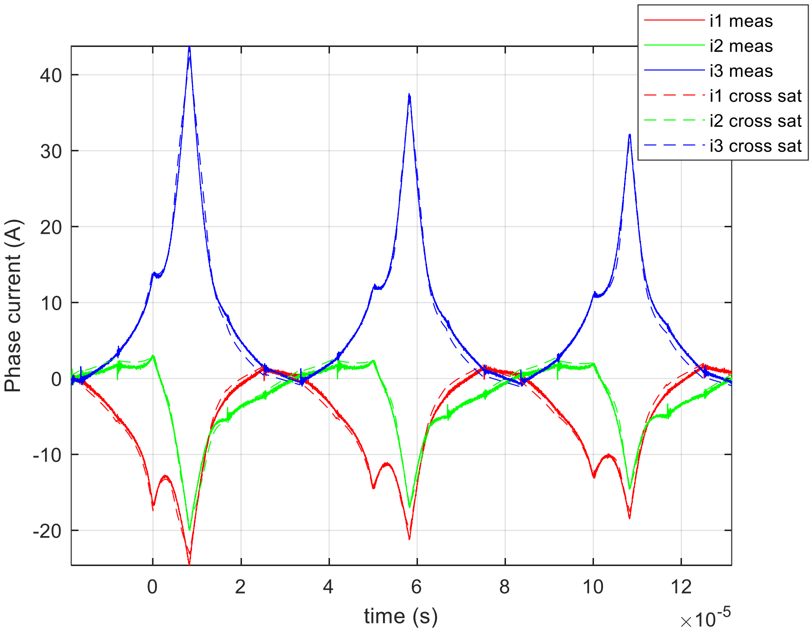

Fig. 6.24. MFT no-load inrush test - comparison of magnetizing current waveforms: cross saturation model (dashed line) and measurement (solid line)

In Fig. 6.25, the magnetizing current is displayed on the surface plot of the magnetizing flux $\Phi_{m3}$ as the function of the magnetizing MMF. This allows to observe the effect of magnetic cross saturation. Indeed, the saturation of winding 3 is influenced by the value of the current in winding 1 (and winding 2, due to the Yy connection).

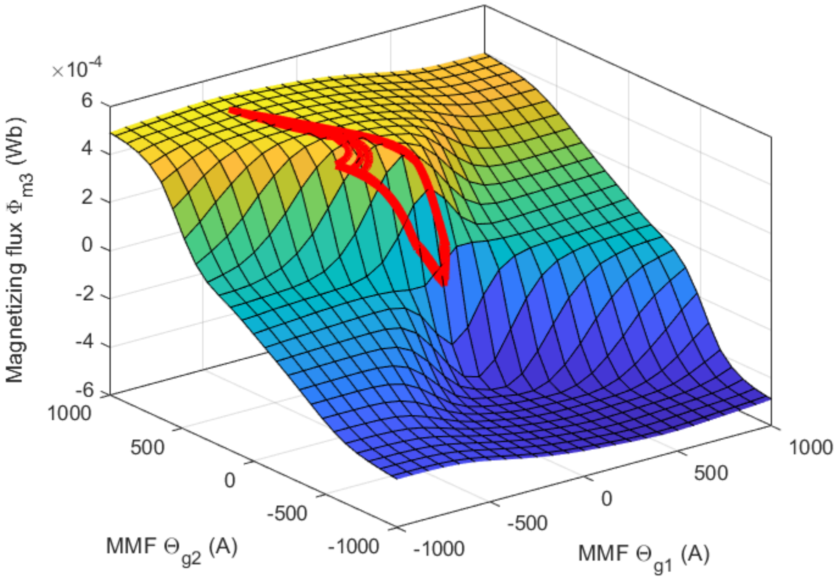

Fig. 6.25. MFT no-load inrush test - visualization of the magnetizing current from Fig. 6.24 on the surface plot of magnetizing flux $\Phi_{m3}$ as function of the magnetizing MMF in generalized coordinates $\Theta_{g1}$ and $\Theta_{g2}$

In the no load inrush test the winding resistance was multiplied by 33 in order to take into account the transient increase in the core loss which is not modelled properly with the proposed equivalent circuit for core power loss. This issue could be solved by implementing the time or voltage dependent $R_{eh}$ [186] or by implementing the hysteresis from §3.3.2 in the circuit model.

This analysis has been accepted for publication in [40].

### 6.3.3. Effect of mutual leakage inductance in DAB converter operation

Fig. 6.26 and Fig. 6.27 compare the model simulation result against the DAB steady-state test measurement at approximately 100 kW. A good fit is observed in the phase shift $\delta$ between the primary and secondary voltage, and as the consequence in the current waveform. A small difference is probably due to the fact that the inductance of connection wires is neglected in the model. The experiment was performed in the power regulation mode, considering the precision of the available transducers (in the range of ±5%). The simulation was performed with the constant $\delta$ according to (2.10). This test proves in particular the validity of the leakage inductance matrix (Table 5.3). It can be seen that the linearization of the leakage inductance matrix was a fair assumption since it has a negligible influence on the steady-state waveforms.

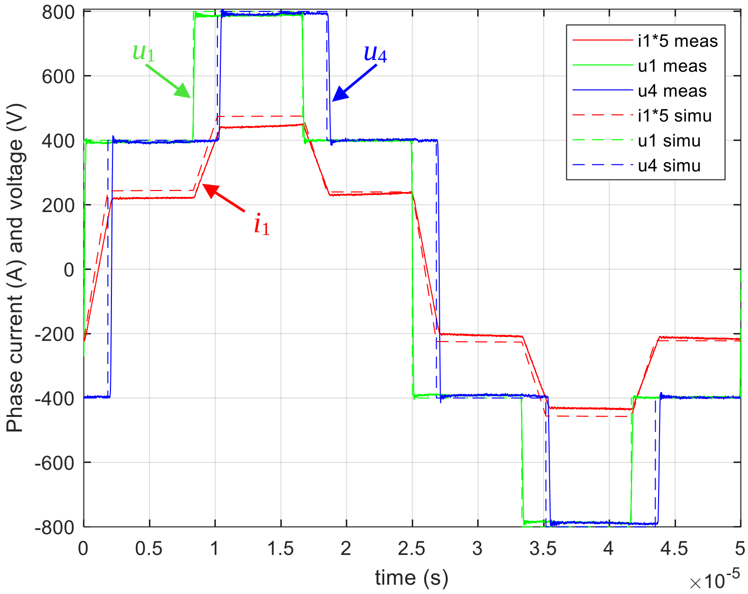

Fig. 6.26. DAB full-load test - comparison of current and voltage waveforms: simulation (dashed line) and measurement (solid line); current values are multiplied by 5

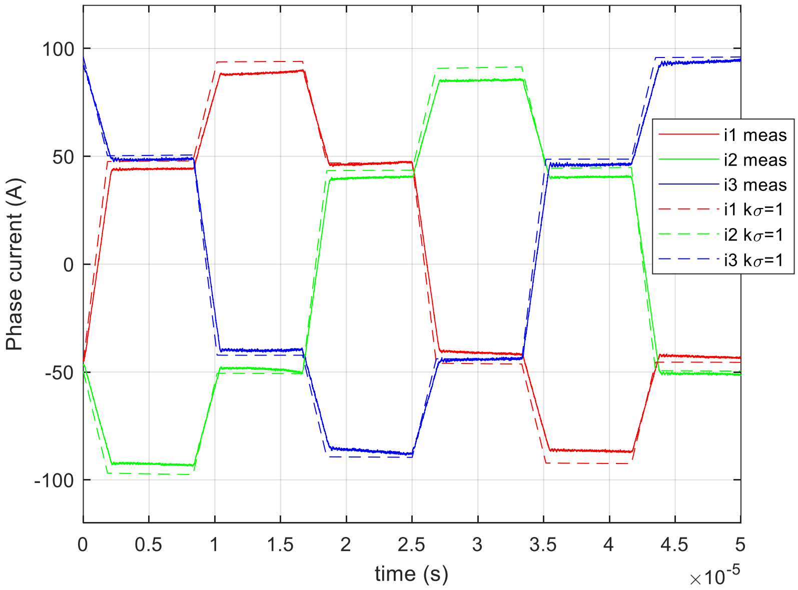

Fig. 6.27. Comparison of 3-phase DAB current waveforms: simulation resulting in 106 kW (dashed line) and measurement (solid line)

In order to analyse the influence of the mutual leakage inductances on the DAB converter operation, the cross-coupling leakage inductance values are multiplied by a coefficient $k_\sigma$:

$$\mathbf{L}_\sigma = \begin{bmatrix} L_{\sigma 1,1} & L_{\sigma 1,2}k_\sigma & L_{\sigma 1,3}k_\sigma & L_{\sigma 1,4} & L_{\sigma 1,5}k_\sigma & L_{\sigma 1,6}k_\sigma \\ L_{\sigma 2,1}k_\sigma & L_{\sigma 2,2} & L_{\sigma 2,3}k_\sigma & L_{\sigma 2,4}k_\sigma & L_{\sigma 2,5} & L_{\sigma 2,6}k_\sigma \\ L_{\sigma 3,1}k_\sigma & L_{\sigma 3,2}k_\sigma & L_{\sigma 3,3} & L_{\sigma 3,4}k_\sigma & L_{\sigma 3,5}k_\sigma & L_{\sigma 3,6} \\ L_{\sigma 4,1} & L_{\sigma 4,2}k_\sigma & L_{\sigma 4,3}k_\sigma & L_{\sigma 4,4} & L_{\sigma 4,5}k_\sigma & L_{\sigma 4,6}k_\sigma \\ L_{\sigma 5,1}k_\sigma & L_{\sigma 5,2} & L_{\sigma 5,3}k_\sigma & L_{\sigma 5,4}k_\sigma & L_{\sigma 5,5} & L_{\sigma 5,6}k_\sigma \\ L_{\sigma 6,1}k_\sigma & L_{\sigma 6,2}k_\sigma & L_{\sigma 6,3} & L_{\sigma 6,4}k_\sigma & L_{\sigma 6,5}k_\sigma & L_{\sigma 6,6} \end{bmatrix} \qquad (6.8)$$

The mutual leakage inductance of the column is unchanged in order to keep unchanged the equivalent leakage inductance of the classical transformer model according to (5.12). The influence of the classical equivalent leakage inductance is well known (§2.3) so it is not analysed here.

In Fig. 6.28, the simulation result with $k_\sigma = 0.8$ is presented. The simulated current waveforms are slightly different from the experiment, in particular in the phase 2. The active power is increased by 8% for the 20% decrease in the cross-coupling leakage inductance. According to (2.10) a 20% decrease in $L_{ac}$ results in 26% active power increase. This means that in terms of the DAB power transfer, the influence of the leakage inductance on the same column is approximately 3 times higher than the influence of the cross-coupling leakage inductance.

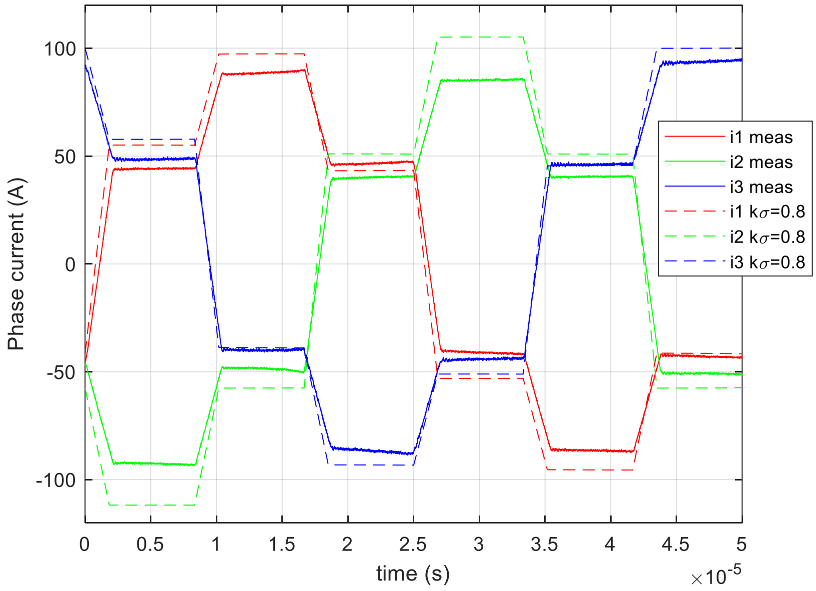

Fig. 6.28. Comparison of 3-phase DAB current waveforms: simulation with $k_\sigma$=0.8 resulting in 114 kW (dashed line) and measurement (solid line)

The analyses presented in §6.3 prove the thesis 3.

# 7. Conclusions and perspectives

The evolutions in power systems and electric vehicles, related to the economic opportunities and the environmental issues, bring the need of high-power isolated DC-DC converter. The medium frequency transformer is one of its key components, enabled by the increasing switching frequency of modern power semiconductors like silicon carbide transistors or diodes. The increased operating frequency offers the small converter size leading to the decrease in raw material usage. Most likely this will result in the converter cost reduction what will further increase the demand for the solid-state transformer solutions. The modelling and analysis are essential in the development of the MFT technology which is attracting lots of research and industrial interest.

The mathematical model of the MFT in the dual active bridge converter was proposed. The Lagrange energy method was used to derive a physically motivated model for circuit analysis. The feedback Preisach model of hysteresis was developed. The design of a 3-phase 20 kHz transformer for a 100 kW 1.2 kV isolated DC-DC power converter was presented resulting in two 3-phase MFT prototypes. The experimental test results on the prototype MFT were presented including the thermal test and efficiency measurement. The influence of the parasitic air gaps on the equivalent magnetic permeability, average air gap length and power losses was discussed. The effect of magnetic cross saturation and mutual leakage inductance was studied. The presented work enabled to prove the three theses of this dissertation.

The feasibility of the 3-phase MFT has been proven with 2 unique prototypes. The experimental tests, including the thermal test, validate the proposed design. The developed 3-phase MFT prototype operating at 20 kHz is more than 10 times lighter than the equivalent 3-phase 50 Hz transformer. The 3-phase 100 kW DC-DC converter efficiency was measured 99.2% which is higher than the equivalent single-phase variant.

The challenge of high power MFT design related to the parasitic air gaps in the core was highlighted. The influence of the air gaps on the core power loss was confirmed. The increase of the air gap size in a certain range causes a decrease of the core power loss. Moreover, in the 3-phase MFT prototype, the parasitic air gaps do not cause any measurable effect on winding power loss and temperature. However, it was shown that the relative permeability is nonlinearly decreasing with the increase of the number of parasitic air gaps. An exponential interpolation function was proposed allowing to estimate the equivalent relative permeability for any high-power ferrite core MFT with a similar core assembly.

The proposed MFT equivalent circuit model has been proven accurate in steady state and transient analyses. The no-load inrush test confirmed the importance of the magnetic cross saturation involved in the magnetizing flux $\mathbf{\Phi_m(\Theta)}$. The influence of the mutual leakage inductance on the operation of the DAB converter was shown. The feedback Preisach model of hysteresis has been proven accurate in the modelling of hysteresis loops of multi air gap ferrite core MFT.

The main achievements of this dissertation include the novelties:

- Lagrangian model of the 3-phase DAB for electromagnetic transient and steady state simulation,
- 3-phase MFT model accounting magnetic cross saturation for precise steady state and transient analyses; the model involves a matrix of nonlinear magnetizing inductances and a matrix of linear leakage inductances, both including self and mutual values,

- Feedback Preisach model of hysteresis for multi air gap MFT composed of type "I" MnZn ferrite cores,
- 3-phase MFT prototype for a 100 kW 20 kHz DC-DC power converter,
- Determination of the equivalent $B(H)$, the equivalent magnetic permeability and the average air gap length in a 3-phase multi air gap ferrite core MFT,
- Practical approach to the determination of 3-phase MFT model parameters based on magnetostatic FEM simulations,
- Demonstration that the equivalent magnetic permeability and the average air gap length of the multi air gap ferrite core MFT are nonlinear functions of the number of air gaps,
- Proposal of an exponential scaling function enabling a rapid estimation of the magnetizing inductance based on the ferrite material datasheet only.

The work realised during the doctoral studies has resulted in numerous publications:

- 1 journal article published in MDPI Energies [42],
- 1 journal article accepted for publication in IEEE Transactions on Power Delivery [40],
- 1 journal article submitted for publication in MDPI Energies [121],
- 2 conference papers [39], [41],
- 6 co-authored conference papers directly linked with this study [60], [61], [95], [96], [122] and [187].

The author has identified some perspectives including the most significant ones:

- implementation of the feedback Preisach model of hysteresis in the equivalent circuit model of a 3-phase medium frequency transformer,
- extension of the feedback Preisach model of hysteresis taking into account the effect of temperature,
- improvement of the transformer equivalent circuit model, taking into account winding resistance in a function of frequency according to [161],
- improvement of the equivalent circuit for core power loss allowing a precise core loss calculation in transient states (if the hysteresis model is not implemented),
- validation of the equivalent magnetic permeability scaling function with a larger number of transformer prototypes, elementary core dimensions and including the effect of temperature,
- precise comparison between the single-phase and 3-phase MFT and DC-DC converter,
- identification of a power loss measurement technique in medium frequency transformers,
- optimization of DC-DC converter design by adjusting the value of the leakage inductance,
- improvement of the electromagnetic interference in SiC based power converters.

# Bibliography

[1] ABB, “Why choose HVDC over HVAC.” [Online]. Available: https://new.abb.com/systems/hvdc/why-hvdc/economic-and-environmental-advantages. [Accessed: 30-Dec-2019].

[2] ABB, “MVDC and Grid Interties: enabling new features in distribution, sub-transmission and industrial networks,” 2019. [Online]. Available: https://library.e.abb.com/public/5fea768c835b4daeb8258bf950ddb05c/ABB%20MVDC_White%20paper.pdf?x-sign=X9LOXylnUBkKlMUPttFtrNFlHfODv7TYMZjoITkYE332BdplwYEgUSztjC9z/l58. [Accessed: 15-Mar-2020].

[3] ABB, “Dry-type low voltage transformers,” 2014. [Online]. Available: https://search-ext.abb.com/library/Download.aspx?DocumentID=1LES100025-ZD&LanguageCode=en&DocumentPartId=&Action=Launch. [Accessed: 12-Jan-2020].

[4] M. Adamowicz, “Power Electronics Building Blocks for implementing Smart MV/LV Distribution Transformers for Smart Grid,” *Acta Energetica*, vol. 4, no. 21, pp. 6–13, 2014.

[5] N. Ahmed, S. Norrga, H.-P. Nee, A. Haider, D. Van Hertem, L. Zhang, and L. Harnefors, “HVDC SuperGrids with modular multilevel converters — The power transmission backbone of the future,” in *International Multi-Conference on Systems, Signals Devices*, 2012, pp. 1–7.

[6] M. Albach and H. Rossmanith, “The influence of air gap size and winding position on the proximity losses in high frequency transformers,” in *2001 IEEE 32nd Annual Power Electronics Specialists Conference (IEEE Cat. No.01CH37230)*, 2001, vol. 3, pp. 1485–1490 vol. 3.

[7] O. Aldosari, L. A. Garcia Rodriguez, J. C. Balda, and S. K. Mazumder, “Design Trade-Offs for Medium- and High-Frequency Transformers for Isolated Power Converters in Distribution System Applications,” in *2018 9th IEEE International Symposium on Power Electronics for Distributed Generation Systems (PEDG)*, 2018, pp. 1–7.

[8] Alstom, “Coradia iLint – the world’s 1st hydrogen powered train,” *Alstom*. [Online]. Available: https://www.alstom.com/our-solutions/rolling-stock/coradia-ilint-worlds-1st-hydrogen-powered-train. [Accessed: 30-Dec-2019].

[9] Ansys, “Help.” [Online]. Available: https://ansyshelp.ansys.com/. [Accessed: 06-Mar-2020].

[10] A. Ayachit and M. K. Kazimierczuk, “Sensitivity of effective relative permeability for gapped magnetic cores with fringing effect,” *IET Circuits, Devices Systems*, vol. 11, no. 3, pp. 209–215, 2017.

[11] A. Ayachit and M. K. Kazimierczuk, “Steinmetz Equation for Gapped Magnetic Cores,” *IEEE Magnetics Letters*, vol. 7, pp. 1–4, 2016.

[12] M. A. Bahmani, “Design considerations of medium-frequency power transformers in HVDC applications,” in *2017 Twelfth International Conference on Ecological Vehicles and Renewable Energies (EVER)*, 2017, pp. 1–6.

[13] M. A. Bahmani, E. Agheb, T. Thiringer, H. K. Høidalen, and Y. Serdyuk, “Core loss behavior in high frequency high power transformers—I: Effect of core topology,” *Journal of Renewable and Sustainable Energy*, vol. 4, no. 3, p. 033112, May 2012.

[14] M. A. Bahmani, T. Thiringer, and M. Kharezy, “Optimization and experimental validation of medium-frequency high power transformers in solid-state transformer applications,” in *2016 IEEE Applied Power Electronics Conference and Exposition (APEC)*, 2016, pp. 3043–3050.

[15] J. P. S. Bala, “DC Connection of Offshore Wind Power Plants without Platform,” 2014.

[16] M. Birle and C. Leu, “Breakdown of polymer dielectrics at high direct and alternating voltages superimposed by high frequency high voltages,” in *2013 IEEE International Conference on Solid Dielectrics (ICSD)*, 2013, pp. 656–661.

[17] M. B. Blarke and B. M. Jenkins, “SuperGrid or SmartGrid: Competing strategies for large-scale integration of intermittent renewables?,” *Energy Policy*, vol. 58, pp. 381–390, Jul. 2013.

[18] M. Brokate and E. Della Torre, “The wiping-out property of the moving model (magnetic hysteresis),” *IEEE Transactions on Magnetics*, vol. 27, no. 5, pp. 3811–3814, Sep. 1991.

[19] A. Cabrera-Tobar, E. Bullich-Massagué, M. Aragüés-Peñalba, and O. Gomis-Bellmunt, “Topologies for large scale photovoltaic power plants,” *Renewable and Sustainable Energy Reviews*, vol. 59, pp. 309–319, Jun. 2016.

[20] S. Calabro, F. Coppadoro, and S. Crepaz, “The Measurement of the Magnetization Characteristics of Large Power Transformers and Reactors through D.C. Excitation,” *IEEE Transactions on Power Delivery*, vol. 1, no. 4, pp. 224–234, Oct. 1986.

[21] L. Chedot and G. Friedrich, “A cross saturation model for interior permanent magnet synchronous machine. Application to a starter-generator,” in *Conference Record of the 2004 IEEE Industry Applications Conference, 2004. 39th IAS Annual Meeting.*, 2004, vol. 1, p. 70.

[22] Chroma, “3-Phase Programmable AC Source - 61700.” [Online]. Available: https://www.chromausa.com/product/3-phase-programmable-ac-source-61700/. [Accessed: 08-Mar-2020].

[23] CIGRE WG C6.31, “Medium voltage direct current (MVDC) grid feasibility study,” Feb. 2020.

[24] Dassault Systèmes, “Opera - electromagnetic and electromechanical simulation.” [Online]. Available: https://www.3ds.com/products-services/simulia/products/opera/. [Accessed: 06-Mar-2020].

[25] R. W. A. A. De Doncker, D. M. Divan, and M. H. Kheraluwala, “A three-phase soft-switched high-power-density DC/DC converter for high-power applications,” *IEEE Transactions on Industry Applications*, vol. 27, no. 1, pp. 63–73, Jan. 1991.

[26] M. De Prada Gil, J. L. Domínguez-García, F. Díaz-González, M. Aragüés-Peñalba, and O. Gomis-Bellmunt, “Feasibility analysis of offshore wind power plants with DC collection grid,” *Renewable Energy*, vol. 78, pp. 467–477, Jun. 2015.

[27] R. W. DeDoncker, M. H. Kheraluwala, and D. M. Divan, “Power conversion apparatus for DC/DC conversion using dual active bridges,” US5027264A, 25-Jun-1991.

[28] R. C. Degeneff, “A general method for determining resonances in transformer windings,” *IEEE Transactions on Power Apparatus and Systems*, vol. 96, no. 2, pp. 423–430, Mar. 1977.

[29] R. C. Degeneff, M. R. Gutierrez, and P. J. McKenny, “A method for constructing a reduced order transformer model for system studies from detailed lumped parameter models,” in *Proceedings of the 1991 IEEE Power Engineering Society Transmission and Distribution Conference*, 1991, pp. 532–538.

[30] E. Della Torre and F. Vajda, “Parameter identification of the complete-moving-hysteresis model using major loop data,” *IEEE Transactions on Magnetics*, vol. 30, no. 6, pp. 4987–5000, Nov. 1994.

[31] F. Della Torre, A. P. Morando, and G. Todeschini, “Three-Phase Distributed Model of High-Voltage Windings to Study Internal Steep-Fronted Surge Propagation in a Straightforward Transformer,” *IEEE Transactions on Power Delivery*, vol. 23, no. 4, pp. 2050–2057, Oct. 2008.

[32] A. Demenko, *Obwodowe modele układów z polem elektromagnetycznym*. Wydaw. Politechniki Poznańskiej, 2004.

[33] A. Demenko, R. M. Wojciechowski, and J. K. Sykulski, “2-D Versus 3-D Electromagnetic Field Modeling in Electromechanical Energy Converters,” *IEEE Transactions on Magnetics*, vol. 50, no. 2, pp. 897–900, Feb. 2014.

[34] C. G. Dincan, P. Kjaer, Y.-H. Chen, E. Sarrá-Macia, S. Munk-Nielsen, C. L. Bak, and S. Vaisambhayana, “Design of a High-Power Resonant Converter for DC Wind Turbines,” *IEEE Transactions on Power Electronics*, vol. 34, no. 7, pp. 6136–6154, Jul. 2019.

[35] D. Dolinar, J. Pihler, and B. Grcar, “Dynamic model of a three-phase power transformer,” *IEEE Transactions on Power Delivery*, vol. 8, no. 4, pp. 1811–1819, Oct. 1993.

[36] M. Dolinar, D. Dolinar, G. Stumberger, B. Polajzer, and J. Ritonja, “A Three-Phase Core-Type Transformer Iron Core Model With Included Magnetic Cross Saturation,” *IEEE Transactions on Magnetics*, vol. 42, no. 10, pp. 2849–2851, Oct. 2006.

[37] P. L. Dowell, “Effects of eddy currents in transformer windings,” *Proceedings of the Institution of Electrical Engineers*, vol. 113, no. 8, pp. 1387–1394, Aug. 1966.

[38] Y. Du, S. Lukic, B. Jacobson, and A. Huang, “Review of high power isolated bi-directional DC-DC converters for PHEV/EV DC charging infrastructure,” in *2011 IEEE Energy Conversion Congress and Exposition*, 2011, pp. 553–560.

[39] P. Dworakowski, A. Wilk, and B. Lefebvre, “Hysteresis modelling of a medium frequency single-phase transformer,” in *2017 19th European Conference on Power Electronics and Applications (EPE’17 ECCE Europe)*, 2017, p. P.1-P.9.

[40] P. Dworakowski, A. Wilk, M. Michna, A. Fouineau, and M. Guillet, “Lagrangian model of an isolated dc-dc converter with a 3-phase medium frequency transformer accounting magnetic cross saturation,” *IEEE Transactions on Power Delivery*, accepted for publication.

[41] P. Dworakowski, A. Wilk, M. Michna, B. Lefebvre, and T. Lagier, “3-phase medium frequency transformer for a 100kW 1.2kV 20kHz Dual Active Bridge converter,” in *IECON 2019 - 45th Annual Conference of the IEEE Industrial Electronics Society*, 2019, vol. 1, pp. 4071–4076.

[42] P. Dworakowski, A. Wilk, M. Michna, B. Lefebvre, F. Sixdenier, and M. Mermet-Guyennet, “Effective Permeability of Multi Air Gap Ferrite Core 3-Phase Medium Frequency Transformer in Isolated DC-DC Converters,” *Energies*, vol. 13, no. 6, p. 1352, Jan. 2020.

[43] ebm-papst, “DC axial compact fan 5214 NHH.” [Online]. Available: https://img.ebmpapst.com/products/datasheets/DC-axial-fan-5214NHH-ENU.pdf?_ga=2.136622008.944340178.1582828446-718160680.1582828446. [Accessed: 27-Feb-2020].

[44] A. E. Eiben and J. E. Smith, *Introduction to Evolutionary Computing*. Berlin Heidelberg: Springer-Verlag, 2003.

[45] J. El Hayek and T. J. Sobczyk, “Equivalent circuit of multi-windings traction transformers including magnetizing currents,” in *2005 International Conference on Electrical Machines and Systems*, 2005, vol. 3, pp. 1740-1745 Vol. 3.

[46] EMTP Alliance, “EMTP.” [Online]. Available: https://www.emtp-software.com/en/products/emtp. [Accessed: 07-Mar-2020].

[47] P. Fairley, “DC Versus AC: The Second War of Currents Has Already Begun [In My View],” *IEEE Power and Energy Magazine*, vol. 10, no. 6, pp. 104–103, Nov. 2012.

[48] P. I. Fergestad and T. Henriksen, “Transient Oscillations in Multiwinding Transformers,” *IEEE Transactions on Power Apparatus and Systems*, vol. PAS-93, no. 2, pp. 500–509, Mar. 1974.

[49] Ferroxcube, “Soft ferrites and accessories, data handbook,” 2013. [Online]. Available: https://www.ferroxcube.com/en-global/download/download/11. [Accessed: 01-Jan-2020].

[50] Ferroxcube, “Design of planar power transformers.” [Online]. Available: http://ferroxcube.home.pl/appl/info/plandesi.pdf. [Accessed: 01-Jan-2020].

[51] Ferroxcube, “3C90 material specification,” 2008. [Online]. Available: https://www.ferroxcube.com/upload/media/product/file/MDS/3c90.pdf. [Accessed: 19-Jan-2020].

[52] J. M. Filipe, C. L. Moreira, R. J. Bessa, and B. A. Silva, “Optimization of the variable speed pump storage participation in frequency restoration reserve market,” in *2016 13th International Conference on the European Energy Market (EEM)*, 2016, pp. 1–6.

[53] FLIR, “Thermal camera A325sc.” [Online]. Available: https://www.flir.com/products/a325sc/. [Accessed: 22-Mar-2020].

[54] A. Fouineau, “Méthodologies de Conception de Transformateurs Moyenne Fréquence pour application aux réseaux haute tension et réseaux ferroviaires,” thesis, Lyon, 2019.

[55] A. Fouineau, M.-A. Raulet, B. Lefebvre, N. Burais, and F. Sixdenier, “Semi-Analytical Methods for Calculation of Leakage Inductance and Frequency-Dependent Resistance of Windings in Transformers,” *IEEE Transactions on Magnetics*, vol. 54, no. 10, pp. 1–10, Oct. 2018.

[56] E. F. Fuchs and Y. You, “Measurement of λ-1 characteristics of asymmetric three-phase transformers and their applications,” *IEEE Power Engineering Review*, vol. 22, no. 8, pp. 69–70, Aug. 2002.

[57] A. Garcia-Bediaga, I. Villar, A. Rujas, I. Etxeberria-Otadui, and A. Rufer, “Analytical Models of Multiphase Isolated Medium-Frequency DC–DC Converters,” *IEEE Transactions on Power Electronics*, vol. 32, no. 4, pp. 2508–2520, Apr. 2017.

[58] A. Garcia-Bediaga, I. Villar, A. Rujas, L. Mir, and A. Rufer, “Multiobjective Optimization of Medium-Frequency Transformers for Isolated Soft-Switching Converters Using a Genetic Algorithm,” *IEEE Transactions on Power Electronics*, vol. 32, no. 4, pp. 2995–3006, Apr. 2017.

[59] GE, “DolWin3 HVDC Voltage Source Converters for Efficient Connection of Renewable Energy.” [Online]. Available: http://www.gegridsolutions.com/products/applications/HVDC/HVDC-VSC-Dolwin3-Case-Study-EN-2018-11-Grid-PEA-0578.pdf. [Accessed: 31-Dec-2019].

[60] H. Geramirad, P. Dworakowski, F. Morel, C. Vollaire, B. Lefebvre, P. Camail, and T. Lagier, “Experimental EMI study of a 3-phase 100kW 1200V Dual Active Bridge converter using SiC MOSFETs,” in *EPE’20 ECCE Europe 22nd European Conference on Power Electronics and Applications*, Lyon, France, 2020, accepted for publication.

[61] H. Geramirad, F. Morel, P. Dworakowski, B. Lefebvre, T. Lagier, P. Camail, C. Vollaire, and A. Breard, “Conducted EMI reduction in a 100kW 1.2kV Dual Active Bridge converter,” in *PCIM Europe 2020; International Exhibition and Conference for Power Electronics, Intelligent Motion, Renewable Energy and Energy Management*, Nuremberg, Germany, 2020, accepted for publication.

[62] A. Globus, “Universal hysteresis loop for soft ferromagnetic materials,” in *Proc. European Physical Society Conference on Soft Magnetic Materials*, 1975.

[63] D. Gómez A., J. D. Páez, M. Cheah-Mane, J. Maneiro, P. Dworakowski, O. Gomis-Bellmunt, and F. Morel, “Requirements for interconnection of HVDC links with DC-DC converters,” in *IECON 2019 - 45th Annual Conference of the IEEE Industrial Electronics Society*, 2019, vol. 1, pp. 4854–4860.

[64] T. Guillod, “Modeling and Design of Medium-Frequency Transformers for Future Medium-Voltage Power Electronics Interfaces,” ETH Zurich, 2018.

[65] T. Guillod, J. E. Huber, G. Ortiz, A. De, C. M. Franck, and J. W. Kolar, “Characterization of the voltage and electric field stresses in multi-cell solid-state transformers,” in *2014 IEEE Energy Conversion Congress and Exposition (ECCE)*, 2014, pp. 4726–4734.

[66] J. Gyselinck, P. Dular, N. Sadowski, J. V. Leite, and J. P. A. Bastos, “Incorporation of a Jiles-Atherton vector hysteresis model in 2D FE magnetic field computations: Application of the Newton-Raphson method,” *COMPEL: The International Journal for Computation and Mathematics in Electrical and Electronic Engineering*, vol. 23, pp. 685–693, Sep. 2004.

[67] J. Gyselinck and J. Melkebeek, “Two-dimensional finite element modelling of overlap joints in transformer cores,” *COMPEL - The international journal for computation and mathematics in electrical and electronic engineering*, vol. 20, no. 1, pp. 253–268, Jan. 2001.

[68] A. Hauck, M. Ertl, J. Schöberl, and M. Kaltenbacher, “Accurate magnetostatic simulation of step-lap joints in transformer cores using anisotropic higher order FEM,” *COMPEL: The International Journal for Computation and Mathematics in Electrical and Electronic Engineering*, vol. 32, no. 5, pp. 1581–1595, Jan. 2013.

[69] L. Heinemann, “An actively cooled high power, high frequency transformer with high insulation capability,” in *APEC. Seventeenth Annual IEEE Applied Power Electronics Conference and Exposition (Cat. No.02CH37335)*, 2002, vol. 1, pp. 352–357 vol.1.

[70] N. Hihat, E. Napieralska-Juszczak, J.-P. Lecointe, J. K. Sykulski, and K. Komeza, “Equivalent Permeability of Step-Lap Joints of Transformer Cores: Computational and Experimental Considerations,” *IEEE Transactions on Magnetics*, vol. 47, no. 1, pp. 244–251, Jan. 2011.

[71] K. Hollaus and M. Schöbinger, “Multiscale finite element method for perturbation of laminated structures,” in *2017 International Conference on Electromagnetics in Advanced Applications (ICEAA)*, 2017, pp. 1262–1263.

[72] C. Huang, F. Woittennek, and K. Röbenack, “Distributed parameter model of the buck converter with constant inductive load,” *IFAC-PapersOnLine*, vol. 48, no. 1, pp. 691–692, Jan. 2015.

[73] P. Huang, C. Mao, D. Wang, L. Wang, Y. Duan, J. Qiu, G. Xu, and H. Cai, “Optimal Design and Implementation of High-Voltage High-Power Silicon Steel Core Medium-Frequency Transformer,” *IEEE Transactions on Industrial Electronics*, vol. 64, no. 6, pp. 4391–4401, Jun. 2017.

[74] W. G. Hurley, T. Merkin, and M. Duffy, “The Performance Factor for Magnetic Materials Revisited: The Effect of Core Losses on the Selection of Core Size in Transformers,” *IEEE Power Electronics Magazine*, vol. 5, no. 3, pp. 26–34, Sep. 2018.

[75] W. G. Hurley and W. H. Wölfle, Transformers and Inductors for Power Electronics: Theory, Design and Applications. Wiley, 2013.

[76] N. Ida and J. P. A. Bastos, “Electrostatic Fields,” in *Electromagnetics and Calculation of Fields*, N. Ida, J. P. A. Bastos, and R. Mittra, Eds. New York, NY: Springer US, 1992, pp. 47–89.

[77] Infineon, “High Power Thyristors & Diodes Selection Guide 2019/2020,” 2019. [Online]. Available: https://www.infineon.com/dgdl?fileId=5546d4625a888733015aad13f7a04835. [Accessed: 01-Jan-2020].

[78] Infineon, “IGBT Modules.” [Online]. Available: https://www.infineon.com/cms/en/product/power/igbt/igbt-modules/. [Accessed: 01-Jan-2020].

[79] A. Ivani, J. Fuzi, and Z. Szabo, “Preisach models of ferromagnetic hysteresis,” *Przeglad Elektrotechniczny*, vol. R. LXXIX 3/2003, pp. 145–150, 2003.

[80] J. Jacobs, M. Thommes, and R. De Doncker, “A transformer comparison for three-phase single active bridges,” in *2005 European Conference on Power Electronics and Applications*, 2005, pp. 10 pp.-P.10.

[81] C. Jedryczka, P. Sujka, and W. Szelag, “The influence of magnetic hysteresis on magnetorheological fluid clutch operation,” *COMPEL: The International Journal for Computation and Mathematics in Electrical and Electronic Engineering*, vol. 28, pp. 711–721, May 2009.

[82] M. Jesenik, M. Beković, A. Hamler, and M. Trlep, “Analytical modelling of a magnetization curve obtained by the measurements of magnetic materials’ properties using evolutionary algorithms,” *Applied Soft Computing*, vol. 52, pp. 387–408, Mar. 2017.

[83] E. Jezierski, *Transformatory*. Warszawa: WNT, 1983.

[84] D. Jiles and D. Atherton, “Ferromagnetic hysteresis,” *IEEE Transactions on Magnetics*, vol. 19, no. 5, pp. 2183–2185, Sep. 1983.

[85] M. Kabalo, B. Blunier, D. Bouquain, and A. Miraoui, “State-of-the-art of DC-DC converters for fuel cell vehicles,” in *2010 IEEE Vehicle Power and Propulsion Conference*, 2010, pp. 1–6.

[86] M. Kachniarz, J. Salach, R. Szewczyk, and A. Bieńkowski, “Temperature Influence on the Magnetic Characteristics of Mn-Zn Ferrite Materials,” in *Progress in Automation, Robotics and Measuring Techniques*, Cham, 2015, pp. 121–127.

[87] G. Kadar and E. Torre, “Hysteresis modeling: I. Non-congruency,” *IEEE Transactions on Magnetics*, vol. 23, no. 5, pp. 2820–2822, Sep. 1987.

[88] A. Kazerooni, G. De Carne, M. Andersen, M. Liserre, M. Eves, and J. Yu, “Technical requirements of Smart Transformer for Deployment in Grid Application,” in *CIRED 2019 Conference*, Madrid, Spain, 2019.

[89] A. Keyhani, S. W. Chua, and S. A. Sebo, “Maximum likelihood estimation of transformer high frequency parameters from test data,” *IEEE Transactions on Power Delivery*, vol. 6, no. 2, pp. 858–865, Apr. 1991.

[90] M. H. Kheraluwala, D. W. Novotny, and D. M. Divan, “Coaxially wound transformers for high-power high-frequency applications,” *IEEE Transactions on Power Electronics*, vol. 7, no. 1, pp. 54–62, Jan. 1992.

[91] L. Knypinski, L. Nowak, P. Sujka, and K. Radziuk, “Application of a PSO algorithm for identification of the parameters of Jiles-Atherton hysteresis model,” *Archives of Electrical Engineering*, vol. 61, pp. 1–2, Jan. 2011.

[92] M. A. Krasnosel’skii and A. V. Pokrovskii, *Systems with Hysteresis*. Berlin Heidelberg: Springer-Verlag, 1989.

[93] P. A. Kyaw, J. Qiu, and C. R. Sullivan, “Analytical Thermal Model for Inductor and Transformer Windings and Litz Wire,” in *2018 IEEE 19th Workshop on Control and Modeling for Power Electronics (COMPEL)*, 2018, pp. 1–9.

[94] T. Lagier, “Convertisseurs continu-continu pour les réseaux d’électricité à courant continu,” thesis, Toulouse, INPT, 2016.

[95] T. Lagier, L. Chédot, L. Ghossein, F. Wallart, B. Lefebvre, P. Dworakowski, M. Mermet-Guyennet, and C. Buttay, “A 100 kW 1.2 kV 20 kHz DC-DC converter prototype based on the Dual Active Bridge topology,” in *2018 IEEE International Conference on Industrial Technology (ICIT)*, 2018, pp. 559–564.

[96] T. Lagier, P. Dworakowski, C. Buttay, P. Ladoux, A. Wilk, P. Camail, and E. Anak, “Experimental validation and comparison of a SiC MOSFET based 100 kW 1.2 kV 20 kHz three-phase dual active bridge converter using two vector groups,” in *EPE’20 ECCE Europe 22nd European Conference on Power Electronics and Applications*, Lyon, France, 2020, accepted for publication.

[97] T. Lagier and P. Ladoux, “Method of Controlling a Dual-Bridge Dc/Dc Converter,” EP3449555 (A1).

[98] T. Lagier and P. Ladoux, “Theoretical and experimental analysis of the soft switching process for SiC MOSFETs based Dual Active Bridge converters,” in *2018 International Symposium on Power Electronics, Electrical Drives, Automation and Motion (SPEEDAM)*, 2018, pp. 262–267.

[99] T. Lagier, P. Ladoux, and P. Dworakowski, “Potential of silicon carbide MOSFETs in the DC/DC converters for future HVDC offshore wind farms,” *High Voltage*, vol. 2, no. 4, pp. 233–243, 2017.

[100] J. F. Lazar and R. Martinelli, “Steady-state analysis of the LLC series resonant converter,” in *APEC 2001. Sixteenth Annual IEEE Applied Power Electronics Conference and Exposition (Cat. No.01CH37181)*, 2001, vol. 2, pp. 728–735 vol.2.

[101] Y. Lee, G. Vakil, Alan. J. Watson, and P. W. Wheeler, “Geometry optimization and characterization of three-phase medium frequency transformer for 10kVA Isolated DC-DC converter,” in *2017 IEEE Energy Conversion Congress and Exposition (ECCE)*, 2017, pp. 511–518.

[102] M. Leibl, G. Ortiz, and J. W. Kolar, “Design and Experimental Analysis of a Medium-Frequency Transformer for Solid-State Transformer Applications,” *IEEE Journal of Emerging and Selected Topics in Power Electronics*, vol. 5, no. 1, pp. 110–123, Mar. 2017.

[103] F. de Leon and A. Semlyen, “Reduced order model for transformer transients,” *IEEE Transactions on Power Delivery*, vol. 7, no. 1, pp. 361–369, Jan. 1992.

[104] A. Lesnicar and R. Marquardt, “An innovative modular multilevel converter topology suitable for a wide power range,” in *2003 IEEE Bologna Power Tech Conference Proceedings,* 2003, vol. 3, pp. 6 pp. Vol.3-.

[105] T. J. Lewis, “The transient behaviour of ladder networks of the type representing transformer and machine windings,” *Journal of the Institution of Electrical Engineers*, vol. 1954, no. 10, pp. 278–280, Oct. 1954.

[106] D. Lin, P. Zhou, and A. Bergqvist, “Improved Vector Play Model and Parameter Identification for Magnetic Hysteresis Materials,” *IEEE Transactions on Magnetics*, vol. 50, no. 2, pp. 357–360, Feb. 2014.

[107] F. Liorzou, B. Phelps, and D. L. Atherton, “Macroscopic models of magnetization,” *IEEE Transactions on Magnetics*, vol. 36, no. 2, pp. 418–428, Mar. 2000.

[108] C. Liu, L. Qi, X. Cui, and X. Wei, “Experimental Extraction of Parasitic Capacitances for High-Frequency Transformers,” *IEEE Transactions on Power Electronics*, vol. 32, no. 6, pp. 4157–4167, Jun. 2017.

[109] H. Y. Lu, J. G. Zhu, and S. Y. R. Hui, “Measurement and Modeling of Thermal Effects on Magnetic Hysteresis of Soft Ferrites,” *IEEE Transactions on Magnetics*, vol. 43, no. 11, pp. 3952–3960, Nov. 2007.

[110] M. Luo, D. Dujic, and J. Allmeling, “Modeling Frequency Independent Hysteresis Effects of Ferrite Core Materials Using Permeance–Capacitance Analogy for System-Level Circuit Simulations,” *IEEE Transactions on Power Electronics*, vol. 33, no. 12, pp. 10055–10070, Dec. 2018.

[111] M. V. F. da Luz, P. Dular, J. V. Leite, and P. Kuo-Peng, “Modeling of Transformer Core Joints via a Subproblem FEM and a Homogenization Technique,” *IEEE Transactions on Magnetics*, vol. 50, no. 2, pp. 1009–1012, Feb. 2014.

[112] W. Lyskawinski, P. Sujka, W. Szelag, and M. Baranski, “Numerical analysis of hysteresis loss in pulse transformer,” *Archives of Electrical Engineering*, vol. 60, Jun. 2011.

[113] Manitoba Hydro International, “PSCAD.” [Online]. Available: https://www.pscad.com/software/pscad/overview. [Accessed: 07-Mar-2020].

[114] Mathworks, “Simulink Real-Time.” [Online]. Available: https://fr.mathworks.com/products/simulink-real-time.html. [Accessed: 06-Mar-2020].

[115] Mathworks, “Simscape saturable transformer with hysteresis.” [Online]. Available: https://fr.mathworks.com/help/physmod/sps/powersys/ref/saturabletransformer.html. [Accessed: 06-Mar-2020].

[116] S. F. Mauser and T. E. McDermott, “Electromagnetic Transients Program (EMTP): Application guide: Final report,” Westinghouse Electric Corp., Pittsburgh, PA (USA). Power System Engineering Dept.; Electric Power Research Inst., Palo Alto, CA (USA), EPRI-EL-4650, Nov. 1986.

[117] I. Mayergoyz, “Mathematical models of hysteresis,” *IEEE Transactions on Magnetics*, vol. 22, no. 5, pp. 603–608, Sep. 1986.

[118] I. D. Mayergoyz and A. A. Adly, “Numerical implementation of the feedback Preisach model,” *IEEE Transactions on Magnetics*, vol. 28, no. 5, pp. 2605–2607, Sep. 1992.

[119] K. Meah and S. Ula, “Comparative Evaluation of HVDC and HVAC Transmission Systems,” in *2007 IEEE Power Engineering Society General Meeting*, 2007, pp. 1–5.

[120] J. Meisel, Principles of electromechanical-energy conversion. McGraw-Hill, 1966.

[121] M. Michna, P. Dworakowski, A. Wilk, F. Kutt, and M. Mermet-Guyennet, “Modified Preisach model of hysteresis in multi air gap ferrite core medium frequency transformer,” *Energies*, submitted for publication.

[122] M. Michna, A. Wilk, P. Dworakowski, and B. Lefebvre, “Determination of Mathematical Model Parameters of a Medium Frequency Transformer,” in *2018 International Symposium on Electrical Machines (SME)*, 2018, pp. 1–5.

[123] J. Millán, P. Godignon, X. Perpiñà, A. Pérez-Tomás, and J. Rebollo, “A Survey of Wide Bandgap Power Semiconductor Devices,” *IEEE Transactions on Power Electronics*, vol. 29, no. 5, pp. 2155–2163, May 2014.

[124] M. Mogorovic and D. Dujic, “100 kW, 10 kHz Medium-Frequency Transformer Design Optimization and Experimental Verification,” *IEEE Transactions on Power Electronics*, vol. 34, no. 2, pp. 1696–1708, Feb. 2019.

[125] A. Morched, L. Marti, and J. Ottevangers, “A high frequency transformer model for the EMTP,” *IEEE Transactions on Power Delivery*, vol. 8, no. 3, pp. 1615–1626, Jul. 1993.

[126] J. J. Moré, “The Levenberg-Marquardt algorithm: Implementation and theory,” in *Numerical Analysis*, Berlin, Heidelberg, 1978, pp. 105–116.

[127] B. A. Mork, F. Gonzalez, D. Ishchenko, D. L. Stuehm, and J. Mitra, “Hybrid Transformer Model for Transient Simulation—Part I: Development and Parameters,” *IEEE Transactions on Power Delivery*, vol. 22, no. 1, pp. 248–255, Jan. 2007.

[128] B. A. Mork, F. Gonzalez, D. Ishchenko, D. L. Stuehm, and J. Mitra, “Hybrid Transformer Model for Transient Simulation—Part II: Laboratory Measurements and Benchmarking,” *IEEE Transactions on Power Delivery*, vol. 22, no. 1, pp. 256–262, Jan. 2007.

[129] L. H. Mweene, C. A. Wright, and M. F. Schlecht, “A 1 kW 500 kHz front-end converter for a distributed power supply system,” *IEEE Transactions on Power Electronics*, vol. 6, no. 3, pp. 398–407, Jul. 1991.

[130] A. Nabae, I. Takahashi, and H. Akagi, “A New Neutral-Point-Clamped PWM Inverter,” *IEEE Transactions on Industry Applications*, vol. IA-17, no. 5, pp. 518–523, Sep. 1981.

[131] T. Nakata, N. Takahashi, and Y. Kawase, “Magnetic performance of step-lap joints in distribution transformer cores,” *IEEE Transactions on Magnetics*, vol. 18, no. 6, pp. 1055–1057, Nov. 1982.

[132] M. Noah, S. Kimura, S. Endo, M. Yamamoto, J. Imaoka, K. Umetani, and W. Martinez, “A novel three-phase LLC resonant converter with integrated magnetics for lower turn-off losses and higher power density,” in *2017 IEEE Applied Power Electronics Conference and Exposition (APEC)*, 2017, pp. 322–329.

[133] M. Noah, K. Umetani, J. Imaoka, and M. Yamamoto, “Lagrangian dynamics model and practical implementation of an integrated transformer in multi-phase LLC resonant converter,” *IET Power Electronics*, vol. 11, no. 2, pp. 339–347, 2018.

[134] S. Okabe, M. Koto, G. Ueta, T. Saida, and S. Yamada, “Development of high frequency circuit model for oil-immersed power transformers and its application for lightning surge analysis,” *IEEE Transactions on Dielectrics and Electrical Insulation*, vol. 18, no. 2, pp. 541–552, Apr. 2011.

[135] G. Ortiz, J. Biela, D. Bortis, and J. W. Kolar, “1 Megawatt, 20 kHz, isolated, bidirectional 12kV to 1.2kV DC-DC converter for renewable energy applications,” in *The 2010 International Power Electronics Conference - ECCE ASIA -*, 2010, pp. 3212–3219.

[136] G. Ortiz, J. Biela, and J. W. Kolar, “Optimized design of medium frequency transformers with high isolation requirements,” in *IECON 2010 - 36th Annual Conference on IEEE Industrial Electronics Society*, 2010, pp. 631–638.

[137] J. D. Páez, D. Frey, J. Maneiro, S. Bacha, and P. Dworakowski, “Overview of DC–DC Converters Dedicated to HVdc Grids,” *IEEE Transactions on Power Delivery*, vol. 34, no. 1, pp. 119–128, Feb. 2019.

[138] Pan-Seok Shin and Jinhee Lee, “Magnetic field analysis of amorphous core transformer using homogenization technique,” *IEEE Transactions on Magnetics*, vol. 33, no. 2, pp. 1808–1811, Mar. 1997.

[139] A. M. Pereira, “Conception de Transformateurs Moyennes Fréquences : application aux convertisseurs DC-DC haute tension et forte puissance,” thesis, Lyon, 2016.

[140] A. Pereira, F. Sixdenier, M. A. Raulet, B. Lefebvre, and N. Burais, “Comparison Between Numerical and Analytical Methods of AC Resistance Evaluation for Medium-Frequency Transformers: Validation on a Prototype and Thermal Impact Analysis,” *Canadian Journal of Electrical and Computer Engineering*, vol. 40, no. 2, pp. 101–109, Spring 2017.

[141] M. Pietruszka and E. Napieralska-Juszczak, “Lamination of T-joints in the transformer core,” *IEEE Transactions on Magnetics*, vol. 32, no. 3, pp. 1180–1183, May 1996.

[142] A. M. Plamitzer, *Maszyny elektryczne*. Wydawnictwa Naukowo-Techniczne, 1972.

[143] F. Preisach, “Über die magnetische Nachwirkung,” *Z. Physik*, vol. 94, no. 5, pp. 277–302, May 1935.

[144] C. Ragusa, “An analytical method for the identification of the Preisach distribution function,” *Journal of Magnetism and Magnetic Materials*, vol. 254–255, pp. 259–261, Jan. 2003.

[145] W. A. Roshen, “Fringing Field Formulas and Winding Loss Due to an Air Gap,” *IEEE Transactions on Magnetics*, vol. 43, no. 8, pp. 3387–3394, Aug. 2007.

[146] D. Rothmund, T. Guillod, D. Bortis, and J. W. Kolar, “99% Efficient 10 kV SiC-Based 7 kV/400 V DC Transformer for Future Data Centers,” *IEEE Journal of Emerging and Selected Topics in Power Electronics*, vol. 7, no. 2, pp. 753–767, Jun. 2019.

[147] R. Rudenberg, “Performance of traveling waves in coils and windings,” *Electrical Engineering*, vol. 59, no. 12, pp. 1031–1040, Dec. 1940.

[148] R. Ryndzionek and Ł. Sienkiewicz, “Evolution of the HVDC Link Connecting Offshore Wind Farms to Onshore Power Systems,” *Energies*, vol. 13, no. 8, p. 1914, Jan. 2020.

[149] A. Schoppa, J. Schneider, C.-D. Wuppermann, and T. Bakon, “Influence of welding and sticking of laminations on the magnetic properties of non-oriented electrical steels,” *Journal of Magnetism and Magnetic Materials*, vol. 254–255, pp. 367–369, Jan. 2003.

[150] F. C. Schwarz and J. B. Klaassens, “A Controllable 45-kW Current Source for DC Machines,” *IEEE Transactions on Industry Applications*, vol. IA-15, no. 4, pp. 437–444, Jul. 1979.

[151] R. Sellick, M. Agamy, L. Hao, and K. Weeber, “A high-speed HVDC breaker topology with integral voltage-changing capability,” in *2015 IEEE Electrical Insulation Conference (EIC)*, 2015, pp. 123–126.

[152] X. She, A. Q. Huang, and R. Burgos, “Review of Solid-State Transformer Technologies and Their Application in Power Distribution Systems,” *IEEE Journal of Emerging and Selected Topics in Power Electronics*, vol. 1, no. 3, pp. 186–198, Sep. 2013.

[153] Y. Shibuya and S. Fujita, “High frequency model and transient response of transformer windings,” in *IEEE/PES Transmission and Distribution Conference and Exhibition*, 2002, vol. 3, pp. 1839–1844 vol.3.

[154] A. Shintemirov, W. H. Tang, and Q. H. Wu, “A Hybrid Winding Model of Disc-Type Power Transformers for Frequency Response Analysis,” *IEEE Transactions on Power Delivery*, vol. 24, no. 2, pp. 730–739, Apr. 2009.

[155] P. Shuai and J. Biela, “Design and optimization of medium frequency, medium voltage transformers,” in *2013 15th European Conference on Power Electronics and Applications (EPE)*, 2013, pp. 1–10.

[156] Siemens, “MVDC PLUS® – the grid connector,” *siemens.com Global Website*. [Online]. Available: https://new.siemens.com/global/en/products/energy/medium-voltage/solutions/mvdc.html. [Accessed: 30-Dec-2019].

[157] G. R. Slemon, “Equivalent circuits for transformers and machines including non-linear effects,” *Proceedings of the IEE - Part IV: Institution Monographs*, vol. 100, no. 5, pp. 129–143, Oct. 1953.

[158] N. Soltau, H. Stagge, R. W. De Doncker, and O. Apeldoorn, “Development and demonstration of a medium-voltage high-power DC-DC converter for DC distribution systems,” in *2014 IEEE 5th International Symposium on Power Electronics for Distributed Generation Systems (PEDG)*, 2014, pp. 1–8.

[159] SP Energy Networks, “LV Engine - a smarter electricity network,” 2018. [Online]. Available: https://www.spenergynetworks.co.uk/userfiles/file/LV_Engine_Smarter_Network.pdf. [Accessed: 28-Feb-2020].

[160] Speedgoat, “Simulink real-time-target performance computer.” [Online]. Available: https://www.speedgoat.com/products-services/real-time-target-machines/performance. [Accessed: 06-Mar-2020].

[161] C. Stackler, F. Morel, P. Ladoux, and P. Dworakowski, “25 kV–50 Hz railway supply modelling for medium frequencies (0–5 kHz),” in *2016 International Conference on Electrical Systems for Aircraft, Railway, Ship Propulsion and Road Vehicles International Transportation Electrification Conference (ESARS-ITEC)*, 2016, pp. 1–6.

[162] C. Stackler, F. Morel, P. Ladoux, A. Fouineau, F. Wallart, and N. Evans, “Optimal sizing of a power electronic traction transformer for railway applications,” in *IECON 2018 - 44th Annual Conference of the IEEE Industrial Electronics Society*, 2018, pp. 1380–1387.

[163] Chas. P. Steinmetz, “On the Law of Hysteresis,” *Transactions of the American Institute of Electrical Engineers*, vol. IX, no. 1, pp. 1–64, Jan. 1892.

[164] M. Stojadinović and J. Biela, “Modelling and Design of a Medium Frequency Transformer for High Power DC-DC Converters,” in *2018 International Power Electronics Conference (IPEC-Niigata 2018 -ECCE Asia)*, 2018, pp. 1103–1110.

[165] E. C. Stoner and E. P. Wohlfarth, “A mechanism of magnetic hysteresis in heterogeneous alloys,” *Philosophical Transactions of the Royal Society of London. Series A, Mathematical and Physical Sciences*, vol. 240, no. 826, pp. 599–642, May 1948.

[166] G. Stumberger, B. Polajzer, B. Stumberger, M. Toman, and D. Dolinar, “Evaluation of experimental methods for determining the magnetically nonlinear characteristics of electromagnetic devices,” *IEEE Transactions on Magnetics*, vol. 41, no. 10, pp. 4030–4032, Oct. 2005.

[167] Q. Su, R. E. James, and D. Sutanto, “A Z-transform model of transformers for the study of electromagnetic transients in power systems,” *IEEE Transactions on Power Systems*, vol. 5, no. 1, pp. 27–33, Feb. 1990.

[168] Tektronix, “5 Series MSO Mixed Signal Oscilloscope.” [Online]. Available: https://www.tek.com/oscilloscope/5-series-mso-mixed-signal-oscilloscope. [Accessed: 15-Mar-2020].

[169] J. Tellinen, “A simple scalar model for magnetic hysteresis,” *IEEE Transactions on Magnetics*, vol. 34, no. 4, pp. 2200–2206, Jul. 1998.

[170] B. Tellini, R. Giannetti, G. Robles, and S. Lizon-Martinez, “New method to characterize magnetic hysteresis in soft ferrites up to high frequencies,” *IEEE Transactions on Instrumentation and Measurement*, vol. 55, no. 1, pp. 311–315, Feb. 2006.

[171] G. J. Thaler and M. L. Wilcox, *Electric machines: dynamics and steady state*. Wiley, 1966.

[172] B. Z. Tomczuk, D. Koteras, and A. Waindok, “Electromagnetic and Temperature 3-D Fields for the Modular Transformers Heating Under High-Frequency Operation,” *IEEE Transactions on Magnetics*, vol. 50, no. 2, pp. 317–320, Feb. 2014.

[173] F. Tourkhani and P. Viarouge, “Accurate analytical model of winding losses in round Litz wire windings,” *IEEE Transactions on Magnetics*, vol. 37, no. 1, pp. 538–543, Jan. 2001.

[174] J. Turowski, M. Turowski, and M. Kopec, “Method of three-dimensional network solution of leakage field of three-phase transformers,” *IEEE Transactions on Magnetics*, vol. 26, no. 5, pp. 2911–2919, Sep. 1990.

[175] K. Umetani, “A generalized method for Lagrangian modeling of power conversion circuit with integrated magnetic components,” *IEEJ Transactions on Electrical and Electronic Engineering*, vol. 7, no. S1, pp. S146–S152, 2012.

[176] P. T. M. Vaessen, “Transformer model for high frequencies,” *IEEE Transactions on Power Delivery*, vol. 3, no. 4, pp. 1761–1768, Oct. 1988.

[177] P. Vas, K. E. Hallenius, and J. E. Brown, “Cross-Saturation in Smooth-Air-Gap Electrical Machines,” *IEEE Transactions on Energy Conversion*, vol. EC-1, no. 1, pp. 103–112, Mar. 1986.

[178] K. Venkatachalam, C. R. Sullivan, T. Abdallah, and H. Tacca, “Accurate prediction of ferrite core loss with nonsinusoidal waveforms using only Steinmetz parameters,” in *2002 IEEE Workshop on Computers in Power Electronics, 2002. Proceedings.*, 2002, pp. 36–41.

[179] I. Villar, A. Garcia-Bediaga, U. Viscarret, I. Etxeberria-Otadui, and A. Rufer, “Proposal and validation of medium-frequency power transformer design methodology,” in *2011 IEEE Energy Conversion Congress and Exposition*, 2011, pp. 3792–3799.

[180] I. Villar, L. Mir, I. Etxeberria-Otadui, J. Colmenero, X. Agirre, and T. Nieva, “Optimal design and experimental validation of a Medium-Frequency 400kVA power transformer for railway traction applications,” in *2012 IEEE Energy Conversion Congress and Exposition (ECCE)*, 2012, pp. 684–690.

[181] G. R. Walker and P. C. Sernia, “Cascaded DC-DC converter connection of photovoltaic modules,” *IEEE Transactions on Power Electronics*, vol. 19, no. 4, pp. 1130–1139, Jul. 2004.

[182] M. Wattenberg, U. Schwalbe, and M. Pfost, “Impact of DC-Bias on Dual Active Bridge Control and How to Avoid it,” in *2019 21st European Conference on Power Electronics and Applications (EPE ’19 ECCE Europe)*, 2019, p. P.1-P.8.

[183] Wayne Kerr Electronics, “6500B Series Impedance Analyzer.” [Online]. Available: http://www.waynekerrtest.com/products_detail.php?indexs=4. [Accessed: 06-Mar-2020].

[184] D. C. White and H. H. Woodson, *Electromechanical Energy Conversion*. Wiley, 1959.

[185] A. Wilk, “Representation of magnetic hysteresis in a circuit model of a single-phase transformer,” *COMPEL - The international journal for computation and mathematics in electrical and electronic engineering*, vol. 34, pp. 778–791, May 2015.

[186] A. Wilk, Modelowanie obwodowo-polowe transformatorów trakcyjnych w aspekcie diagnostyki opartej na modelu referencyjnym. Politechnika Gdańska, 2012.

[187] A. Wilk, M. Michna, P. Dworakowski, and B. Lefebvre, “Influence of air gap size on magnetizing current and power losses in ferrite core transformers - experimental investigations,” in *EPNC 2018 Twenty-fifth Symposium on Electromagnetic Phenomena in Nonlinear Circuits*, Arras, France, 2018.

[188] A. Wilk, J. Nieznanski, I. Moson, P. Dobrowolski, and G. Kostro, “Nonlinear equivalent circuit model of a traction transformer for winding internal fault diagnostic purposes,” in *2008 18th International Conference on Electrical Machines*, 2008, pp. 1–5.

[189] R. M. Wojciechowski, A. Demenko, and J. K. Sykulski, “Inducted currents analysis in multiply connected conductors using reluctance-resistance networks,” *COMPEL - The international journal for computation and mathematics in electrical and electronic engineering*, vol. 29, no. 4, pp. 908–918, Jan. 2010.

[190] Wolfspeed, “CAS300M17BM2 1700V 225A 8.0mΩ SiC Half-Bridge.” [Online]. Available: https://www.wolfspeed.com/power/products/sic-power-modules/cas300m17bm2. [Accessed: 01-Jan-2020].

[191] Wolfspeed, “SiC Custom Power Services,” 2017. [Online]. Available: https://www.wolfspeed.com/downloads/dl/file/id/867/product/0/custom_power_services_overview.pdf. [Accessed: 01-Jan-2020].

[192] Q. Wu, T. Hong, S. Jazebi, and F. de León, “Experimentally Validated Method to Measure the lambda-i Characteristics of Asymmetric Three-Phase Transformers,” *IEEE Transactions on Magnetics*, vol. 55, no. 4, pp. 1–9, Apr. 2019.

[193] Q. Wu, S. Jazebi, and F. de Leon, “Parameter Estimation of Three-Phase Transformer Models for Low-Frequency Transient Studies From Terminal Measurements,” *IEEE Transactions on Magnetics*, vol. 53, no. 7, pp. 1–8, Jul. 2017.

[194] G. Xue, P. Zhang, Z. He, D. Li, Z. Yang, and Z. Zhao, “Modification and Numerical Method for the Jiles-Atherton Hysteresis Model,” *Communications in Computational Physics*, vol. 21, no. 3, pp. 763–781, Mar. 2017.

[195] J. Xue, F. Wang, D. Boroyevich, and Z. Shen, “Single-phase vs. three-phase high density power transformers,” in *2010 IEEE Energy Conversion Congress and Exposition*, 2010, pp. 4368–4375.

[196] M. Yilmaz and P. T. Krein, “Review of benefits and challenges of vehicle-to-grid technology,” in *2012 IEEE Energy Conversion Congress and Exposition (ECCE)*, 2012, pp. 3082–3089.

[197] Yokogawa, “WT1800E High-Performance Power Analyzer.” [Online]. Available: https://tmi.yokogawa.com/fr/solutions/products/power-analyzers/wt1800e-high-performance-power-analyzer/. [Accessed: 08-Mar-2020].

[198] J. Yu, K. Smith, M. Urizarbarrena, N. MacLeod, R. Bryans, and A. Moon, “Initial designs for the ANGLE DC project; converting existing AC cable and overhead line into DC operation,” in *13th IET International Conference on AC and DC Power Transmission (ACDC 2017)*, 2017, pp. 1–6.

[199] K. Zakrzewski and M. Lukaniszyn, “Three-dimensional model of one- and three-phase transformer for leakage field calculation,” *IEEE Transactions on Magnetics*, vol. 28, no. 2, pp. 1344–1347, Mar. 1992.

[200] K. Zakrzewski, B. Tomczuk, and D. Koteras, “Simulation of forces and 3-D field arising during power autotransformer fault due to electric arc in HV winding,” *IEEE Transactions on Magnetics*, vol. 38, no. 2, pp. 1153–1156, Mar. 2002.

[201] ZES Zimmer, “LMG670 - 1 to 7 Channel Power Analyzer.” [Online]. Available: https://www.zes.com/en/Products/Discontinued-Products/Energy-and-Power-Meters/LMG670. [Accessed: 06-Mar-2020].

[202] C. Zhao, M. Weiss, A. Mester, S. Lewdeni-Schmid, D. Dujic, J. K. Steinke, and T. Chaudhuri, “Power electronic transformer (PET) converter: Design of a 1.2MW demonstrator for traction applications,” in *Automation and Motion International Symposium on Power Electronics Power Electronics, Electrical Drives*, 2012, pp. 855–860.

[203] Z. Zhao, F. Liu, Z. Cheng, W. Yan, L. Liu, J. Zhang, and Y. Fan, “Measurements and Calculation of Core-Based $B-H$ Curve and Magnetizing Current in DC-Biased Transformers,” *IEEE Transactions on Applied Superconductivity*, vol. 20, no. 3, pp. 1131–1134, Jun. 2010.

[204] “ELIPTIC project.” [Online]. Available: https://www.eliptic-project.eu/. [Accessed: 10-Mar-2020].

[205] “393-1991 - IEEE Standard for Test Procedures for Magnetic Cores.” IEEE SA, 1992.

[206] “IEC 60404-2:1996 Magnetic materials - Part 2: Methods of measurement of the magnetic properties of electrical steel sheet and strip by means of an Epstein frame.” 1996.

[207] “IEC 60404-3:1992 Magnetic materials - Part 3: Methods of measurement of the magnetic properties of magnetic sheet and strip by means of a single sheet tester.” 1992.

[208] “IEC 60404-10:2016 Magnetic materials - Part 10: Methods of measurement of magnetic properties of electrical steel strip and sheet at medium frequencies.” 2016.

[209] “IEC 60404-6:2003 Magnetic materials - Part 6: Methods of measurement of the magnetic properties of magnetically soft metallic and powder materials at frequencies in the range 20 Hz to 200 kHz by the use of ring specimens.” 2003.

[210] “IEC 62044 Cores made of soft magnetic materials - Measuring methods.” 2002.

# Appendices

## Appendix 1. Model implementation

The model developed in chapter 3 and used in the analysis presented in §6.3 was implemented in a Matlab script including the following m-files:

- DAB3_solver.m - based on Matlab differential equation solver ode15s which enables the variable and singular mass matrix (Listing A1); ode15s is a variable-order numerical differentiation formula (NDF) based solver,
- DAB3_param.m - model parameters (Listing A2),
- DAB3_model.m - right hand side of the differential equation (Listing A3),
- DAB3_model_Msys.m - mass matrix of the differential equation, matrix of inductances (Listing A4),
- DAB3_model_Fsys.m - matrix of voltages (Listing A5),
- DAB3_square.m - VSC voltage waveform generator (Listing A6),
- DAB3_model_Rsys.m - matrix of resistances (Listing A7).

The listings presented hereafter give the selected parts of the code.

Listing A1. DAB3_solver.m

```
DAB3_param;

y0(1,1) = 0;
y0(2,1) = 0;
y0(3,1) = 0;
y0(4,1) = 0;
y0(5,1) = 0;
y0(6,1) = 0;

options = odeset('Mass', @DAB3_model_Msys, 'NormControl', 'on','OutputFcn', @odeplot,
'RelTol', 1e-5, 'AbsTol',1e-5, 'MaxStep', 1e-7);

[t,y] = ode15s(@DAB3_model,tspan,y0,options);
```

Listing A2. DAB3_param.m

```
LfM = 1; % cross coupling leakage inductance gain
LmNL = 1; % nonlinear magnetizing inductance gain
LmM = 1; % cross coupling magnetizing inductance gain
```

Listing A3. DAB3_model.m

```
function dy = DAB3_model(t,y)
    dy = DAB3_model_Fsys(t,y) - DAB3_model_Rsys(t,y)*y;
end
```

Listing A4. DAB3_model_Msys.m

```
function Mx = DAB3_model_Msys(t,y)
    DAB3_param;

    Theta(1) = y(1)*Np;
    Theta(2) = y(2)*Np;
    Theta(3) = y(3)*Ns;
    Theta(4) = y(4)*Ns;
    Theta(5) = y(5)*Ne;
    Theta(6) = y(6)*Ne;
    ThetaCom(1) = Theta(1) + Theta(3) + Theta(5);
    ThetaCom(2) = Theta(2) + Theta(4) + Theta(6);

    %% Magnetizing flux derivative
    [dPhiC1dTheta1, dPhiC1dTheta2] = differentiate(phiCoreSfit{1}, LmNL*ThetaCom(1),
    LmNL*ThetaCom(2) * LmM);
    [dPhiC3dTheta1, dPhiC3dTheta2] = differentiate(phiCoreSfit{3},
```

```
    LmNL*ThetaCom(1) * LmM, LmNL*ThetaCom(2));

    dPhiC1dTheta2 = dPhiC1dTheta2 * LmM;
    dPhiC3dTheta1 = dPhiC3dTheta1 * LmM;

    dPhiC2dTheta1 = - dPhiC1dTheta1 - dPhiC3dTheta1;
    dPhiC2dTheta2 = - dPhiC1dTheta2 - dPhiC3dTheta2;

    %% Magnetizing inductance
    Mc(1,1) =   Np*dPhiC1dTheta1*Np - Np*dPhiC2dTheta1*Np;
    Mc(2,1) = - Np*dPhiC2dTheta1*Np + Np*dPhiC3dTheta1*Np;
    Mc(3,1) =   Ns*dPhiC1dTheta1*Np - Ns*dPhiC2dTheta1*Np;
    Mc(4,1) = - Ns*dPhiC2dTheta1*Np + Ns*dPhiC3dTheta1*Np;
    Mc(5,1) =   Ne*dPhiC1dTheta1*Np - Ne*dPhiC2dTheta1*Np;
    Mc(6,1) = - Ne*dPhiC2dTheta1*Np + Ne*dPhiC3dTheta1*Np;
    Mc(1,2) =   Np*dPhiC1dTheta2*Np - Np*dPhiC2dTheta2*Np;
    Mc(2,2) = - Np*dPhiC2dTheta2*Np + Np*dPhiC3dTheta2*Np;
    Mc(3,2) =   Ns*dPhiC1dTheta2*Np - Ns*dPhiC2dTheta2*Np;
    Mc(4,2) = - Ns*dPhiC2dTheta2*Np + Ns*dPhiC3dTheta2*Np;
    Mc(5,2) =   Ne*dPhiC1dTheta2*Np - Ne*dPhiC2dTheta2*Np;
    Mc(6,2) = - Ne*dPhiC2dTheta2*Np + Ne*dPhiC3dTheta2*Np;
    Mc(1,3) =   Np*dPhiC1dTheta1*Ns - Np*dPhiC2dTheta1*Ns;
    Mc(2,3) = - Np*dPhiC2dTheta1*Ns + Np*dPhiC3dTheta1*Ns;
    Mc(3,3) =   Ns*dPhiC1dTheta1*Ns - Ns*dPhiC2dTheta1*Ns;
    Mc(4,3) = - Ns*dPhiC2dTheta1*Ns + Ns*dPhiC3dTheta1*Ns;
    Mc(5,3) =   Ne*dPhiC1dTheta1*Ns - Ne*dPhiC2dTheta1*Ns;
    Mc(6,3) = - Ne*dPhiC2dTheta1*Ns + Ne*dPhiC3dTheta1*Ns;
    Mc(1,4) =   Np*dPhiC1dTheta2*Ns - Np*dPhiC2dTheta2*Ns;
    Mc(2,4) = - Np*dPhiC2dTheta2*Ns + Np*dPhiC3dTheta2*Ns;
    Mc(3,4) =   Ns*dPhiC1dTheta2*Ns - Ns*dPhiC2dTheta2*Ns;
    Mc(4,4) = - Ns*dPhiC2dTheta2*Ns + Ns*dPhiC3dTheta2*Ns;
    Mc(5,4) =   Ne*dPhiC1dTheta2*Ns - Ne*dPhiC2dTheta2*Ns;
    Mc(6,4) = - Ne*dPhiC2dTheta2*Ns + Ne*dPhiC3dTheta2*Ns;
    Mc(1,5) =   Np*dPhiC1dTheta1*Ne - Np*dPhiC2dTheta1*Ne;
    Mc(2,5) = - Np*dPhiC2dTheta1*Ne + Np*dPhiC3dTheta1*Ne;
    Mc(3,5) =   Ns*dPhiC1dTheta1*Ne - Ns*dPhiC2dTheta1*Ne;
    Mc(4,5) = - Ns*dPhiC2dTheta1*Ne + Ns*dPhiC3dTheta1*Ne;
    Mc(5,5) =   Ne*dPhiC1dTheta1*Ne - Ne*dPhiC2dTheta1*Ne;
    Mc(6,5) = - Ne*dPhiC2dTheta1*Ne + Ne*dPhiC3dTheta1*Ne;
    Mc(1,6) =   Np*dPhiC1dTheta2*Ne - Np*dPhiC2dTheta2*Ne;
    Mc(2,6) = - Np*dPhiC2dTheta2*Ne + Np*dPhiC3dTheta2*Ne;
    Mc(3,6) =   Ns*dPhiC1dTheta2*Ne - Ns*dPhiC2dTheta2*Ne;
    Mc(4,6) = - Ns*dPhiC2dTheta2*Ne + Ns*dPhiC3dTheta2*Ne;
    Mc(5,6) =   Ne*dPhiC1dTheta2*Ne - Ne*dPhiC2dTheta2*Ne;
    Mc(6,6) = - Ne*dPhiC2dTheta2*Ne + Ne*dPhiC3dTheta2*Ne;

    %% Leakage inductance
    Ml(1,1) =   Lfg(1,1) - Lfg(2,1);
    Ml(2,1) = - Lfg(2,1) + Lfg(3,1);
    Ml(3,1) =   Lfg(4,1) - Lfg(5,1);
    Ml(4,1) = - Lfg(5,1) + Lfg(6,1);
    Ml(1,2) =   Lfg(1,2) - Lfg(2,2);
    Ml(2,2) = - Lfg(2,2) + Lfg(3,2);
    Ml(3,2) =   Lfg(4,2) - Lfg(5,2);
    Ml(4,2) = - Lfg(5,2) + Lfg(6,2);
    Ml(1,3) =   Lfg(1,3) - Lfg(2,3);
    Ml(2,3) = - Lfg(2,3) + Lfg(3,3);
    Ml(3,3) =   Lfg(4,3) - Lfg(5,3);
    Ml(4,3) = - Lfg(5,3) + Lfg(6,3);
    Ml(1,4) =   Lfg(1,4) - Lfg(2,4);
    Ml(2,4) = - Lfg(2,4) + Lfg(3,4);
    Ml(3,4) =   Lfg(4,4) - Lfg(5,4);
    Ml(4,4) = - Lfg(5,4) + Lfg(6,4);
    Ml(5,5) =   Leh;
    Ml(6,6) =   Leh;

    %% Inductance matrix
    Mx = Mc + Ml;
end
```

Listing A5. DAB3_model_Fsys.m

```
function Fx = DAB3_model_Fsys(t,y)
    DAB3_param;

    uA = Udc1 * (0.5 * DAB3_square(t,        0) + 0.5);
```

```
    uB = Udc1 * (0.5 * DAB3_square(t, - 2*pi/3) + 0.5);
    uC = Udc1 * (0.5 * DAB3_square(t, + 2*pi/3) + 0.5);
    ua = Udc2 * (0.5 * DAB3_square(t,        0 - delta) + 0.5);
    ub = Udc2 * (0.5 * DAB3_square(t, - 2*pi/3 - delta) + 0.5);
    uc = Udc2 * (0.5 * DAB3_square(t, + 2*pi/3 - delta) + 0.5);
    u1 = (2*uA - uB - uC)/3;
    u2 = (2*uB - uC - uA)/3;
    u3 = (2*uC - uA - uB)/3;
    u4 = (2*ua - ub - uc)/3;
    u5 = (2*ub - uc - ua)/3;
    u6 = (2*uc - ua - ub)/3;

    Fx(1,1) = u1 - u2;
    Fx(2,1) = u3 - u2;
    Fx(3,1) = u4 - u5;
    Fx(4,1) = u6 - u5;
    Fx(5,1) = 0;
    Fx(6,1) = 0;
end
```

Listing A6. DAB3_square.m

```
function y = DAB3_square(t, ph)
    DAB3_param;

    SinTrans = sin(2*pi*fcc*Tcctrans/2);
    usin = 1/SinTrans * sin(2*pi*fcc*t + ph);

    y = min(max(usin,-1),1);
end
```

Listing A7. DAB3_model_Rsys.m

```
function Rx = DAB3_model_Rsys(t,y)
    DAB3_param;

    Rx(1,1) = R1+R2;
    Rx(2,1) = R2;
    Rx(1,2) = R2;
    Rx(2,2) = R2+R3;
    Rx(3,3) = R4+R5;
    Rx(4,3) = R5;
    Rx(3,4) = R5;
    Rx(4,4) = R5+R6;
    Rx(5,5) = R7+R8;
    Rx(6,5) = R8;
    Rx(5,6) = R8;
    Rx(6,6) = R8+R9;
end
```

## Appendix 2. Single-phase MFT including the hysteresis model

The single-phase MFT was developed at SuperGrid Institute for the 100 kW DC-DC converter in 2015 [95], [139], [140]. For the windings, a copper foil 270 mm x 0.2 mm was used and the core was made from 3C90 ferrite I-cores. The core cross section is 33.6 cm$^2$. The primary winding is composed of 2 coils connected in series, each containing 14 turns. The secondary winding is composed of 2 coils connected in parallel, each containing 14 turns. The prototype weight is 40 kg and volume 32.5 dm$^3$. It is presented in the Fig. A1. The dark red wires are the thermocouple connections allowing to measure the temperature at different points of the transformer.

Fig. A1. Single-phase MFT prototype 180 kVA [139]

The single-phase MFT equivalent circuit parameters are presented in the Table A1.

Table A1. Single-phase MFT equivalent circuit parameters [139]

| | Primary winding | Secondary winding |
|---|---|---|
| Number of turns | 28 | 14 |
| Resistance at 20 kHz | 9.5 mΩ | 1.9 mΩ |
| Leakage inductance | 1.3 µH | 0.8 µH |
| Capacitance | 0.4 nF | 4.3 nF |

The author contributed to the development of the single-phase MFT circuit model including the hysteresis what was reported in [39]. The feedback Preisach model was developed and the Fig. A2 shows the simulated symmetrical major loop compared with the experimental measurement.

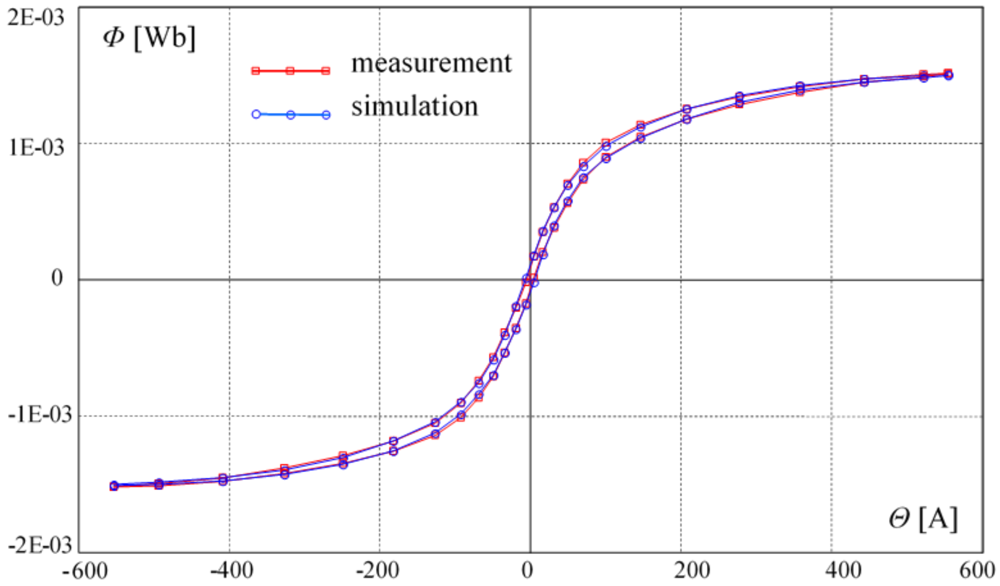

Fig. A2. Simulated and measured trajectories of the symmetrical major hysteresis loops for the single-phase MFT

In order to validate the hysteresis model in a circuit simulation, a no-load operation of the transformer was considered. The proposed equivalent circuit is presented in Fig. A3.

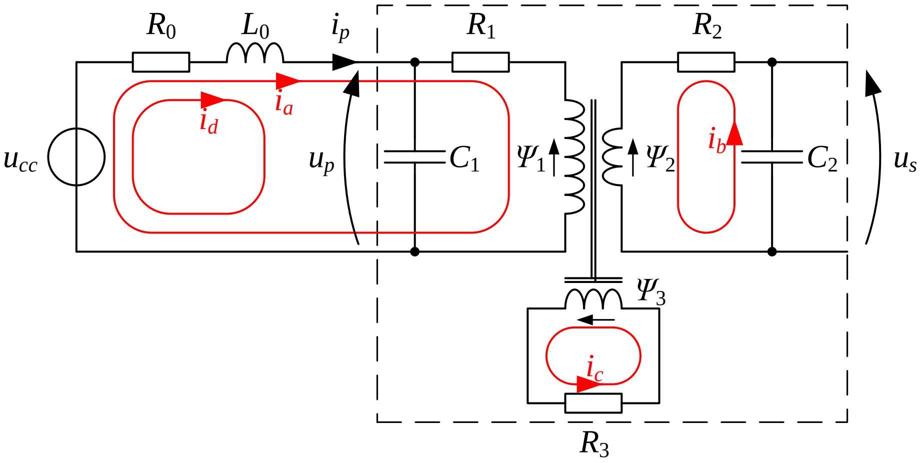

Fig. A3. Single-phase MFT equivalent circuit diagram for no load test: $u_{cc}$ - programmable voltage source; $R_0$, $L_0$ - resistance and inductance of the voltage source and connections; $R_1$, $C_1$, $\Psi_1$ - primary winding resistance, capacitance and flux linkage; $R_2$, $C_2$, $\Psi_2$ - secondary winding resistance, capacitance and flux linkage; $R_3$, $\Psi_3$ - resistance and flux linkage of the equivalent eddy current and excess losses circuit; $i_a$, $i_b$, $i_c$, $i_d$ - loop currents (in red); $u_p$, $u_s$, $i_p$ - primary voltage, secondary voltage and primary current

The Lagrange energy method was proposed to model the circuit. The final matrix form of the Euler-Lagrange equation is:

$$
\begin{bmatrix} L_0+L_{\sigma 1} & 0 & 0 & 0 \\ 0 & L_{\sigma 2} & 0 & 0 \\ 0 & 0 & L_{\sigma 3} & 0 \\ L_0 & 0 & 0 & L_0 \end{bmatrix}
\begin{bmatrix} \ddot{q}_a \\ \ddot{q}_b \\ \ddot{q}_c \\ \ddot{q}_d \end{bmatrix}
+ \frac{\partial \Phi_c}{\partial \Theta}
\begin{bmatrix} N_1N_1 & N_1N_2 & N_1N_3 & 0 \\ N_2N_1 & N_2N_2 & N_2N_3 & 0 \\ N_3N_1 & N_3N_2 & N_3N_3 & 0 \\ 0 & 0 & 0 & 0 \end{bmatrix}
\begin{bmatrix} \ddot{q}_a \\ \ddot{q}_b \\ \ddot{q}_c \\ \ddot{q}_d \end{bmatrix}
$$

$$
= \begin{bmatrix} u_{cc}(t) \\ 0 \\ 0 \\ u_{cc}(t) \end{bmatrix}
- \begin{bmatrix} R_0+R_1 & 0 & 0 & R_0 \\ 0 & R_2 & 0 & 0 \\ 0 & 0 & R_3 & 0 \\ R_0 & 0 & 0 & R_0 \end{bmatrix}
\begin{bmatrix} \dot{q}_a \\ \dot{q}_b \\ \dot{q}_c \\ \dot{q}_d \end{bmatrix}
- \begin{bmatrix} 0 & 0 & 0 & 0 \\ 0 & \frac{1}{C_2} & 0 & 0 \\ 0 & 0 & 0 & 0 \\ 0 & 0 & 0 & \frac{1}{C_1} \end{bmatrix}
\begin{bmatrix} q_a \\ q_b \\ q_c \\ q_d \end{bmatrix}
\tag{A1}
$$

where

$$
\dot{q} = \frac{dq}{dt} = i \tag{A2}
$$

$$
\Theta(\dot{\mathbf{q}}) = N_1\dot{q}_a + N_2\dot{q}_b + N_3\dot{q}_c \tag{A3}
$$

and $N_k$ is the number of turns of the $k$-th coil and $L_{\sigma k}$ is the leakage inductance. The relationship $\Phi_c(\Theta)$ involves the feedback Preisach model of hysteresis.

A no load operating point at 800 V 17 kHz is presented in Fig. A4 for the simulation and the measurement. A no load operation with an increased supply voltage is presented in Fig. A5. It can be observed that the simulation model fits the measurement quite well. The small differences are probably caused by the slightly different supply voltage shape.

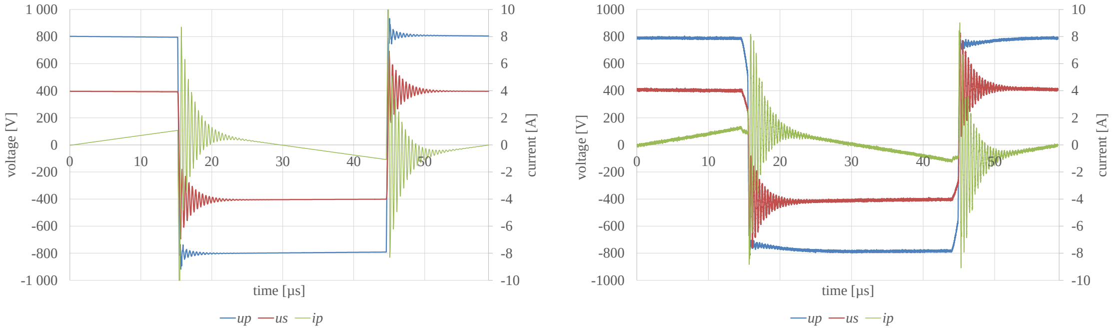

Fig. A4. Simulated (left) and measured (right) waveforms at 800 V 17 kHz no load operation: primary voltage $u_p$, secondary voltage $u_s$, primary current $i_p$

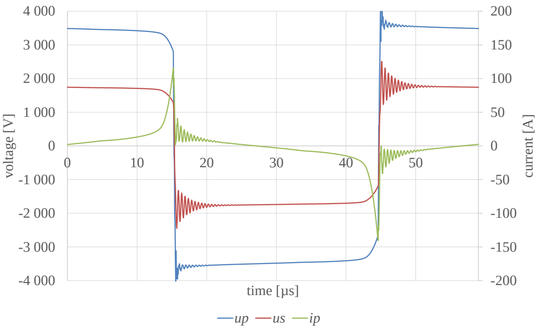

Fig. A5. Simulated waveforms with an increased supply voltage 3500 V 17 kHz no load operation: primary voltage $u_p$, secondary voltage $u_s$, primary current $i_p$

The transformer circuit model involving the feedback Preisach model of hysteresis enables a precise analysis in various operating conditions like frequency change or supply voltage shape change. The hysteresis and eddy current losses are directly calculated enabling, for example to evaluate the impact of a power converter design on the transformer performance.

## Appendix 3. Magnetic hysteresis model of a 3-phase MFT

The magnetic hysteresis model presented in chapter 3 can be implemented in the transformer equivalent circuit model as it was presented in Appendix 2 for the single-phase MFT. However, the extension of the model to the 3-phase MFT is challenging. In this appendix some preliminary considerations are presented on the magnetic hysteresis model in circuit analysis of the 3-phase MFT.

The magnetic hysteresis model is available in several commercial simulation software, including:

- Ansys Maxwell - FEM simulator using vector play model [106],
- Cobham/Dassault Opera 3D - FEM simulator (probably using Preisach model) [24],
- Matlab Simulink - circuit simulator using arctangent analytical expression *Ψ*(*i*) and its inverse *i*(*Ψ*) [115],
- Plexim Plecs - circuit simulator using Preisach model [110].

The author utilized the Ansys Maxwell magnetic transient simulations with the 3-phase MFT. An example simulation result is presented in Fig. A6 where the hysteresis effect can be observed in phase current waveforms. The hysteresis loss and eddy current loss are calculated by the solver but the author has limited confidence in the results because there are no details available on the implemented model variant and the model parameters.

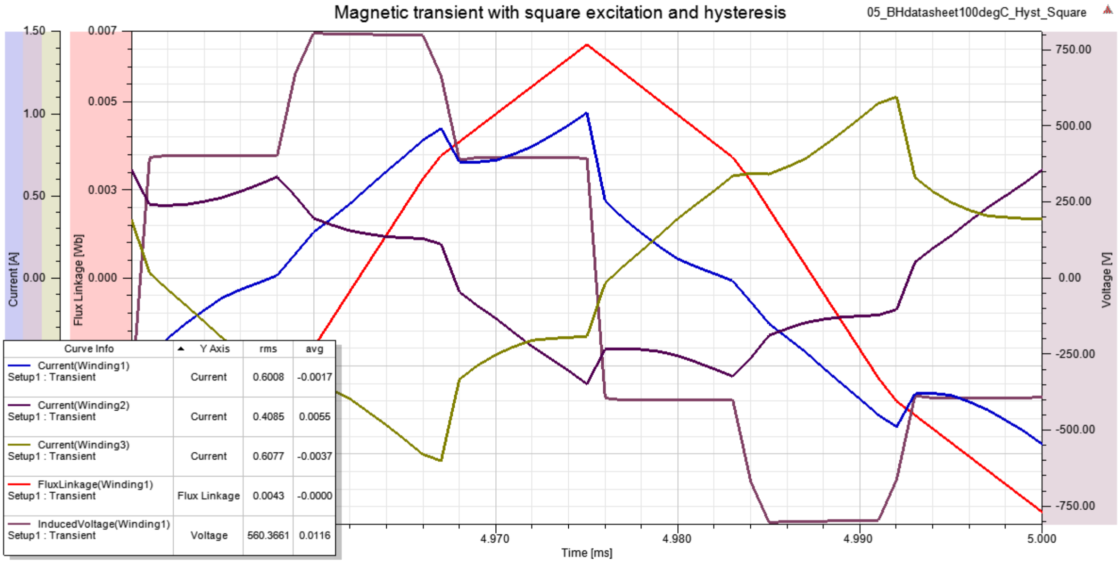

| Curve Info | Y Axis | rms | avg |
|---|---|---|---|
| Current(Winding1)<br>Setup1 : Transient | Current | 0.6008 | -0.0017 |
| Current(Winding2)<br>Setup1 : Transient | Current | 0.4085 | 0.0055 |
| Current(Winding3)<br>Setup1 : Transient | Current | 0.6077 | -0.0037 |
| FluxLinkage(Winding1)<br>Setup1 : Transient | Flux Linkage | 0.0043 | -0.0000 |
| InducedVoltage(Winding1)<br>Setup1 : Transient | Voltage | 560.3661 | 0.0116 |

Fig. A6. Ansys Maxwell magnetic transient simulation of 3-phase MFT including the hysteresis model

A circuit model of the 3-phase MFT involving the magnetic hysteresis can be developed based on the equivalent reluctance model. In [35] the hysteresis model based on polynomial interpolations was used. This model could be further improved using the feedback Preisach model.

The reluctance model of a 3-phase core type transformer, considering the magnetizing flux only, can be simplified to the circuit presented in Fig. A7.

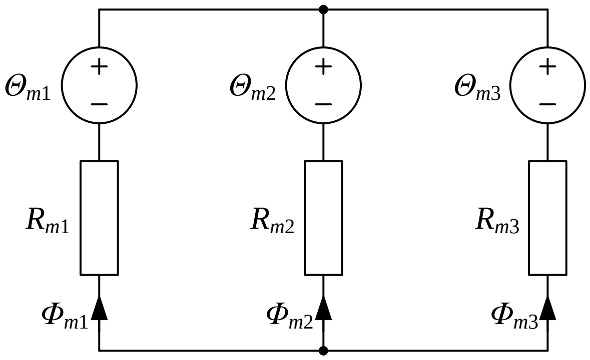

Fig. A7. Simplified reluctance model of the magnetizing flux in the 3-phase core type transformer

The reluctance model can be described with the equation:

$$\begin{bmatrix} 1 & 1 & 1 \\ -R_{m1} & R_{m2} & 0 \\ 0 & -R_{m2} & R_{m3} \end{bmatrix} \begin{bmatrix} \Phi_{m1} \\ \Phi_{m2} \\ \Phi_{m3} \end{bmatrix} = \begin{bmatrix} 0 \\ \Theta_{m2} - \Theta_{m1} \\ \Theta_{m3} - \Theta_{m2} \end{bmatrix} \tag{A4}$$

where $\Phi_m$ is defined in (3.9), $\Theta_m$ is defined in (3.10) and $R_m$ is defined according to [35] with:

$$R_m = R_m(\Phi_m) = \frac{l_m}{A_c} \frac{\partial}{\partial B} H[B(\Phi_m)] \tag{A5}$$

where $l_m$ is the average magnetic circuit length, $A_c$ is the average cross-section of the core and the $H(B)$ is the inverse of the $B(H)$ defined in §3.3.2 with the parameters from §5.4.

The transformer model can be further derived starting from the equation (3.1).

## Appendix 4. MFT prototypes

In this appendix some details of the MFT prototypes are presented. The 3-phase MFT prototype T2 before impregnation is presented in Fig. A8. Different views of MFT T2 are presented in Fig. A9.

Fig. A8. 3-phase MFT prototype T2 before impregnation

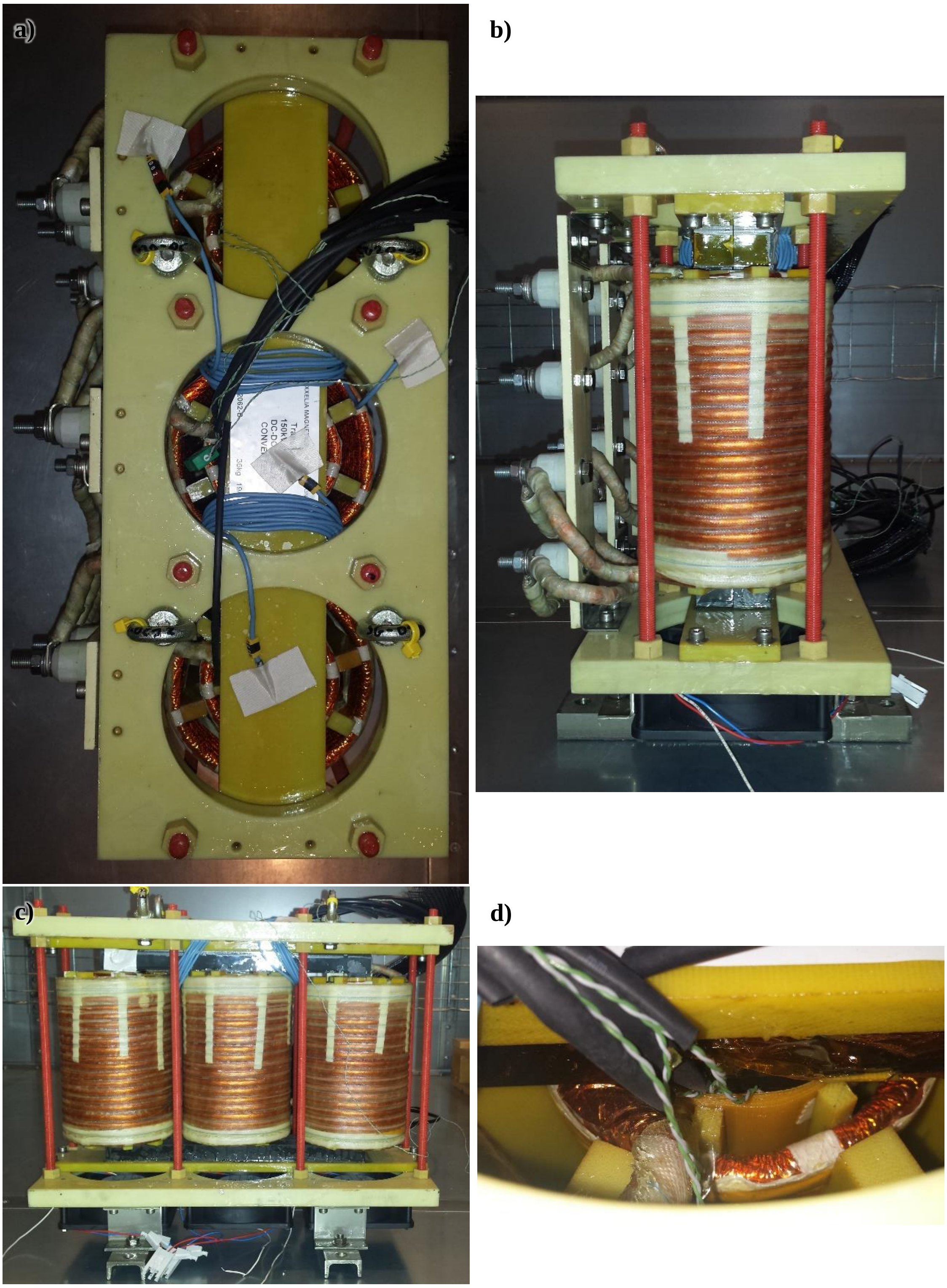

Fig. A9. 3-phase MFT prototype T2: a) top view, b) side view, c) rear view, d) view of thermocouples

The single-phase multi air gap (MAG) MFTs are presented in Fig. A10. Their core assemblies are presented in Fig. A11.

Fig. A10. Single-phase multi air gap MFT: MAG4 (left) and MAG6 (right)

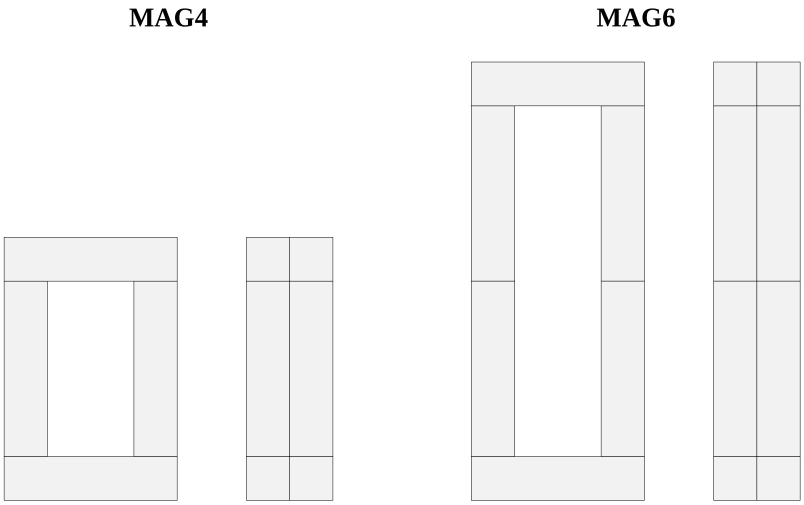

Fig. A11. Single-phase multi air gap MFT core assembly: MAG4 with 4 air gaps and MAG6 with 6 air gaps

The 3C90 ferrite I-core is presented in Fig. A12.

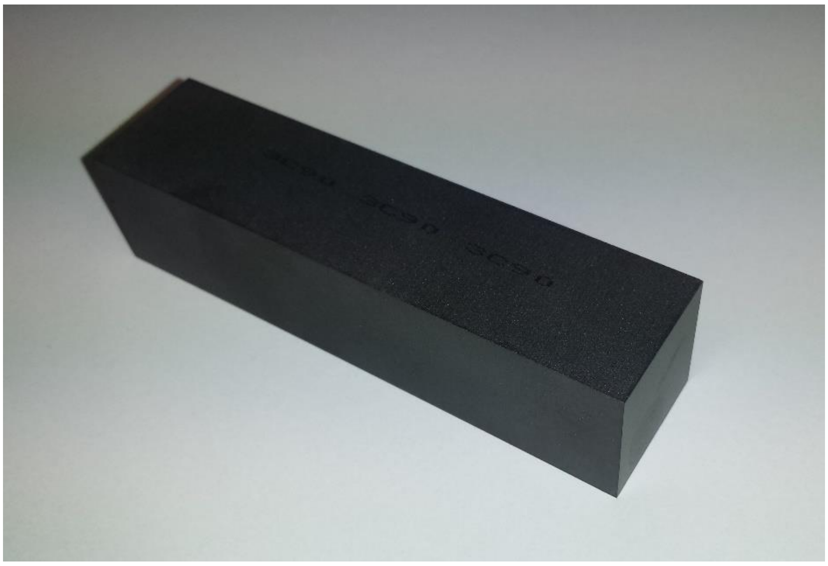
Fig. A12. 3C90 ferrite I-core measuring 100 mm x 25 mm x 25 mm

The position of thermocouples in the 3-phase MFT prototype is presented in Fig. A13.

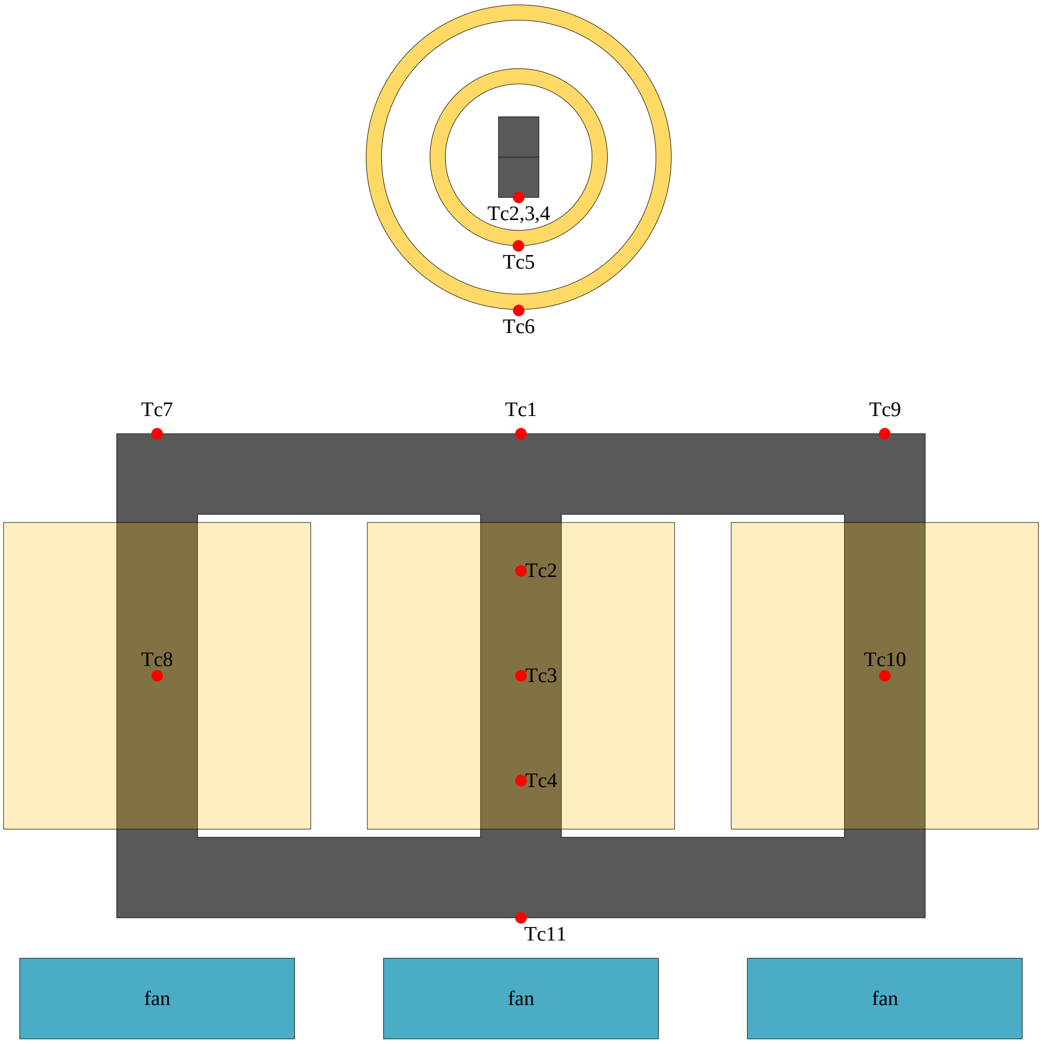

Fig. A13. Position of thermocouples in the 3-phase MFT

## Appendix 5. Measurement of power losses in an MFT

The power losses of the 3-phase MFT were measured in two configurations:

- MFT supplied from a variable frequency 3-phase sinusoidal power supply CHROMA 61704 [22] as presented in Fig. A14,
- MFT supplied from the VSC operating normally with the rectangular modulation as presented in Fig. A16.

The power measurement was done in the 2-wattmeter scheme.

Fig. A14. MFT T1 no load test with a variable frequency 3-phase sinusoidal power supply

In Fig. A15 the no load power loss of the MFT T1 supplied with a variable frequency 3-phase sinusoidal power supply at the ambient temperature of 25°C is presented. The operation at $B_{max}$ corresponding to Y and D vector groups was considered. The measurement with ZES Zimmer [201] is compared against the calculation with the Steinmetz equation (4.7) and a significant difference is observed. It is likely that the Steinmetz parameters are not valid at low frequency. However, if the measurement is extrapolated to higher frequency then the difference becomes smaller and the measurement is lower than the calculation.

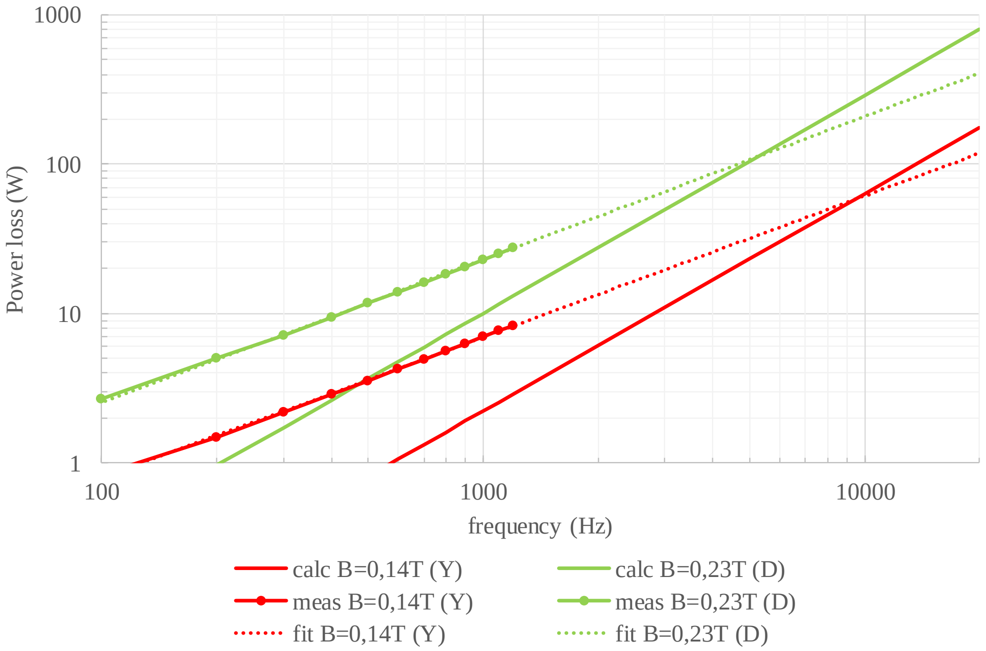

Fig. A15. No load power loss of the MFT T1 with the variable frequency 3-phase sinusoidal power supply for two values of $B_{max}$ corresponding to Y and D vector groups: measurement (solid dotted line) and extrapolation (dotted line), calculation with Steinmetz equation (solid line)

In Fig. A17 the no load power loss of the MFT T2 supplied from the VSC operating normally at 20 kHz with the rectangular modulation is presented. The measurement of MFT power loss was done with: power analyser ZES Zimmer LMG670 [201], power analyser Yokogawa WT1800E [197] and oscilloscope Tektronix 5 series [168]. The core temperature was slightly different in different tests. The measurements are compared against the calculation with the Steinmetz equation (4.9) and a significant difference is observed, especially at high DC voltage. The total power loss of the VSC and MFT was measured (P_DC) and the values divided by 3 are displayed. It is difficult to evaluate the share of the MFT power loss in the total power loss but one third seems reasonable in the no load test. However, no conclusion can be made because none of the calculation or measurement cannot be considered valid. It should be noted that the accuracy of the power analysers at 20 kHz is not good, potentially in the same range as the measured power loss.

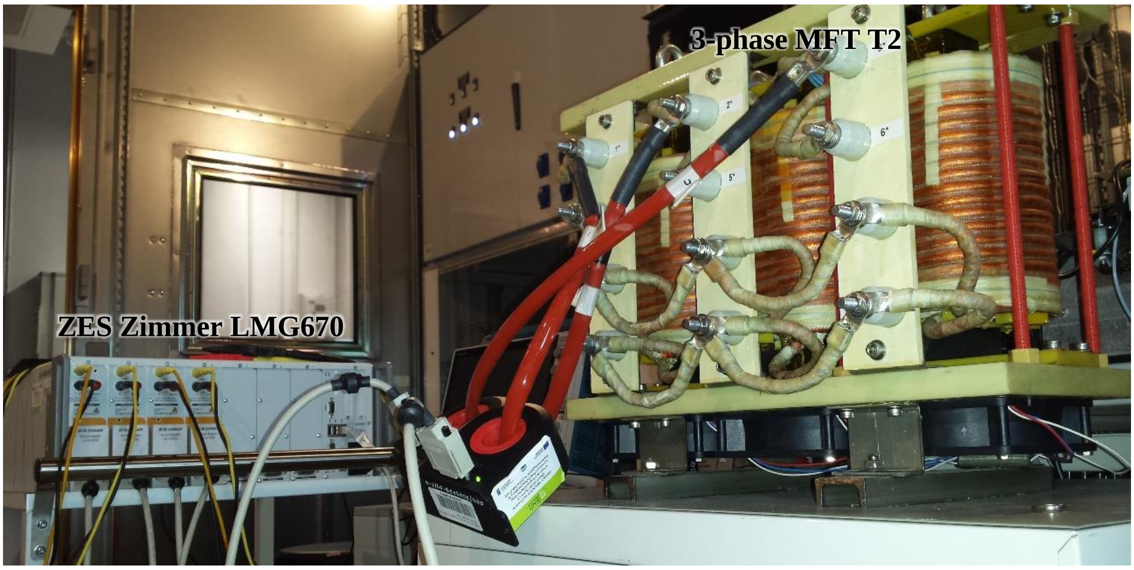

Fig. A16. MFT T2 no load test with the supply from the VSC

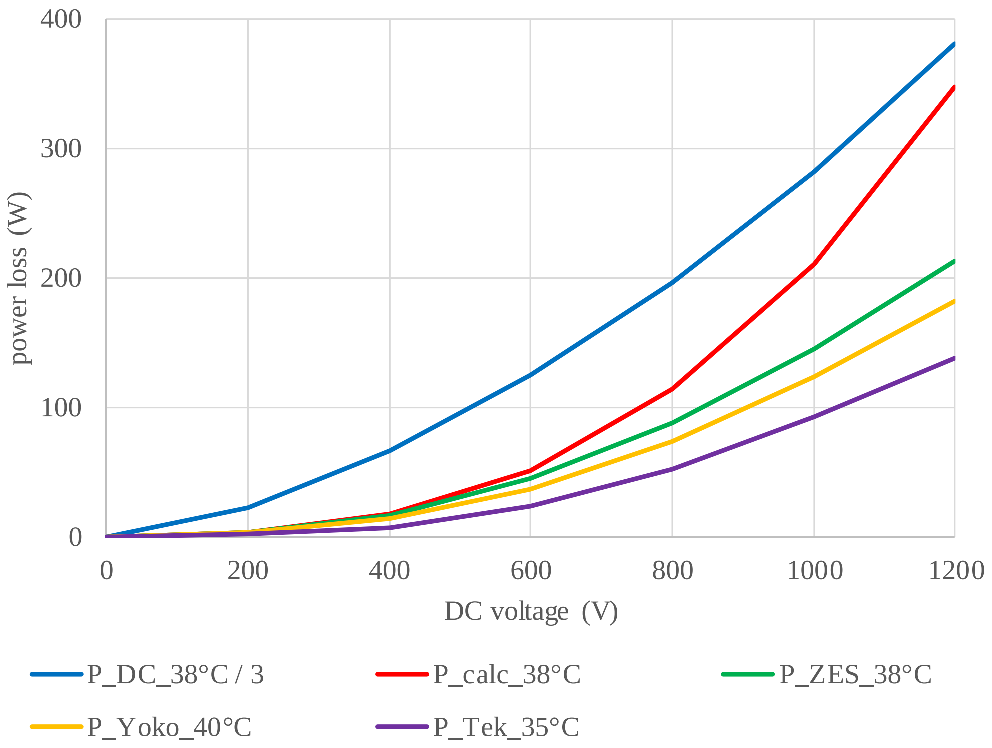

Fig. A17. No load power loss of the MFT T2 with the VSC supply at 20 kHz: P_DC total VSC and MFT measured power loss (values divided by 3), P_calc MFT power loss calculated with the Steinmetz equation, P_ZES MFT power loss measured with ZES Zimmer LMG670, P_Yoko MFT power loss measured with Yokogawa WT1800E, P_tek MFT power loss measured with Tektronix 5 series oscilloscope

In Fig. A18 and Fig. A19 the no load power losses of the MFT T2 supplied from the VSC at 2.5 kHz and 5 kHz are presented. The measurements with ZES Zimmer LMG670 are compared against the calculations with the Steinmetz equation (4.9). In reference to the measurement at 20 kHz, better fit is observed especially below the nominal flux density $B_{max}$. This analysis shows that the frequency and voltage amplitude may influence the accuracy of the power analyser measurement.

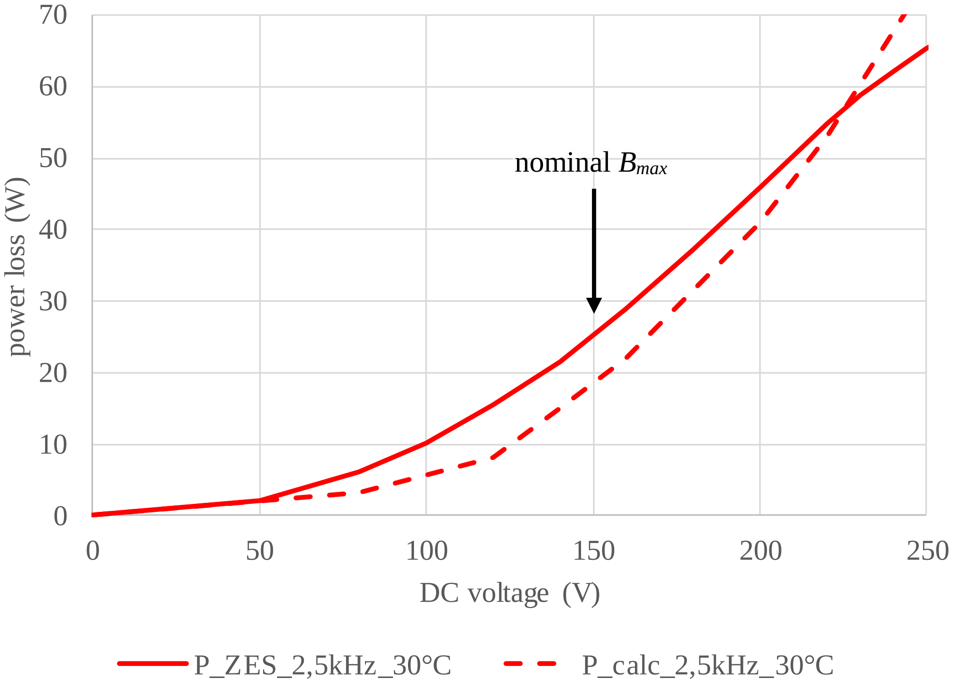

Fig. A18. No load power loss of the MFT T2 with the VSC supply at 2.5 kHz: P_ZES power loss measured with ZES Zimmer LMG670, P_calc power loss calculated with the Steinmetz equation

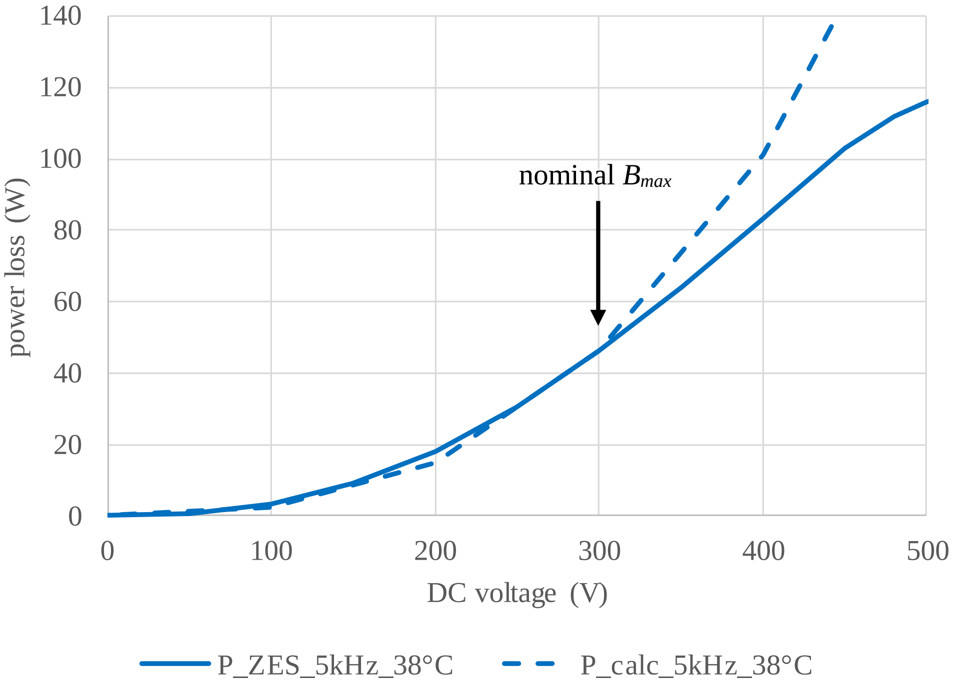

Fig. A19. No load power loss of the MFT T2 with the VSC supply at 5 kHz: P_ZES power loss measured with ZES Zimmer LMG670, P_calc power loss calculated with the Steinmetz equation

An MFT full load test was done but at several operating points a negative power loss was measured.

The measurement problems presented in this appendix are likely due to the high fundamental frequency and high harmonics, especially in the voltage measurement, incompatible with the available power analysers. Considering that the thermal simulation and measurement are consistent (§6.1.2), it is likely that the MFT power loss measurement method is not valid. The author concludes that the measurement of the MFT efficiency is a subject on its own and it exceeds the scope of this thesis. In the scientific literature the calorimetric methods are considered [146].